RPN
28

LABORATORY OF PLASMA STUDIES
CORNELL UNIVERSITY
ITHACA, NEW YORK

OPERATIONAL CHARACTERISTICS AND ENTRANCE CONDITIONS OF A HIGH-CURRENT, RELATIVISTIC ELECTRON BEAM ACCELERATOR

by

J. J. Clark
S. Linke

LPS 23 AUGUST 1969

This research was supported by the Office of Naval Research (ONR) under Contract No. N00014-67-A-0077-0003.

Major portions of this report are reproduced from a Ph.D. Thesis by John J. Clark, Cornell University, dated July, 1969.

TABLE OF CONTENTS

ABSTRACT

The design and construction of a 500 KV, 100 KA, 50 nsec pulse duration, electron beam accelerator used as a basic plasma-physics research tool are discussed.

The operational characteristics of a high-field-emission diode which is used to launch the electron beam in such an accelerator system are discussed in detail. The diode is shown empirically to have two separate and distinct modes of operation which depend on the diode aspect ratio, pressure, and total diode voltage and current. The first mode gives evidence of laminar electron flow, and the diode impedance is shown to be less than that predicted by the Child-Langmuir space-charge-limited flow equation by a factor of two, for diode pressures ranging from 5×10^{-3} to 10^{-5} torr. The second mode indicates a pressure dependent diode "pinching" phenomenon in the gap region, wherein the electrons are radially compressed and for which the diode impedance is equal to or greater than Child-Langmuir impedance predictions.

The electrons which form the beam are emitted from a metal-dielectric "plasma" cathode. The dielectric sections of this "plasma" cathode are shown to make an important contribution to the spatial uniformity of cathode emission by means of a surface multipactor or surface flashover effect which vaporizes enough of the dielectric to allow a plasma sheath to form in front of the cathode. There is evidence that the electrons, upon release from this sheath under space-charge-limited conditions, then determine the overall diode impedance.

Simple theoretical models for estimating the conditions under which diode pinching should occur are extended and verified. Data on these pinch conditions are of extreme interest because they predetermine the propagation characteristics of the electron beam as it propagates in a drift space. Diode pinching has been observed to occur (by radiographs and distributed calorimetry) for values of $\frac{\nu}{\gamma}\Big|_{\text{measured}}$ above 80% of $\frac{\nu}{\gamma}\Big|_{\text{critical}}$ as defined* by Friedlander,[1] and a minor correction to

his model for zero initial electron velocity is offered.

The time history of diode pinching was studied by means of a fast-streak/framing camera and indicates that:

1. Diode-pinch build-up times are generally about 30 nsec and are pressure independent, indicating that the electrons but not the ions are radially compressed.
2. The degree of pinching in the diode (and therefore the electron spatial distribution) is pressure dependent whereas the overall diode impedance is pressure independent - at least over the available range of $.5 \times 10^{-3}$ to 10^{-5} torr.
3. The electron trajectory angles at the anode plane increase up to what may be a saturation value as $\frac{\nu}{\gamma}$ increases from .66 to 1.05.

Recommendations for the elimination of such diode pinching, when and if desirable, are made.

---

* $\frac{\nu}{\gamma}$ is a measure of the ratio of electron transverse energy to electron axial energy.

1. Friedlander, F., Hechtel, R., Jory, H., Mosher, C., "Megavolt-Megampere Electron Gun Study," Final Report, Defense Atomic Support Agency (DASA), No. 2173, September 1968, Washington, D.C. 20305.

LIST OF ILLUSTRATIONS

INTRODUCTION

The theoretical analysis of high-current, relativistic electron beams was begun in 1934 by Bennett[26] and was continued and expanded by Alfvén[27] in 1939 and Lawson[28,29] in 1957-58.

Until about 1960, experimental techniques generally lagged the theory. Since 1960, advances in high-voltage pulse technology, such as those made by J.C. Martin and co-workers[1] at AWRE Aldermaston, England, have rapidly closed this gap and in many instances the experimental results now guide new theoretical analyses.[23]

Long-term interest in accelerators capable of launching such high-current, relativistic beams is based in part on the possibility that the electrostatic potential well of such an electron beam might prove useful as an accelerating mechanism for ions trapped in the well. In addition, such accelerators yield useful data on the transport properties of the beam in both vacuum and gaseous atmospheres, beam-plasma interactions, beam-emitted radiations, and a host of other basic plasma-physics phenomena.

In general, these electron beam accelerators consist of (1) an energy-storage component (usually capacitive) (2) a pulse-forming network, and (3) a high-field-emission diode which generates the electron beam and launches it through a thin-foil anode into a partially evacuated drift tube, thus forming the pulsed beam.

The design and construction details of a reliable, relatively low-cost accelerator of this type, built at Cornell University in 1968, are presented in Chapter I. The accelerator is capable of producing electron-beam currents of 30-100 KA at particle energies ranging from 200-500 KeV for pulse durations of approximately 50 nsec.

In the early stages of experimentation with this machine it became apparent that the propagation characteristics of the electron beam in the drift tube were critically dependent on the operational characteristics of the diode and on the spatial distribution of the diode current. Since such characteristics were not available in the literature, an extensive experimental examination of the diode was considered necessary. The development, execution and analysis of the results of this investigation constitute the major portions of this study.

The operational characteristics of a high-field-emission diode, which utilizes a metal-dielectric "plasma" cathode to launch the relativistic electron beam, are discussed in Chapter II.

The importance of the dielectric sections of the cathode on the spatial distribution of the diode current and some possible electron emission mechanisms are discussed in Chapter III.

Simple theoretical models have been proposed recently by Friedlander[14] and de Packh[26] for estimating the diode conditions for which a radial compression of the electron stream in the diode gap (i.e. "pinching") should occur. These models are compared in Chapter IV to measurements of the electron spatial distribution at the anode. Measurements performed included radiography, distributed calorimetry, and open-shuttered, and fast-streak/framing-camera photography.

CHAPTER I - THE CORNELL ACCELERATOR

A. BACKGROUND INFORMATION

The Cornell Accelerator was established as a direct result of the formation of a joint research program between Cornell University and the Naval Research Laboratory (NRL), Washington D.C. through the efforts of Professors E.L. Resler and S. Linke (Cornell) and Dr. Alan C. Kolb (NRL). The original design plans for the accelerator were suggested by Mr. J.C. Martin and his co-workers at the Atomic Weapons Research Establishment (AWRE) Aldermaston, England. (The Aldermaston group at this time were, and still are, among the free world's acknowledged leaders in the design and construction of flash X-ray diodes and associated system components.) A diode design capable of 1 MV and pulse lengths up to 100 nsec. was decided on. It was believed that longer pulse lengths would cause either diode-impedance collapse or internal dielectric breakdown of the diode insulators. This 100 nsec (maximum) pulse length in turn suggested a distributed transmission line for the pulse-forming network. As a side benefit, the increased dielectric strength of the transmission line, operating under pulsed rather than d-c conditions, could be examined.

Design and construction of the Cornell Accelerator under the guidance of the J.C. Martin group began on July 1, 1967. All major components were completed and tested within the following 6 months and the first relativistic beam was achieved on January 5, 1968. Monitoring waveforms available at this date included diode voltage, and Marx voltage. Accelerator characteristics are:

Beam Current	50 to 100 Kiloamps
Beam Voltage	300 to 500 KV
Pulse Duration	50-60 nsec
Energy/Pulse	~ 2 Kilojoules
Maximum Marx Storage	9.6 Kilojoules at 800 KV

B. DESCRIPTION OF ACCELERATOR COMPONENTS

The Cornell Accelerator consists of the following basic components: (See Figures 1 and 2)

A Marx Generator - for capacitive energy storage

A Mylar Transmission Line (Blumlein) - the pulse forming network or so called "fast section" .

A Field Emission Diode - to generate the electron beam and launch it into an appropriate drift tube. (Discussed in detail in Chapter II).

1. Marx Generator

The Marx Generator (See Figures 2 and 3) consists of sixteen 0.50 microfarad, 100 KV I.C.S.E. capacitors which are charged in parallel by a $\pm$ 60 KV,25 ma power supply in approximately 30 seconds. An interstage resistor network is used to balance the capacitor voltage.

The capacitors are discharged in a series configuration by means of an air-tight spark-gap column, one gap of which is triggered on demand by a 10 KV d-c power pack feeding a 1/10 step-up pulse transformer. Should the trigger source fail, the spark column may be ignited by evacuating the column to a suitable self-break point on it's breakdown-pressure characteristic curve (See Figure 4).

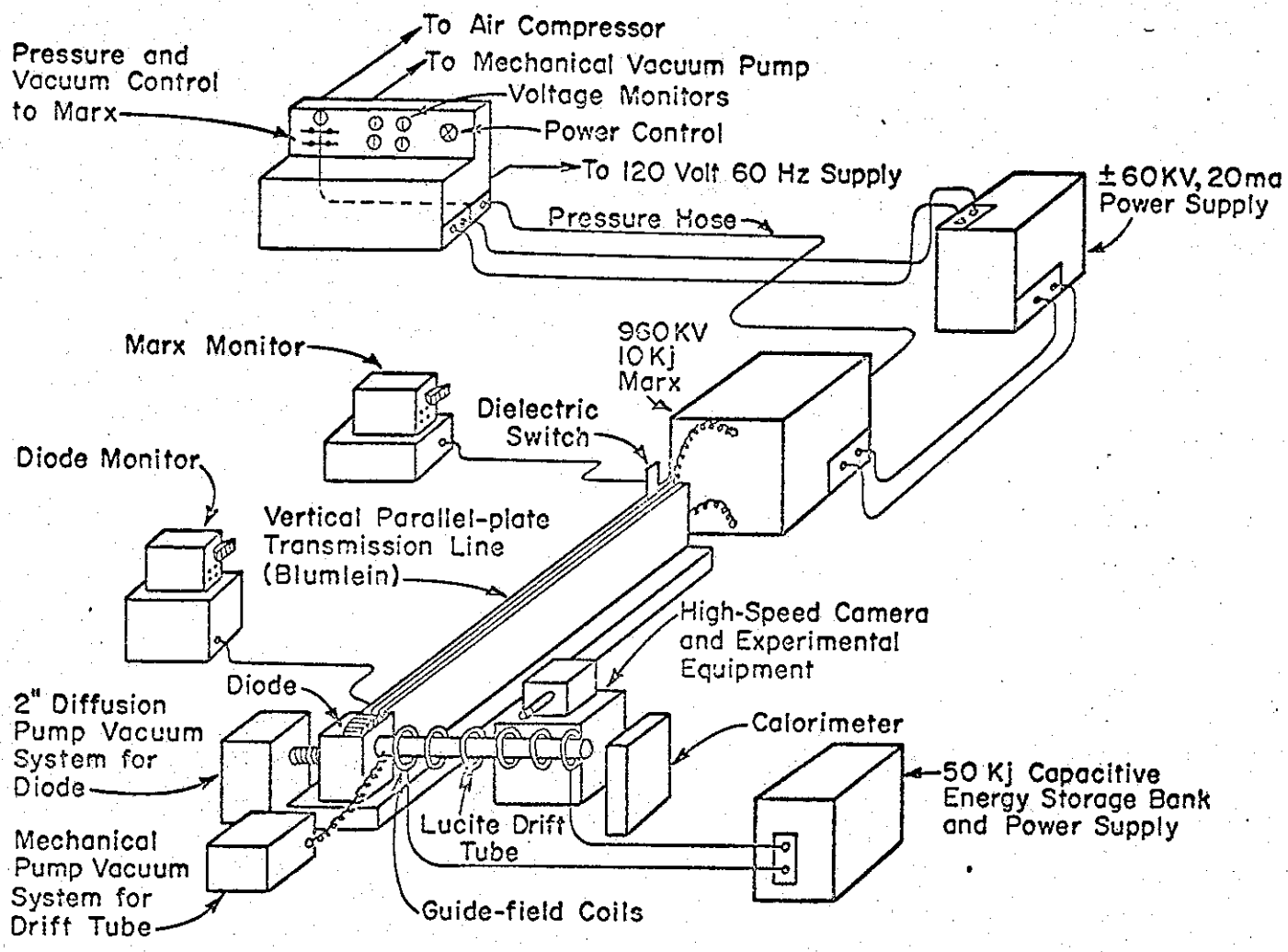

Fig. 1. Projection of 960 KV - 100 KA Accelerator

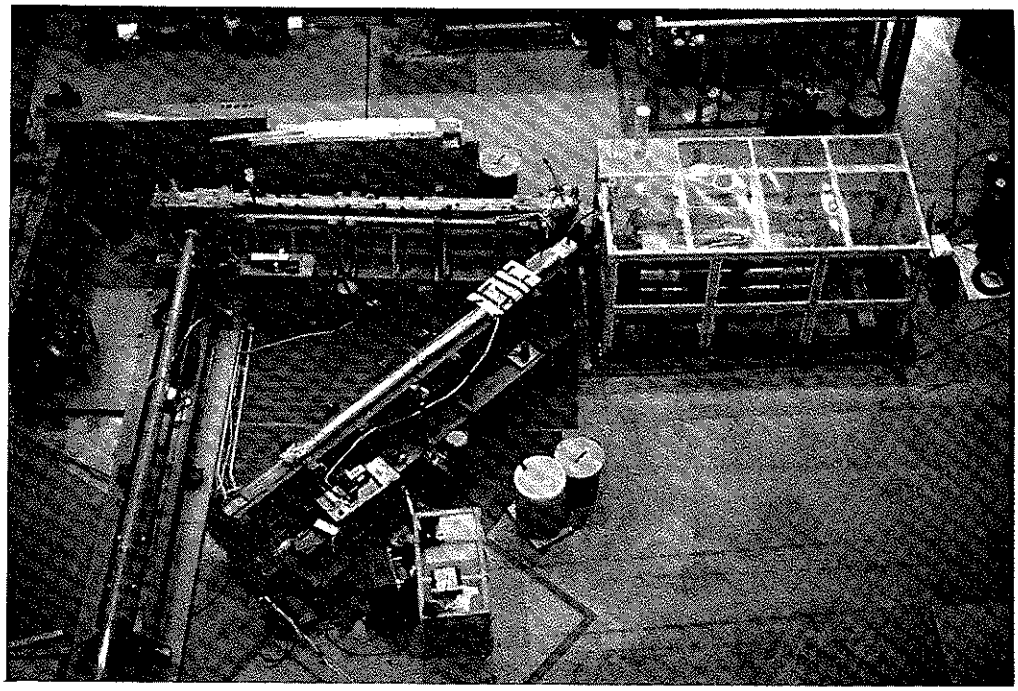

Fig. 2. Cornell Electron Beam Accelerator

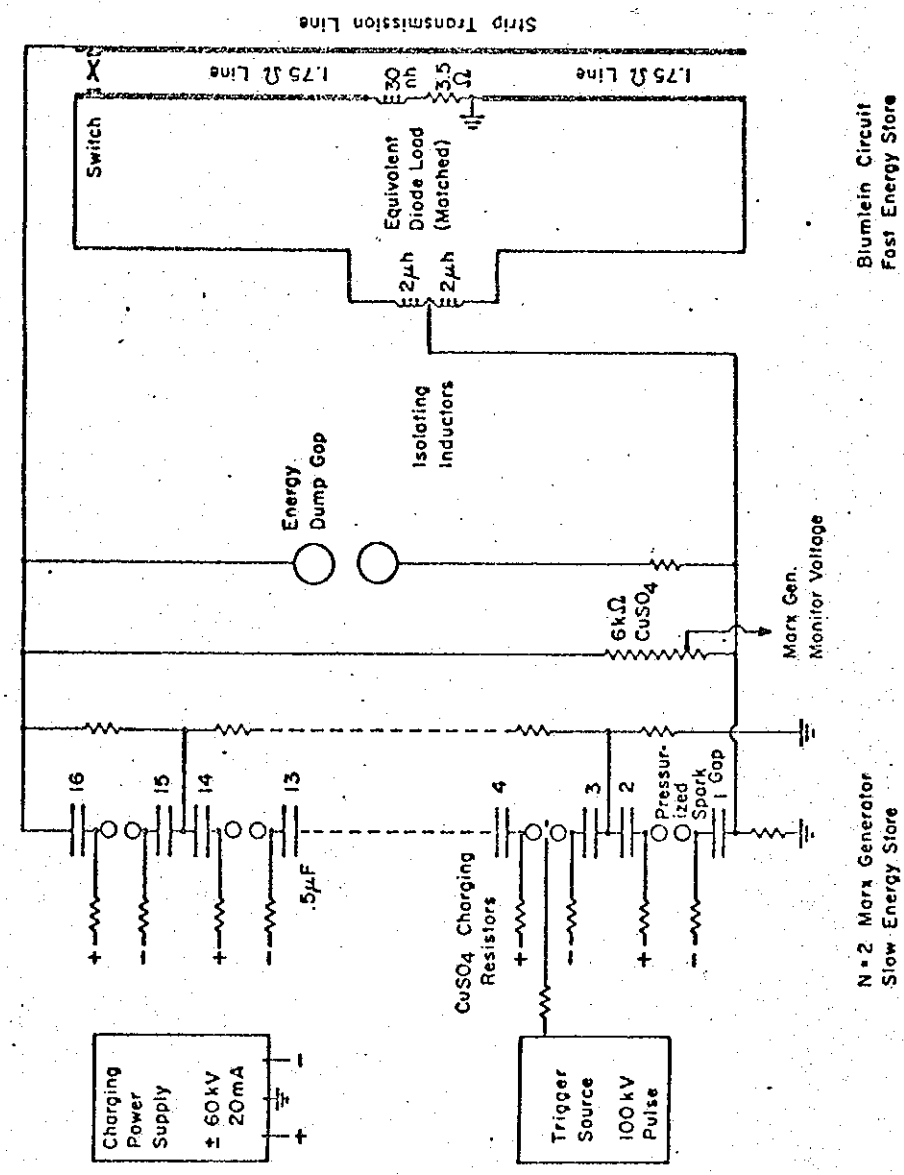

Fig. 3. Simplified System Schematic

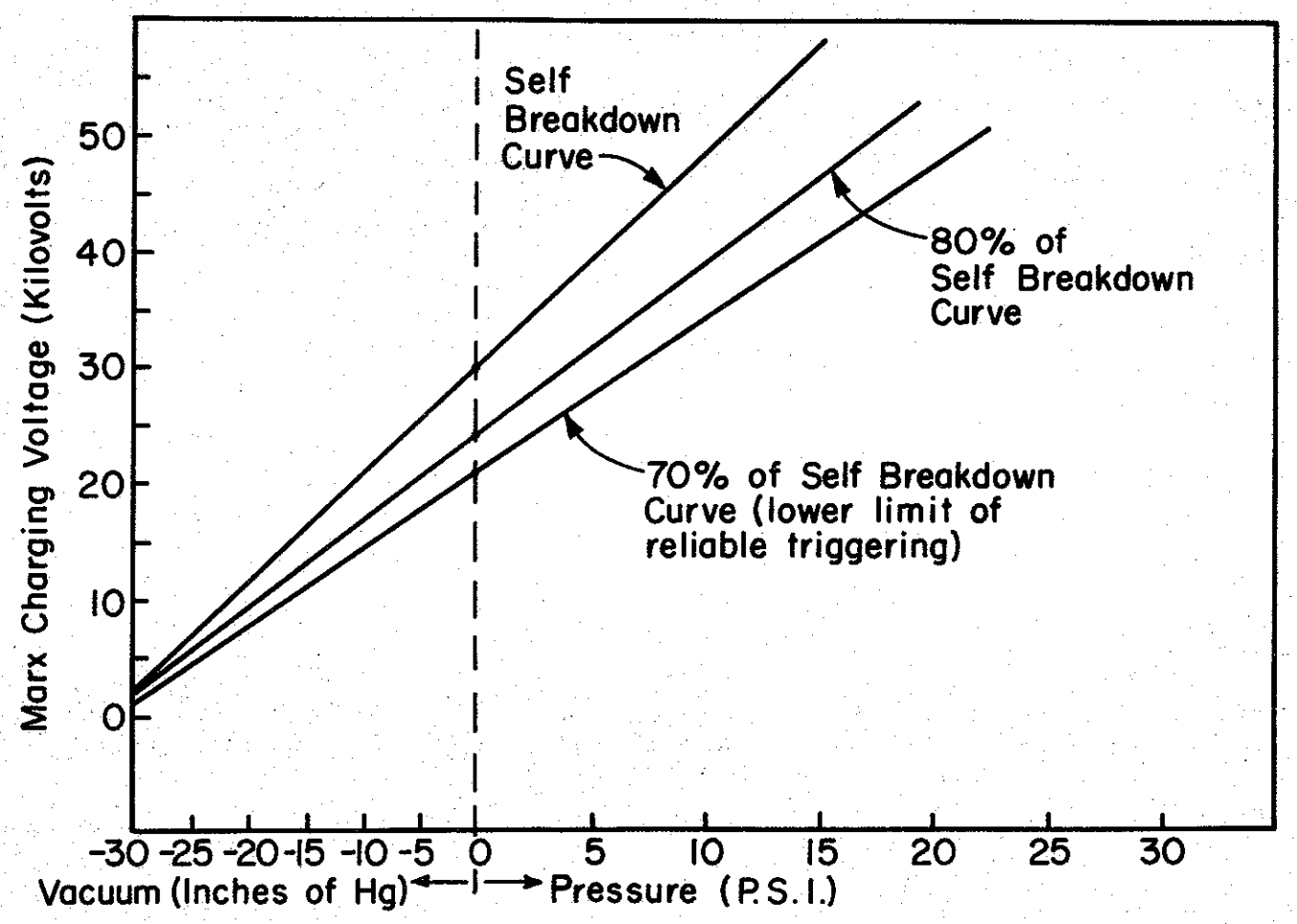

Fig. 4. Marx Spark Column Breakdown Voltage Vs Pressure Dependence

The maximum stored energy with the present charging system is 9.6 KJ at 800 KV. Since interstage flash-over of the capacitors occurs at about 480 KV in dry air, the entire Marx assembly was encased in a wooden framed, transparent,* lucite box, and Freon 12 refrigerant gas at atmospheric pressure used to replace the air as the dielectric medium. The now-standard "Freon Marx" was successfully tested up to 950 KV on March 27, 1968. A standard Freon refrigeration leak detector is used to both check for leaks and to maintain the Freon level safely above the topmost capacitor.

2. Blumlein

The "fast section" of the accelerator consists of a folded, 3 conductor, parellel-plate transmission line, called a Blumlein after its inventor (See Figures 3 and 5a). The load for such a transmission line, be it a dummy resistive load for test and/or calibration, or the diode for actual beam production, is in series with the outer conductor in the approximate geometric center of the line. There are two such Blumleins at Cornell (See Figure 2) . Line no. 1, the topmost in the figure, has a characteristic impedance, Z_o, of 2 ohms. Line no. 2 has a Z_o of 1.75 ohms. The characteristic impedance, Z_o, of each section of a line is therefore designed to be either 1.75 ohms or 2 ohms depending on the line in use, and for a matched line, the load, Z_L, should be 2 Z_o or 3.5/4 ohms, respectively.

a) Operation

In operation, the Marx capacitors are charged to the desired voltage and discharged in series when the spark column is triggered. The Marx erects to full voltage and takes approximately a microsecond to charge

*The transparency allows open-shutter diagnostic photos to be taken should flashover occur.

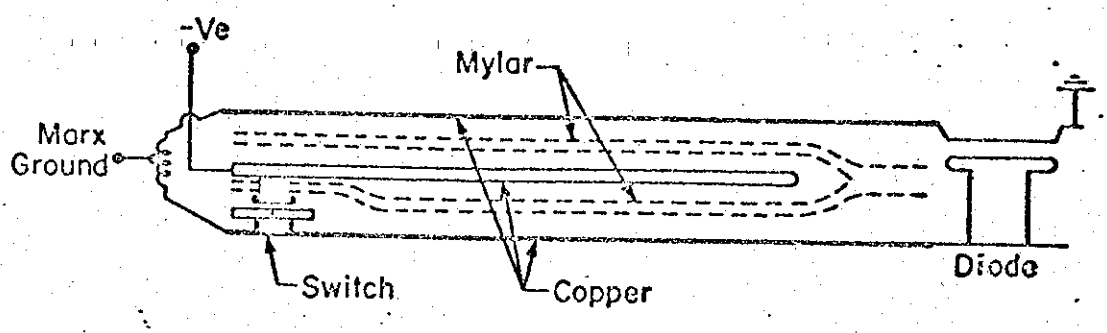

Figure 5a. Folded Blumlein Assembly

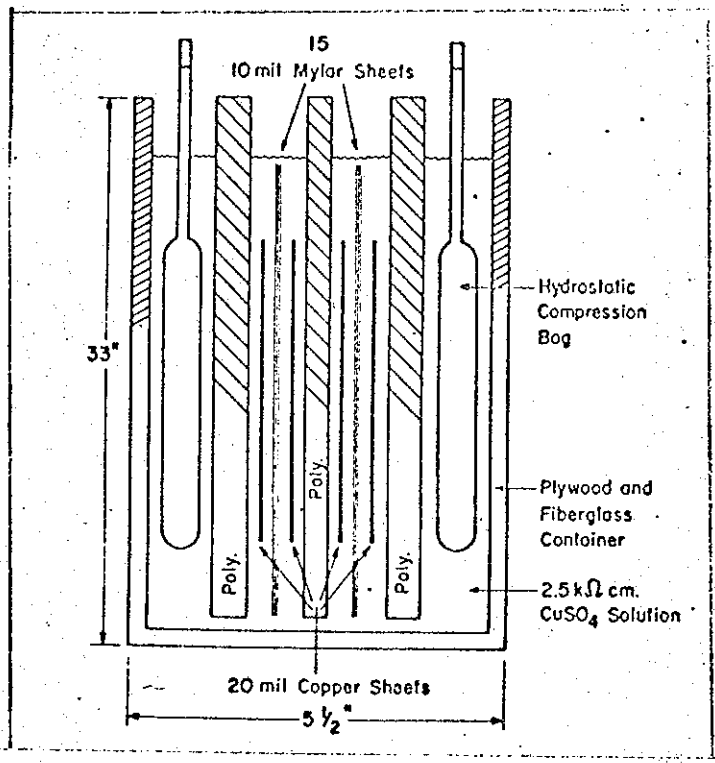

Figure 5b. Transmission Line Construction Details

the Blumlein center conductor negative, the outer conductors remaining reasonably well grounded. The solid dielectric pre-stabbed switch (See Section I.B.2.C.) located between the center and outer conductors at one end of the line (See Figures 1 and 3), becomes over-volted and closes in a few nanoseconds, thus placing a short on one end of the line while the other end remains open. A voltage pulse of about 50 nsec. duration is then felt across the load in a sequence such as indicated in Figures 6a,b and 7. It is seen that an outstanding advantage of the Blumlein configuration over a conventional transmission line is its' ability to deliver V_{input} rather than $V_{input}/2$ to the load.

b) Construction Details

Specifically, the Blumlein (See Figure 5) is composed of three 20 mil copper electrodes, approximately 15 feet long and 20 inches wide cemented to $\frac{1}{2}$ inch thick polyethylene sheets for support, and mounted on-edge (i.e. vertically) in a narrow (about 4 inch wide), 20 foot long PVC-cloth-lined tank. The tank is then filled a few cms above the lines with a water-copper sulfate ($CUSO_4$) grading solution of resistivity, ρ, about $2.5 \Big/ 4$ kilohm-cm. The spacing and positioning of the entire line assembly is maintained by means of PVC pressure bags filled with water. Although it is not shown in Figure 5 some outward flaring of the Blumlein outer conductors is required to accomodate the diode, thereby increasing the characteristic impedance of this section of the line.

The flaring also leaves a space between the line conductors and the input edge of the diode from which the grading solution must be carefully excluded by packing with polyethylene ($\epsilon \approx 2.5$) etc., or else the high dielectric constant ($\epsilon \approx 81$) of the solution would capacitively load the diode.

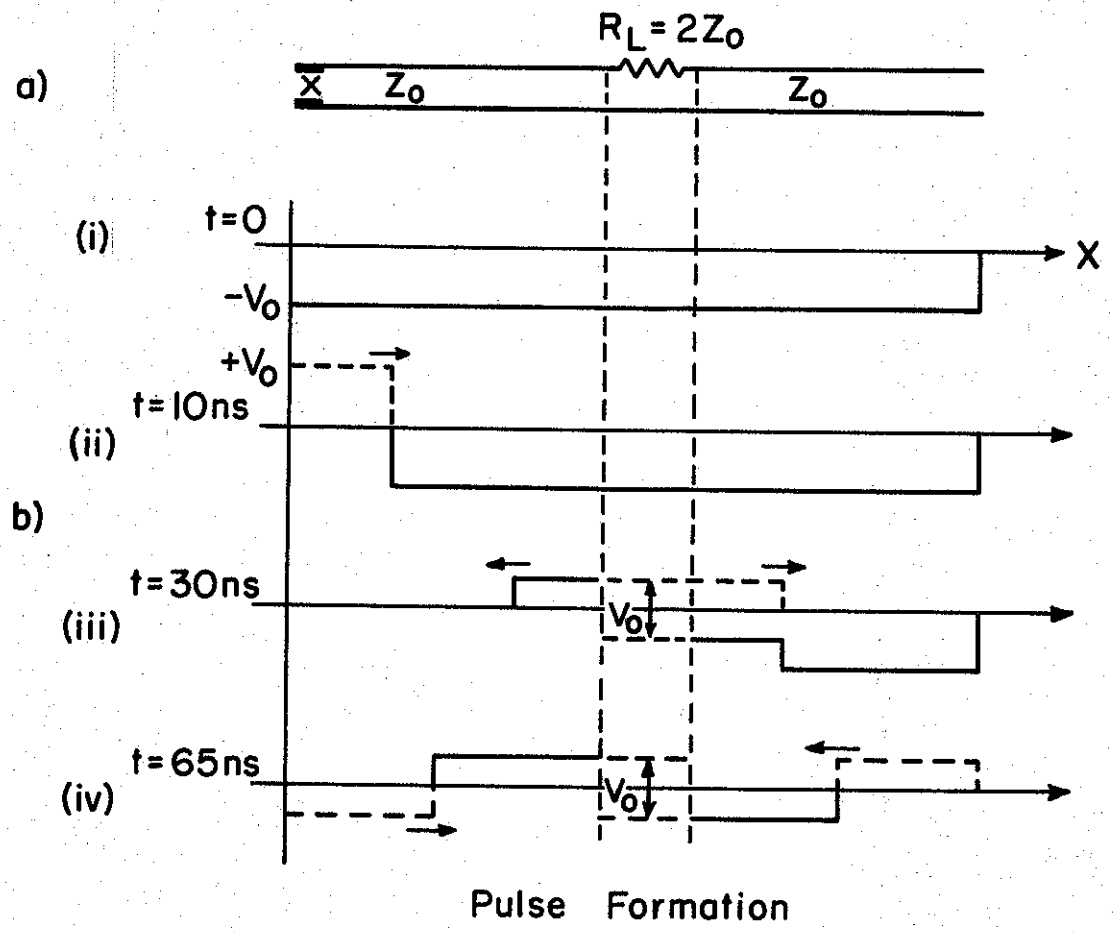

Fig. 6a. A Schematic of the Blumlein.

Fig. 6b. Blumlein Pulse Formation Sequence.
(i) Prior to Firing of Switch
(iii) Pulse Reaches Diode and Partially Reflects, Partially Transmits.
(iv) Pulses Reflect From Shorted (Switch) End and Open End of Line Eventually Cancelling So That Voltage Across Diode 0.

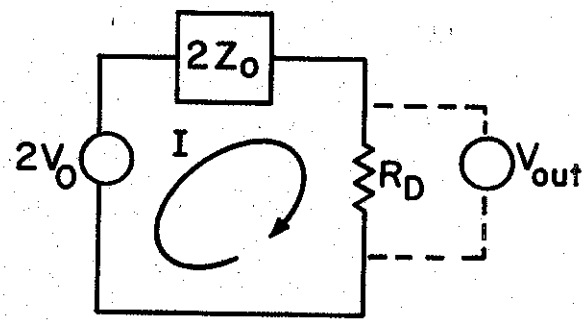

$$2V_O = V_D + I\,(2Z_O)$$

$$= 2V_O \frac{R_D}{R_D + 2Z_O}$$

For $R_D = 2Z_O$

$$V_{out} = V_O$$

(a) Blumlein Output Voltage for Pure Resistive Load

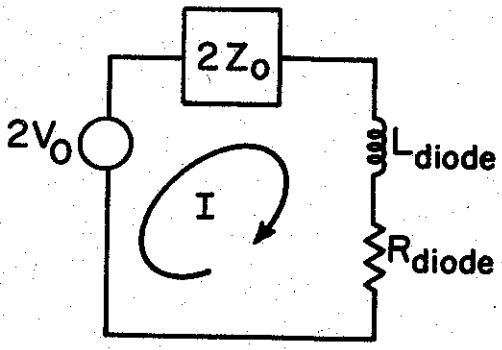

$$T_D = \frac{2.2L_D}{2Z_O + R_D}$$

$$I_D R_D = 2V_O - L_D \dot{I}_D - I(2Z_O)$$

(b) Pulse Rise Time, T_D, for Actual Diode Load

Fig. 7. Simplified Lumped Circuit Equivalents of the Blumlein for the First Voltage Pulse.

The water-$CUSO_4$ grading solution serves a number of purposes[1]:

1) It reduces the possibility of trapped air bubbles in the system which would lower the line breakdown voltage (if the water is de-aerated before use).

2) It efficiently clamps the electric stress onto the mylar dielectric by virtue of its high dielectric constant ($\epsilon \approx 81$) which remains essentially frequency independent to 3 GHz . This clamping is important because the relative dielectric strengths of mylar and water are about 8 Mv/cm and 200 KV/cm respectively, for time scales of a few tens of nanoseconds.

3) It reduces the field enhancement at the edges of the copper conductors of the Blumlein by smearing the potential (i.e. the potential diffuses out from the line edges in accordance with the diffusion equation). The required height of water above the line, x, is chosen such that the $V_{applied}/2$ equipotential line passes thru the water in such a way that the field gradient in the water does not exceed 200 KV/cm . The solution of the diffusion equation for a step voltage input yields[2]

$$x = 2\left(\frac{t}{R_s C_s}\right)^{1/2} \qquad (1)$$

where x = distance from conductor edge in cm ,

t = time (secs)

C_s = capacitance/square of dielectric between conductors (picofarads)

R_s = resistance/square of water-$CUSO_4$ solution (ohms)

In actual practice, R_s and x are adjusted to experimentally determine the optimum combination.

c) Solid-Dielectric Switch

To obtain a 50 nanosecond reasonably rectangular pulse of electrons from the diode, the voltage pulse applied to the diode must itself have a rise time less than 10 nsec.* The input impedance of the Blumlein is (3.5)/4 ohms and the charging voltage is 400 KV . This gives a current of 100 KA, and a 10^{-8} second rise time requires $\frac{di}{dt} = 1 \times 10^{13}$ amps/sec. These conditions preclude the use of normal gas switches and considerable attention has been given to the successful development of a "hot stabbed" solid dielectric switch by the AWRE Group.[1]

The fast dielectric switch used in the Cornel Accelerator must be replaced after each shot. It is a modified version of the AWRE effort, and consists of a slab of 1/4 inch thick polyethylene about 3 feet long and 8 inches wide. About 12 inches from the end of the slab, on center axis, a hot stabbing iron is used to imbed a 1/16 inch diameter stainless steel ball bearing at a depth determined by the desired breakdown voltage. (A stab-depth versus voltage breakdown curve had been generated by means of a high-voltage pulse transformer that was built for testing purposes.) A one inch square piece of adhesive-backed aluminum tape is cemented to the slab on each side of the stab point. The prepared switch is then inserted between the outside (positive) and center (negative) conductors of the Blumlein in a slotted aperture arranged so that the aluminum squares make electrical contact with the Blumlein conductors. When the Marx is fired the Blumlein begins to charge until the switch breaks down at the pre-calibrated voltage. A typical Marx output voltage waveform is shown in Figure 8a. The sharp discontinuity in the negative-going waveform indicates the breakdown point of the switch.

---

*See discussion in Chapter II on overall circuit rise times.

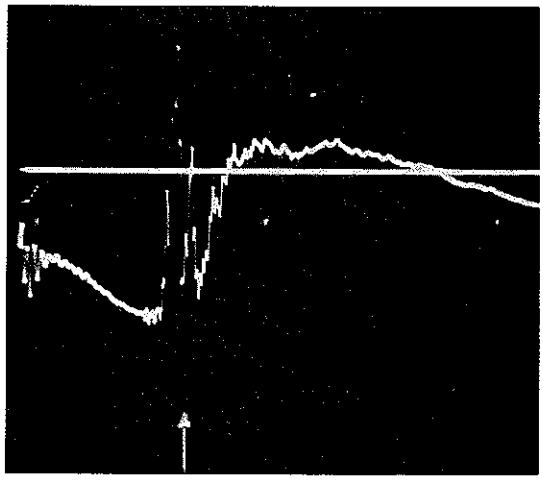

Fig. 8a. Typical Marx Voltage Trace - Shot #2, 10/29/68

$450 \frac{\text{nsec.}}{\text{cm}}$

Sharp Discontinuity (i.e. Arrow) Indicates Firing of Blumlein Solid Switch.

For $CuSO_4$ Resistor: Length Ratio = $\frac{201\text{cm}}{.72\text{ cm}} = 280/1$; Area Ratio = $\frac{2.4}{1}$

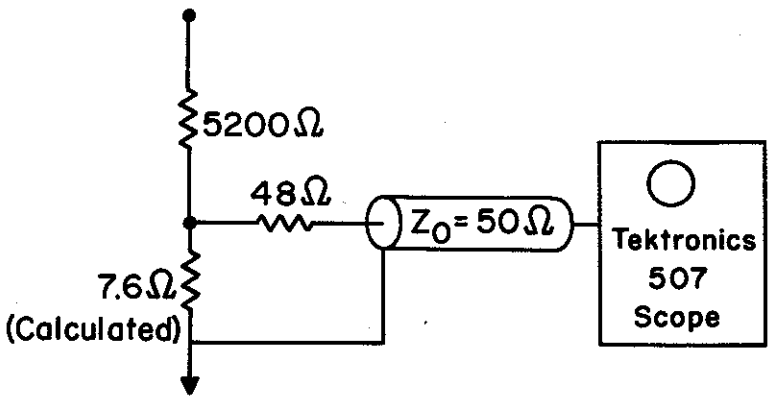

Attenuation Ratio:

$$\frac{5200}{7.6}\left(\frac{98}{50}\right) \approx \frac{1430}{1}$$

$$\frac{5200\Omega}{2.4\,(280)} = 7.6\,\Omega$$

Fig. 8b. Schematic Diagram of Marx Voltage Monitor.

The switches are normally operated with positive voltages applied to the stabbed side. If the polarity is reversed the required breakdown voltage increases by a factor of about 3[1] and there would be a highly increased probability of rupturing the mylar of the Blumlein, since its breakdown voltage is time dependent. If a switch fails to fire, the Marx generator continues to charge the system and a ringing condition exists which eventually reverses the polarity of charge on the transmission line. Since the breakdown strength of the water-copper sulfate grading solution is lower for positive polarity and the stress time has been increased by the ringing condition, a breakdown point may be reached that will result in severe mechanical damage to the system. An energy "dump gap" arrangement is used to avoid this eventuality (See Figure 3). Marx charging voltages are set 25% above the desired switch breakdown voltage while an adjustable spark gap is set to close at approximately 10% over the switch breakdown voltage. Should the switch not fire the unwanted energy is discharged through a critically damped circuit.

It is believed that field enhancement at the switch hole tip causes the local field to exceed the intrinsic strength of the remaining polyethylene (~ 8 Mv/cm). The air in the hole breaks down and conveys the high fields to the tip. Care is taken to prevent the Blumlein water from seeping into the switch hole because this would cause erratic switch breakdown and is likely to increase the switch rise time beyond acceptable limits.

An estimate of the switch inductance can be made by considering the spark channel to be the center conductor of a coaxial inductor where,

$$L_{SWITCH} = 2 \log_e \frac{b}{a} 10^{-9} \text{ henrys/cm} \quad . \qquad (2)$$

Where l = discharge path length ~ 0.1 cm

a = .01 cm

b = 15-20 cm (return path in switch box)

giving

$$L_{SWITCH} \simeq 2 \times 10^{-9} \text{ h} \quad .$$

Measurements by the AWRE group with a 200 KV, fraction of an ohm transmission line yielded $\sim 3 \times 10^{-9}$ h .

The Marx output waveform of Figure 8 is obtained by means of a $CUSO_4$ resistive voltage divider (See Figure 8b). This divider is approximately two meters in total length and has an area division ratio at the tap off section of 2.4, terminated in a carbon resistor network to give a total voltage division ratio of $\frac{1430}{1}$. Because this monitor is isolated from the Blumlein by the fixed Marx-Blumlein 2μh isolating inductors* of Figure 3 and an unknown amount of stray and lead inductance, a detailed test procedure was carried out to determine accurately the relationship between the Marx monitor voltage waveform and the actual Blumlein input voltage. The Marx monitor would serve primarily as a time marker and accurate calibration of its voltage division ratio would be of only secondary importance. The results of this procedure are now described.

3. The Marx-to-Blumlein Energy Transfer Process

A simplified schematic of the Marx-Blumlein electrical circuit is shown in Figure 9a. Upon erection, the Marx capacity, C_M, is equal to 0.5 μf/16 stages or .03 μf . The internal resistance of the Marx, R_M, may be measured by placing a current shunt across the 16 ICSE capacitors.

---

*Designed to act as a short circuit for the microsecond Marx pulse and as an open circuit for the much more rapidly rising (order of few nsec) Blumlein pulse. They thus isolate the Blumlein from the Marx after the switch fires, and prevent voltage reversal on the Marx capacitors.

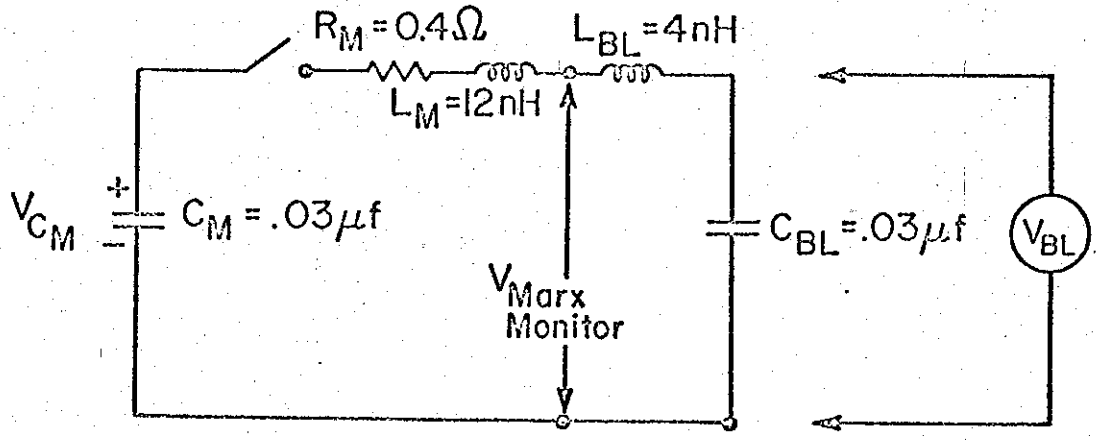

Fig. 9a. Simplified Marx-Blumlein Electrical Circuit.

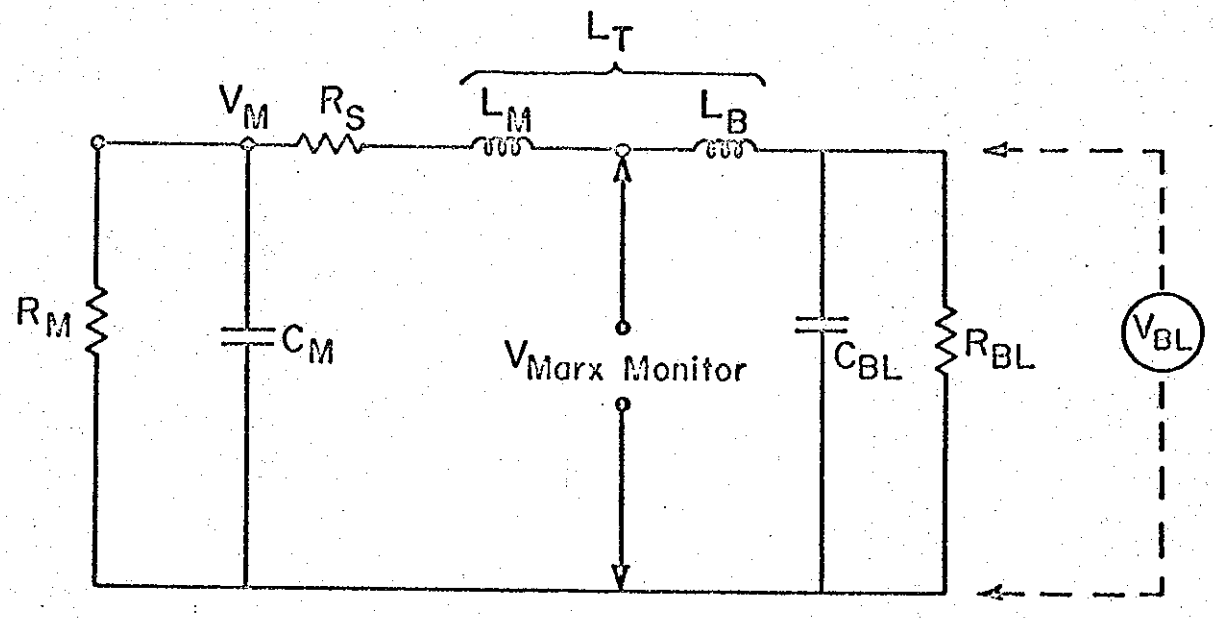

Fig. 9b. "Actual" Marx-Blumlein Electrical Circuit

discharging the capacitors and monitoring the RC decay time. For $C_M = .03\ \mu fh$ R_M is estimated at 0.4Ω, L_M, L_{BL} and C_{BL} are estimated from geometry to be $12\ \mu h$, $4\ \mu h$ and $.03\ \mu f$ respectively. Applying Kirchoff voltage law to the circuit of Figure 9a we have:

$$\frac{V_{C_M}}{S} = I(s)\left[R + S(L_M + L_{BL}) + \frac{1}{S}\left(\frac{1}{C_M} + \frac{1}{C_{BL}}\right)\right] \qquad (3)$$

or

$$I(S) = \frac{V_{C_M}}{S^2 L_T + RS + \frac{1}{C_T}} = \frac{V_{C_M}/L_T}{S^2 + S\frac{R}{L_T} + \frac{1}{L_T C_T}} \qquad (4)$$

where

$$L_T = L_M + L_{BL} \approx 16\ \mu h \qquad (5)$$

$$C_T = \frac{C_M C_{BL}}{C_M + C_{BL}} \approx .015\ \mu f \qquad (6)$$

$$I(S) = \frac{V_{C_M}}{L_T}\ \frac{1}{(s+a)(s+b)} \qquad (7)$$

$$a = \frac{-R_M}{2L_T} + \left(\frac{R_M^2}{4L_T^2} - \frac{1}{L_T C_T}\right)^{1/2} \qquad (8)$$

$$b = \frac{-R}{2L_T} - \left(\frac{R_M^2}{4L_T^2} - \frac{1}{L_T C_T}\right)^{1/2} \qquad (9)$$

$$I(t) = L^{-1} I(s) = \frac{V_{C_M}}{L_T}\ \frac{e^{-at} - e^{-bt}}{b - a} \qquad (10)$$

Since

$$\frac{R_M^2}{L_T^2} < \frac{1}{L_T C_T} \qquad (11)$$

in the order of 0.4Ω to 65 Ω the radical portion of a and b is imaginary.

Letting

$$\beta = \frac{1}{L_T C_T} - \frac{R_M^2}{4L_T^2} \tag{12}$$

we have

$$I(t) = \frac{V_{C_M}}{L_T} e^{-\frac{R_M}{2L_T}t} \frac{e^{j\beta t} - e^{-j\beta t}}{2j\beta} \tag{13}$$

or

$$I(t) = \frac{V_{C_M}}{\beta L_T} e^{-\frac{R_M}{2L_T}t} \sin \beta t \tag{14}$$

or

$$I(t) = \frac{V_{C_M}}{\beta L_T} e^{-1.25 \times 10^4 t} \sin 2 \times 10^6 t \tag{15}$$

For RM = 0 , (the lossless case) we have

$$I(t)_{\text{lossless}} = \frac{V_{C_M}}{\beta L_T} \sin \beta t \quad , \tag{16}$$

from which $V_{C_{BL}}$

$$V_{C_{BL}} = \frac{I(t)}{C_{BL}} = \frac{1}{C_{BL}} \int_0^t \frac{V_{C_M}}{\beta L_T} \sin \beta t \, dt \tag{17}$$

or

$$VC_{BL_{peak}} = \frac{1}{C_{BL}} \left[\frac{V_{C_M}}{C_{BL} \beta^2 L_T} - \cos \beta t \right]_0^{\pi} \tag{18}$$

$$V_{C_{BL_{pk}}} = 2V_{C_M} \frac{C_M}{C_{BL} + C_M} \tag{19}$$

If C_{BL} were very small, $V_{C_{BL_{pk}}} \approx 2\, V_{C_M}$. For our case since $C_M \approx C_{BL}$, we expected from this simplified analysis,

$$V_{C_{BL,peak}} \cong V_{C_M} \quad . \tag{20}$$

Having found $I(t)$, $V(t)_{\substack{MARX \\ MONITOR}}$ and $V_{C_{BL}}(t)$ may be determined to be:

$$\frac{V_{C_M}}{4}\left(2.0 - 1.06 \cos 2 \times 10^6\, t\right) \cong V_{\substack{MARX \\ MONITOR}}(t) \tag{21}$$

$$V_{C_{BL}}(t) \approx \frac{V_{C_M}}{2}\,(1 - \cos 2 \times 10^6\, t) = V_{BLUMLEIN} \tag{22}$$

If switch firing time is determined from the Marx monitor trace, the Blumlein and Marx monitor voltages may be related by equations 21 and 22 and, theoretically at least, the input voltage to the diode (V_D) is known.

A circuit which more closely approximates our actual situation is shown in Figure 9b. Detailed measurements and analysis of this circuit are reported on in references 3 and 4. A brief summary is presented.

1. The voltage on a single Marx capacitor was monitored both by the usual panel voltmeter and an electrostatic voltmeter having a 1% full scale accuracy. It was assumed that at $t = 0$, the Marx voltage $V_M(0)$ was equal to 16 times the charge on any one capacitor.
2. The Marx monitor $(CUSO_4)$ resistance (> 6 K Ω) was assumed to be infinite in comparison with other shunt resistances.
3. R_{BL} and C_{BL} are time dependent quantities - subject to the diffusion effect of the $CUSO_4 - H_2O$ grading solution.

Since C_M was the only well known circuit parameter the following shots were made:

a) C_{BL} and R_{BL} were short circuited by means of low inductance (wide) copper straps. The decay constant of the Marx monitor waveform was used to determine $R_M = 111\ \Omega$ and the waveform period gave $L_T = 13.6$ nh, by using $T = \sqrt{LC}$.

b) A non-stabbed switch was used to accomplish open-circuit ringing of Marx generator into the Blumlein. The resultant waveform was used to estimate the damping constant resulting from C_{BL} and R_{BL} .

A combination of an analysis similar to that given above for Figure 9a and the experimentally derived constants led to

$$V_M = .516\ V_M(0)\ (1-e^{-1.86 \times 10^5 t}\ (.333)\ \cos\ 2.187 \times 10^6 t)e^{-1.28 \times 10^5 t} \quad (23)$$

$$V_{BL} = .516\ V_M(0)\ \ (1-e^{1.86 \times 10^5 t}\ \cos\ 2.187 \times 10^6 t)e^{-1.28 \times 10^5 t} \quad (24)$$

Figure 10 is the resulting plot of actual Blumlein voltage (V_{BL}) (as a percentage of Marx voltage at $t = 0$ ($V_M(0)$), as a function of the time from Marx erection to switch breakdown. One can now accurately fix the Blumlein (hence diode) voltage even though the monitoring system is somewhat isolated electrically from the Blumlein. The figure also includes data derived from an analogue circuit which was built by M. Ury[3] to verify the analysis.

An estimate of the Marx-Blumlein energy transfer efficiency at 100 KV and $\beta t = \pi$ radians, or peak Blumlein voltage, is:

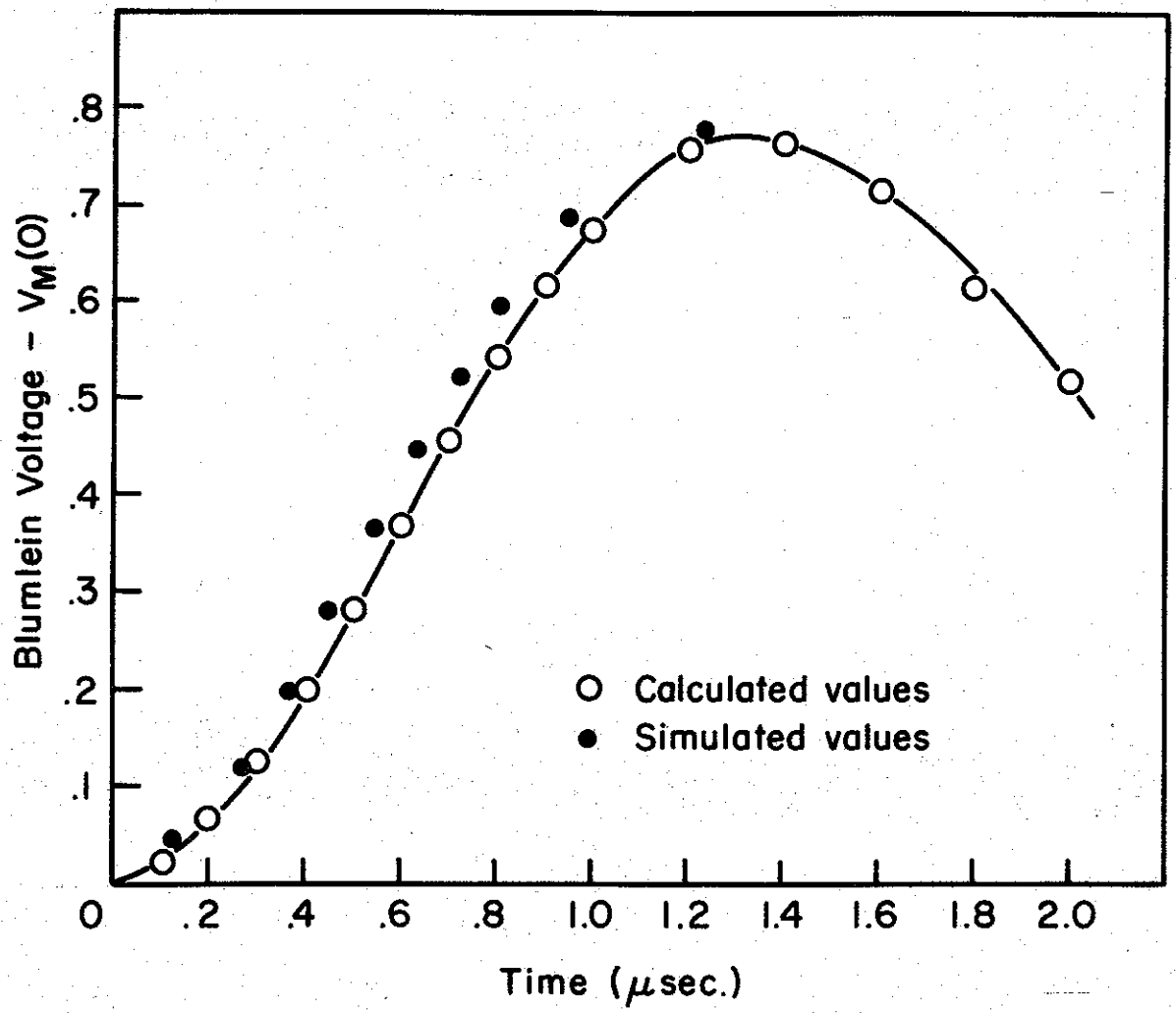

Fig. 10. Plot of Actual Blumlein Voltage Vs. Time From Marx Erection to Switch Breakdown.

Marx Energy ($t = 0$)	Blumlein Energy ($\beta t = \pi$)
$\frac{1}{2}\ C\ V_M(0)^2$	$\frac{1}{2}\ C\ V_{BL}^2$
$\frac{1}{2}\ (.0312)(10^5)^2$	$\frac{1}{2}\ (.0292)(.77 \times 10^5)^2$
155 Joules	86 Joules

i.e. 55.5% of the available energy may be transferred.

CHAPTER II - OPERATIONAL CHARACTERISTICS OF THE FIELD EMISSION DIODE

A. GENERAL DESCRIPTION OF DIODE

The 50-nsec high voltage pulse from the Marx-Blumlein combination discussed in Chapter I is applied across the anode-cathode gap of a field emission diode of special design. Electrons, field emitted from the surface of a "plasma" cathode, are accelerated across the anode-cathode (A-K) gap and reach relativistic velocities. Then they are either stopped by bombarding a thick (.250 inch) aluminum target at the anode plane or are extracted from the diode by penetrating a thin (.001" or less) metallic foil anode and emerge into an external drift tube to form a high current relativistic electron beam. The drift chamber length and pressure and the type and thickness of the metallic anode foils are easily varied. A foil stretching structure ensures parallel-plane geometry between cathode and anode.

The diode consists of two 5/8-inch thick by 20-inch diameter aluminum disks, separated by either three or four 1-inch thick lucite spacers which in turn are partly separated by 1/8-inch thick aluminum spacer rings to form a capacitively graded structure (See Figures 11a and 11b).

The cathode is attached to the cathode plate by a removable spacer arrangement that allows adjustment of the A-K gap. The "plasma" cathode is a solid brass disk 4.0 inches in effective diameter and 5/8 inches thick, with rounded edges to avoid field enhancement. The emitting surface contains about 200 conical indentations or "studs" 1/8 inch in diameter at the cone base. The holes may be filled with liquid lucite (or epoxy) which is allowed to harden. The surface is then faced off and polished.

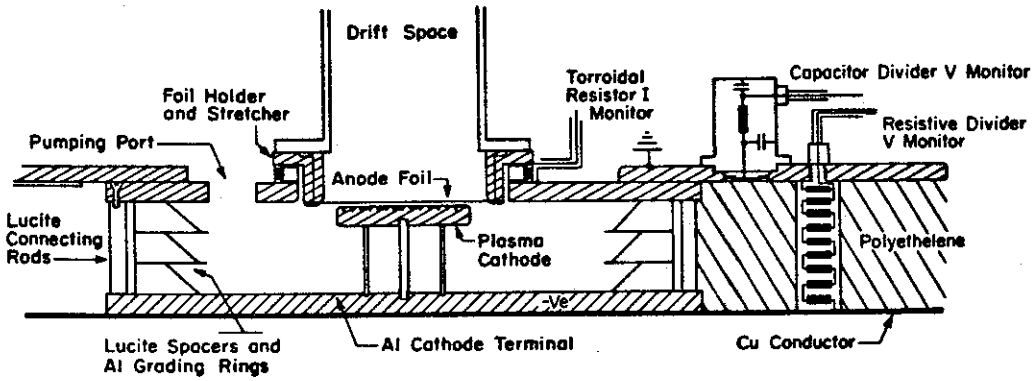

Fig. 11a. Diode Assembly (Approx. 1/10 full size)

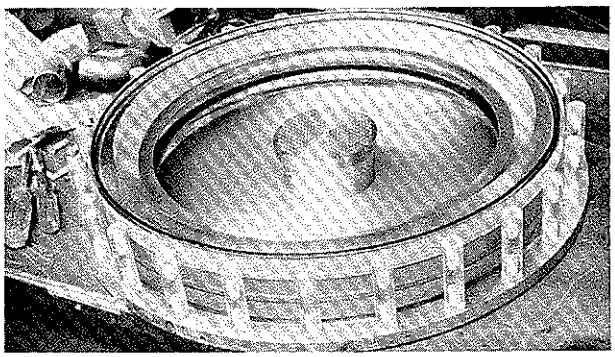

Fig. 11b. Field Emission Diode Being Assembled (Anode Plate Removed)

The anode plate has ports for beam extraction, for a 2 inch diffusion pump (which is mounted directly on the plate to maximize pumping conductance), and for a combination thermocouple-Penning discharge gauge to measure diode pressure.

B. MONITOR DESCRIPTION AND CALIBRATION

Diode voltage is monitored in two ways, (1) by means of a low-inductance carbon resistance voltage divider, consisting of a potted assembly of 200, 10 ohm, 2 watt resistors (Figure 11a) with a 50-ohm tap-off section which is resistance-capacitance (RC) balanced, and (2) by means of a capacitive voltage divider, called a Shipman probe (Figure 12), which is capable of 2 nsec resolution. The Shipman probe must be carefully shielded against RFI due to its low level-output ($\frac{1v}{300\ KV}$).

Calibration of the resistive voltage-monitors is accomplished by placing the monitor between the plates of a mockup model of the Blumlein, pulsing the input with a 40 nsec, 1500 volt (50 Ω load) square wave and monitoring both the input and output pulses with fast (2.4 nsec) rise time oscilloscopes. Appropriate adjustments are made on the balancing capacitors until overshoot in the output waveform is minimized. The monitor is then placed in the actual Blumlein, with the diode open circuited to remove the diode inductance, and final tuning accomplished while open circuit test shots are made.

Diode current is measured by means of a single-loop $\dot{B}$ probe and simultaneously by a current shunt consisting of either a saturated $CUSO_4$ solution (Figure 13) or a belt of 200, 10 ohm, 1/2 watt resistors (Figure 11a) in parallel.

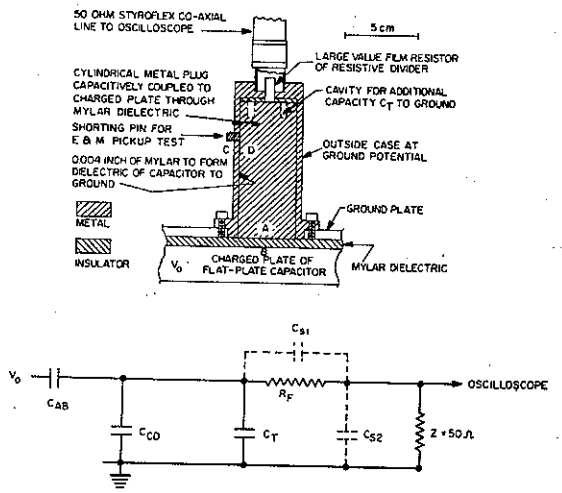

Figure 12. Schematic Diagram of the NRL Capacitive Voltage Divider (After G.E. Leavitt, J.S. Shipman, Jr. and I.M. Vitkovitsky "Ultrafast High Voltage Probe" Review of Scientific Instruments Vol. 36, No. 9, 1371-2, September 1965)

$$V_{OUTPUT} = V_o \frac{C_{AB}}{C_{CD} + C_T + C_{AB}} \left(\frac{50}{R_F + 50}\right)$$

$$T = (C_{CD} + C_T + C_{AB})(R_F + 50)$$

For Cornell Case $C_T = 0$, $C_S \approx 10$ pf, $R_F = 1K\Omega$

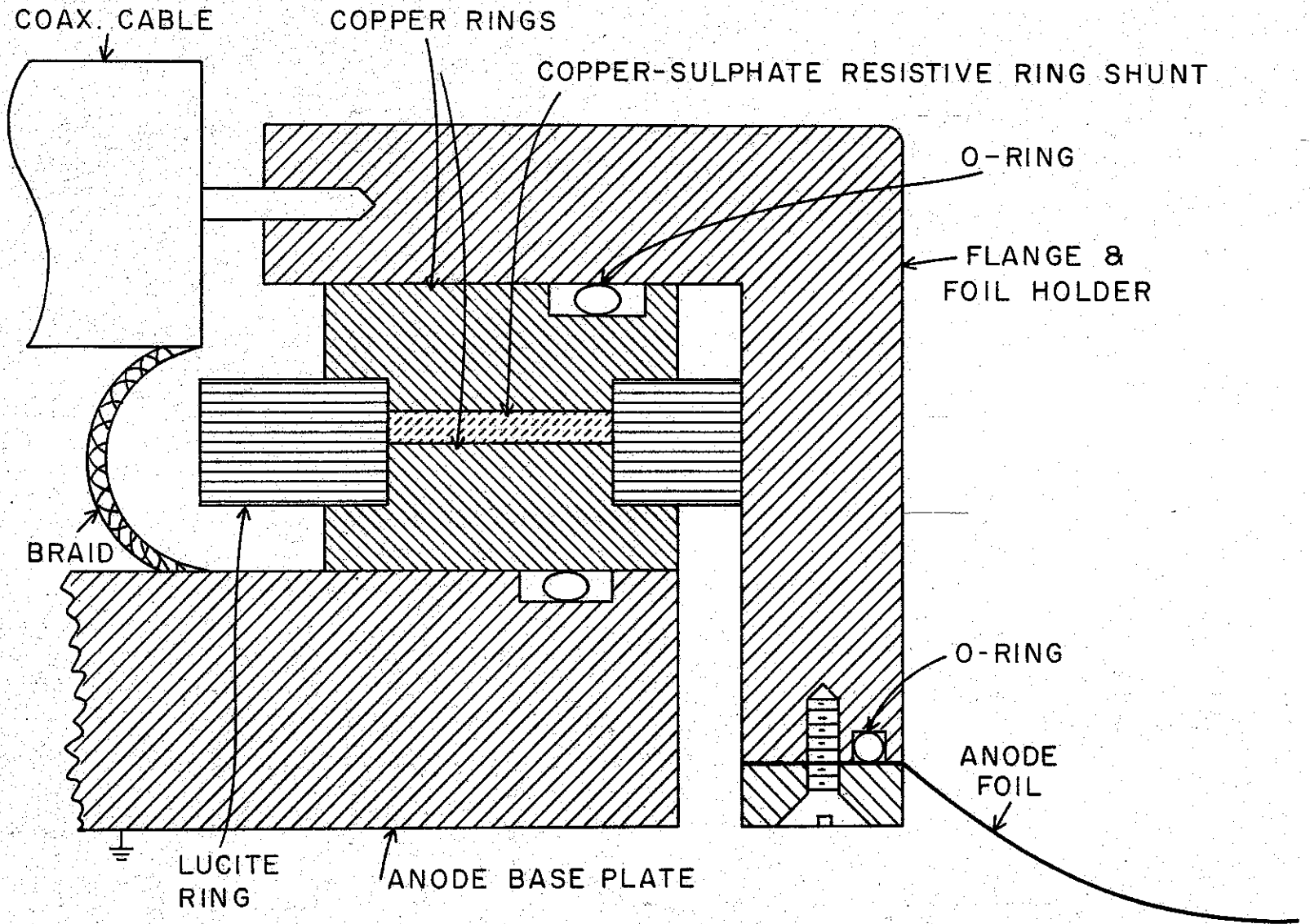

Fig. 13. Copper Sulfate Diode Current Monitor

The single loop $\dot{B}$ probe is located at a fixed radial distance from the cathode axis and so aligned that the magnetic field lines (caused by the diode current) threaded the loop. This changing magnetic flux ϕ, generates a voltage, V(t), (seen across a terminating resistor R) that induces a reverse current in the loop which in turn produces a magnetic flux which cancels the applied flux. The loop current is shown to be proportional to the diode current in the following manner:

$$V(t) = \frac{d\phi}{dt} - L\frac{di}{dt} = iR \tag{25}$$

Solving we have,

$$V(t) = Ri(t) = Ce^{-t/\tau} + \frac{R}{L} e^{-t/T}\int_0^t \frac{d\phi}{dt'} e^{t'/T}\, dt' \tag{26}$$

where $t = L/R$. For $i(t) = 0$ at $t = 0$, $C = 0$. Therefore

$$V(t) = \frac{e^{-t/T}}{T}\int_0^t \frac{d\phi}{dt'} e^{t'/T}\, dt' \tag{27}$$

For $T \gg t$

$$e^{t'/T} \approx e^{t/T} \approx 1 \quad \text{and} \quad V(t) = \frac{1}{T}\phi(t) \tag{28}$$

But

$$\phi(t) = B(t)\, A = A\left(\frac{\mu_o}{2\pi}\right) \frac{I(t)}{r} \tag{29}$$

where $I(t)$ = diode current

A = loop area

r = distance from loop center to electron beam center.

We have then

$$V(t) = \frac{1}{T} A \left(\frac{\mu_o}{2\pi}\right) \frac{I(t)}{r} \tag{30}$$

or the measured probe voltage, V(t), is proportional to the diode current, I(t).

Calibration of the current shunts with a pulser is difficult to do directly because of their low resistance (~.050Ω) . The $CUSO_4$ shunt resistance is estimated from the solution conductivity (measured on a G.R. resistance bridge) and the known geometry and volume of the solution enclosure. The d-c resistance of the carbon belt resistor was accurately measured on a bridge.

A front view of the resistor-belt shunt and the 24 possible tap off points on its periphery (numbered clockwise) is shown in Figure 14. Figure 15 is a plot of normalized current versus tap-off position on the belt resistor and indicates the expected asymmetry in the diode current due to the asymmetrical feed* design of the Cornell diode. For normal shots, position No. 1 (which is very close to the average position) is used. A calibration check of the $\dot{B}$ current probe and positions 1 and 3 of the resistive belt shunt is shown in Figure 16. From the known calibration of the resistive shunt ($34 \frac{KA}{cm}$) , the calibration of the $\dot{B}$ probe is also determined to be approximately $34 \frac{KA}{cm}$.

The parallel plate (open) Blumlein configuration, the solid dielectric switch, and the Marx-discharge spark column are all sources of considerable RF noise. All monitor cables (coax) used are of the doubly-shielded braid type or have a solid outer conductor to reduce noise pickup, and the oscilloscopes are mounted inside a doubly-shielded fine mesh copper screen room. The coax cables enter the screen room at a common point to reduce loop currents, and all power supplies are isolated from the 60 Hz input lines by large inductors. Voltage division ratios of all signal voltages are selected to optimize the

---

*For further discussion of this point see Chapter IV.

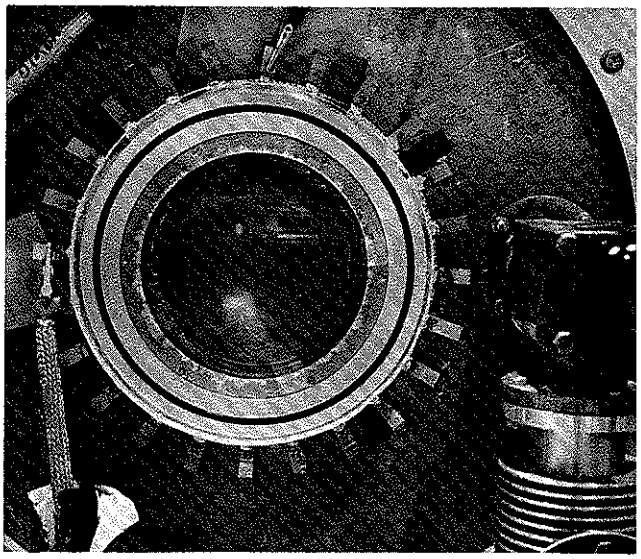

Fig. 14. Front View of Field Emission Diode Showing:
Plasma Cathode
Quartz and Lucite Cover Plates
24 Tap-Off Resistive Current Shunt
Diffusion Pump (Right-Center)
Shielded Signal Cables

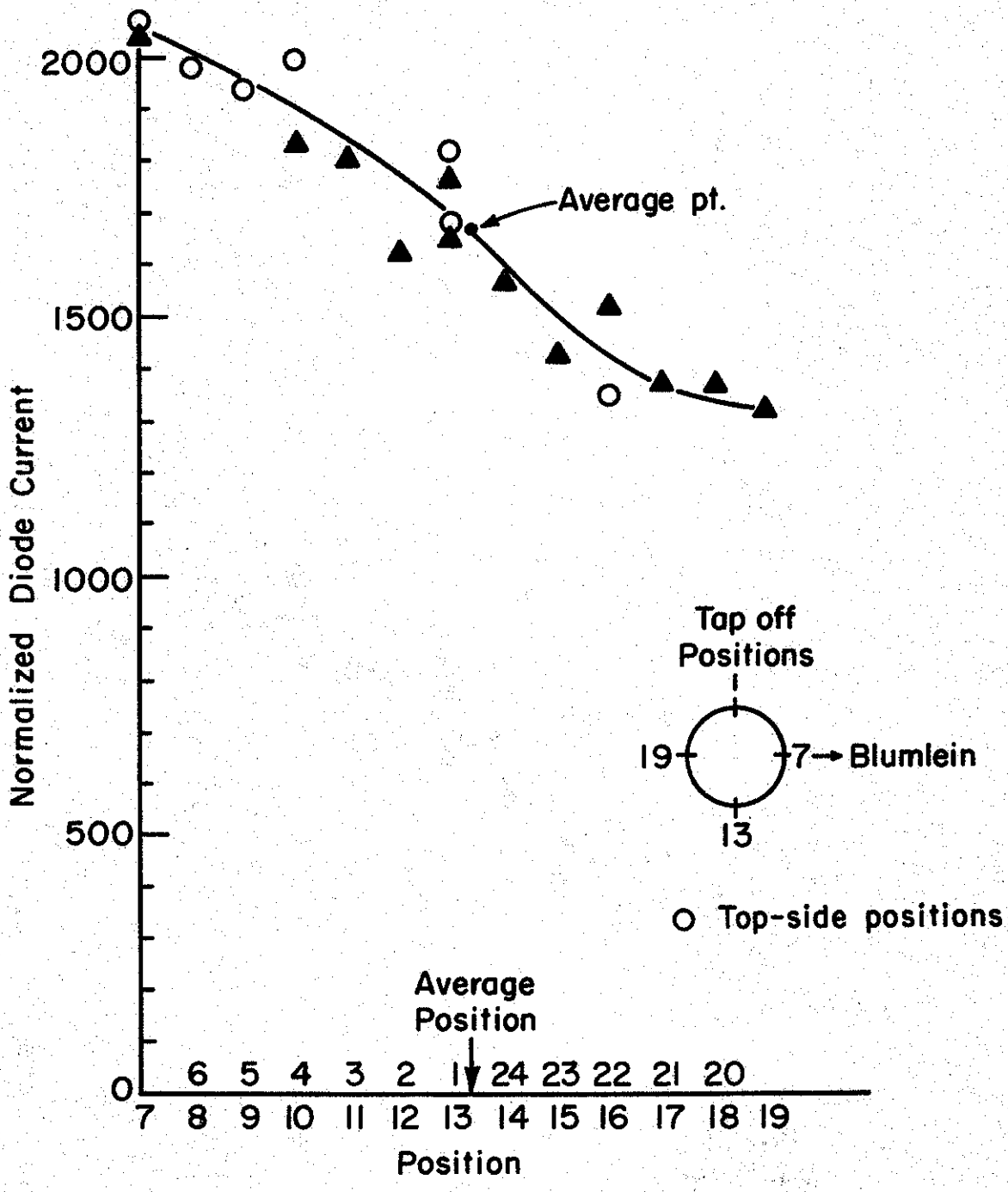

Fig. 15. Normalized Diode Current Versus Resistive Belt Tap-Off Position

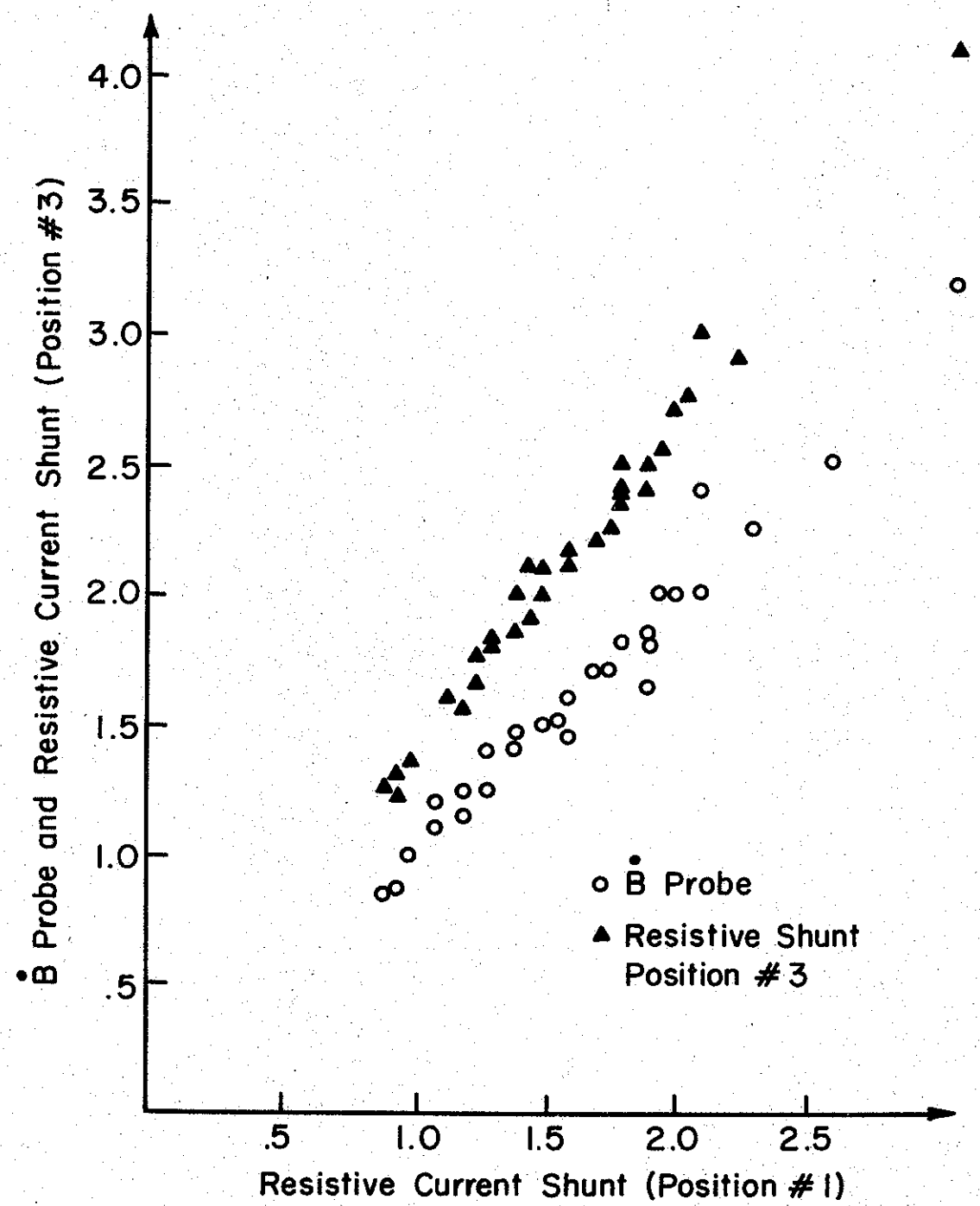

Fig. 16. "Line 2 Current" (Position #1) Vs. $\dot{B}$ Probe and Position #3. (All Units Are cm on Film) - Calibration of Resistive Monitor ≈ 34 KA/cm.

S/N ratio; the absolute magnitude of such signals being determined by the attenuators and oscilloscopes available.

C. DIODE DESIGN CONSIDERATIONS

1. Lucite Spacer Design

A major consideration in the design of a diode intended to utilize pulse lengths of the order of a few tens of nanoseconds is the minimization of diode inductance. This is so because the diode pulse rise time T_D (10% to 90%) is approximately $2.2L_D/2Z_o + R_D$, and in general it is desirable that R_D be of the order of a few ohms or less so that currents in the hundreds or thousands of kiloamps may be obtained at voltages less than a megavolt. Diode inductance, L_D, is given by

$$L_D = 2 \ell \log_e \frac{b}{a} 10^{-9} \text{ henrys} \qquad (31)$$

where

ℓ = diode length, cm

b = diode outer radius, cm

a = cathode radius, cm

Since b is fixed by the number of ports required for the experiment, and a is fixed by the required diode impedance, Z_D, ℓ remains for possible minimization.

Considerable experimental research effort has therefore been expended in the selection of the optimum dielectric spacer material and geometry to provide the largest breakdown voltage possible per unit length of material. In addition, the tube may require demounting after each shot should the anode foil be ruptured; to minimize pump down times after re-assembly the diode must operate properly at relatively high pressure (10^{-3} torr).

An extremely successful ad hoc approach to these problems was devised by the AWRE group[5] when they showed that lucite spacers angled at +45° (to prevent an electron multipactor effect) and coated with silicon diffusion pump oil (such as DC-704) could withstand breakdown fields (E_B) of approxi ately 175-200 KV/cm (See Figure 17a,b). It was also shown that E_B was independent of:[5]

a) Tube envelope diameter, if this be as great or greater than the anode-cathode separation, d.

b) The material of which the electrodes are made.

c) The identity of the residual gas in the envelope. (E_B slightly higher for electro-negative gases)

d) The gas pressure, provided this be lower than a well-defined threshold (See Figure 18). (It is worth noting here that the p-d product is <u>not</u> an important <u>surface flashover</u> parameter.)

Using the data of reference 5, the tube envelope shown in Figure 11a,b was evolved. The 0 rings which provide the vacuum seal are shown in Figure 11b. The envelope successfully withstood input voltages up to 500 KV for hundreds of shots without breakdown across the insulator surfaces.

It is believed that the positive angling of the insulators prevents primary electrons emitted from the wall or electrodes from re-encountering the wall and hence from multiplying and eventually causing flashover. Negative angles would accentuate the "multipactor" effect. The primary electrons are believed to be caused by field emission from the insulator surfaces near the anode,[5] caused by field enhancement due to polarization of the dielectric, although other explanations such as thermionic emission have also been offered.[6]

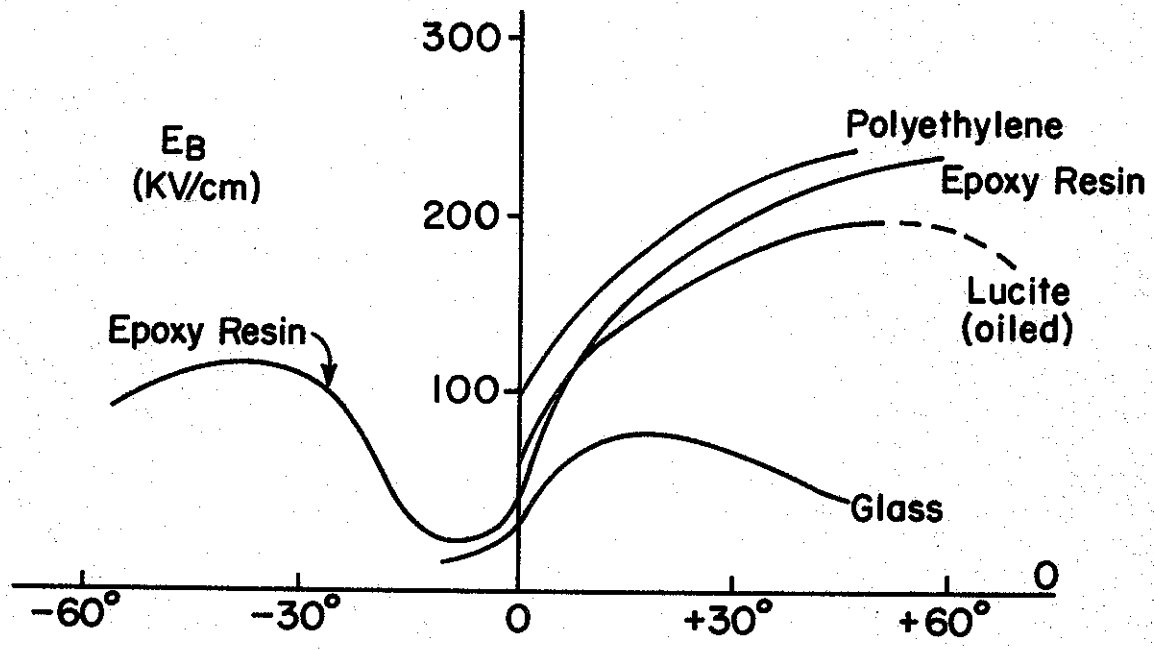

Fig. 17a. Breakdown Strength of Oiled Lucite Insulators Versus Angle of Attack. (After Reference 5)

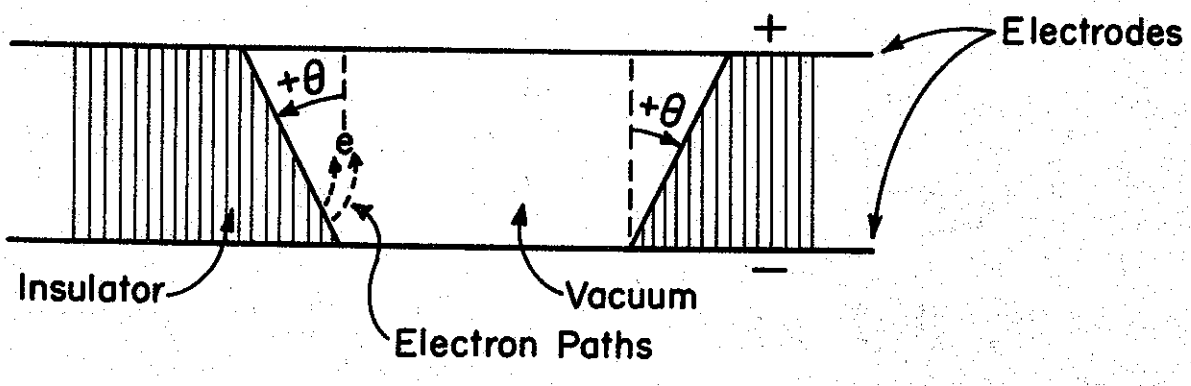

Fig. 17b. Definition of Positive θ(Angle of Attack)

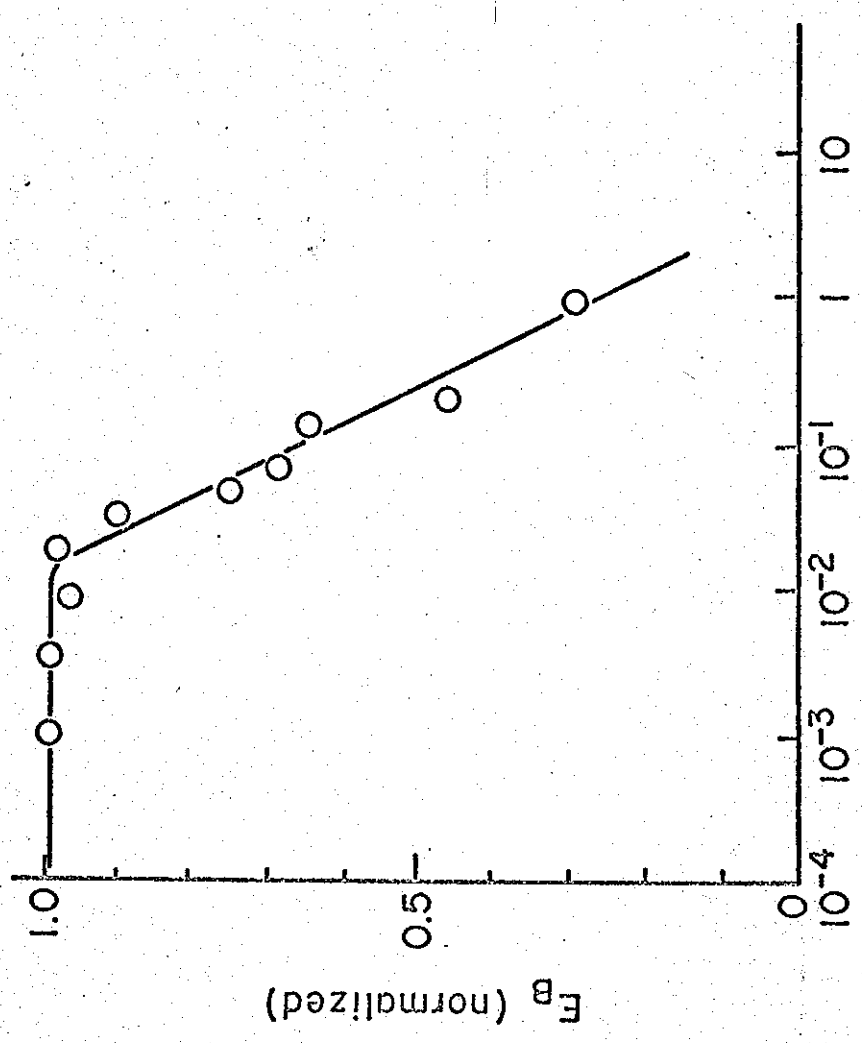

Fig. 18. Pressure Dependence of E_B for 1" Oiled Lucite Envelope (30 ns pulse) (After Reference 5)

2. Diode Inductance - Calculated Versus Experimental

Using Equation 31, $L_D \cong 28$ nh for the Cornell diode with:

ℓ = 4.0" = 10 cm

b = 16.0" = 40 cm

a = 4.0" = 10 cm

To determine the diode inductance experimentally, shots were made with a copper cylinder (of the same diameter (4.0") as usual cathode) placed between the anode-cathode plates. This short circuit served to remove the resistive component, R_D, from the diode impedance ($Z_D = R_D + jL_D$). Since

$$2V_o = V_D + I(2Z_o) \tag{32}$$

$$2V_o = I_D R_D + L_D \dot{I}_D + I(4\Omega) \tag{33}$$

$$I_D R_D = 2V_{\substack{MARX \\ MONITOR}} - L_D \dot{I}_D - I(4\ \Omega) \tag{34}$$

Using the oscilloscope traces of Figure 19 for V_{MARX} and I_D and setting $R_D = 0$ we have:

$$0 = 2(174KV) - L_D \frac{95KA}{40\ nsec} - 95\ Ka\ (4\ \Omega) \tag{35}$$

$$0 = 348 - 380 - 2.37\ L_D \tag{36}$$

$$13.5nh = L_D \tag{37}$$

or alternatively, $L_D \left(\frac{95KA}{40\ nsec}\right) = 30$ KV (from V_D trace)

$$L_D = 12.6\ nh \tag{38}$$

Considering the difficulties involved in accurately estimating the coaxial outer radius (i.e. return current path of the diode) the agreement within a factor of 2 is considered very satisfactory, but is not

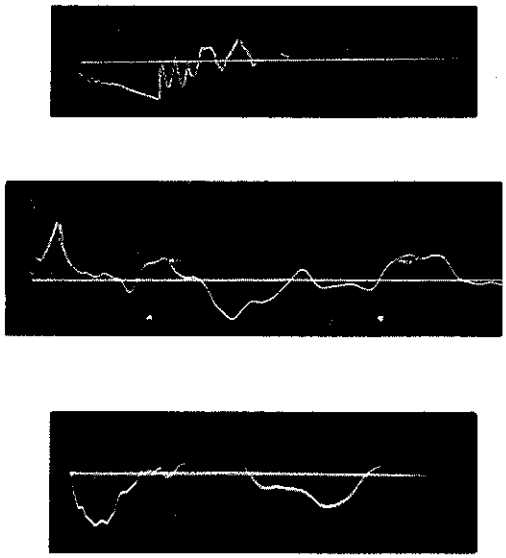

Fig. 19. Short Circuit Test Oscilloscope Traces
Shot #1, 5/8/68

Top Trace (V_{MARX})	507 Tektronics Scope	296 $\frac{KV}{CM}$	0.5 $\frac{\mu sec}{CM}$	V_{MARX}	$\cong$174 KV
Center Trace (V_{DIODE})	507 Tektronics Scope	30 $\frac{KV}{CM}$	100 $\frac{nsec}{CM}$	$V_{DL_{PK}}$	$\cong$30 KV
Bottom Trace	519 Tektronics Scope	119 $\frac{Ka}{CM}$	100 $\frac{nsec}{CM}$	$I_{D_{PK}}$	$\simeq$95 Ka

entirely unexpected due to the slowly varying $\log_e \frac{b}{a}$ term in equation 31.

The oscilloscope treces of Figure 19 which were obtained prior to the Marx to Blumlein energy transfer analysis given in Chapter I may also be used to cross check the Marx and diode monitors, as follows:

For a Short Circuit Test Shot $R_D \longrightarrow 0$, and if one measures peak current $\dot{I}_D \longrightarrow 0$, $L_D \dot{I}_D \longrightarrow 0$ and therefore:

$$I_{\substack{\text{SHORT CIRCUIT} \\ \text{(CALCULATED) PEAK}}} = \frac{V_{MARX}}{Z_o} = \frac{2(174KV)}{4\ \Omega} = 87\ KA \quad (39)$$

versus

$$I_{\substack{\text{SHORT CIRCUIT} \\ \text{(MEASURED) PEAK}}} = 95\ KA \quad (40)$$

or, the monitors agree within approximately 10% .

3. Expected Circuit Rise Times and Open Circuit Test Shots

The equivalent circuit which determines the rise time , T_D, of the diode voltage is shown in Figure 20.

$$V_{\substack{\text{RESISTIVE} \\ \text{VOLTAGE MONITOR}}} = \frac{R_{TAP\text{-}OFF}}{R_{TAP\text{-}OFF} + R_{MONITOR}} , \quad (41)$$

if $R_{MONITOR}\, C_{MONITOR} = R_{TAP\text{-}OFF}\, C_{TAP\text{-}OFF}$ for all frequencies of interest. This condition is approximately realized by considering the paths of the electric field lines in the diode and appropriately positioning the monitor, and/or by capacitively tuning the tap-off section with a lumped, variable capacitance. The diode voltage rise time should then be controlled by the longest of the following times:

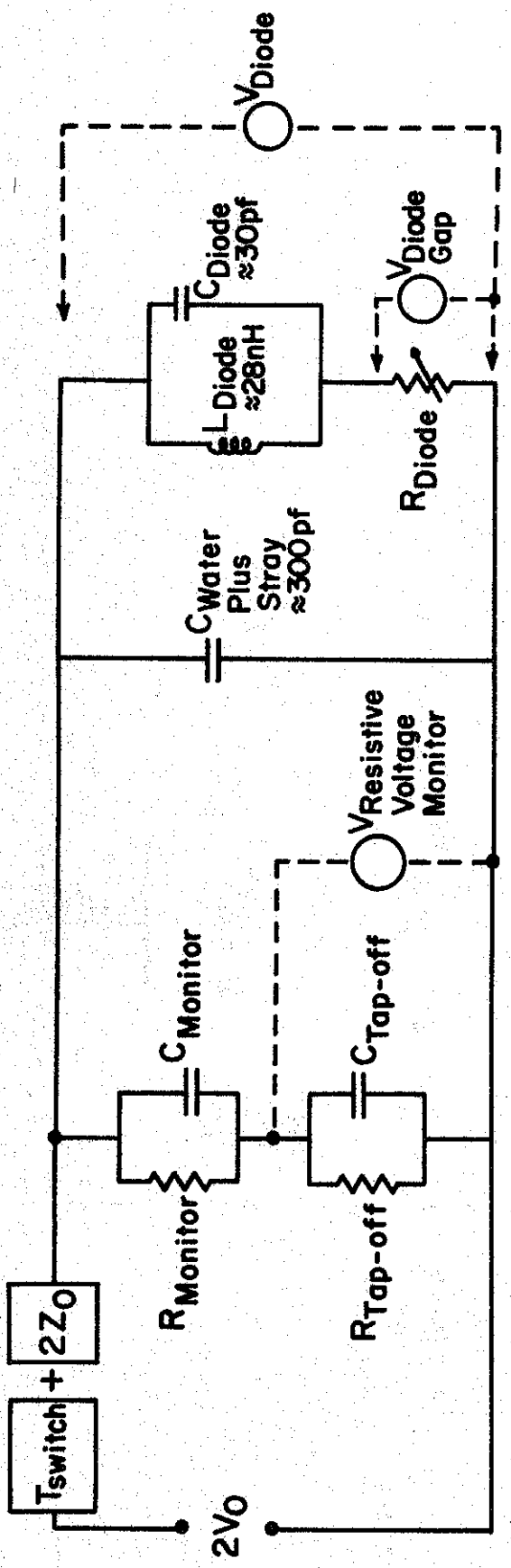

Fig. 20. Equivalent Circuit for Estimating Diode Voltage Rise Times

$$(1)\quad 2Z_0\, C_{WATER} = 4\ \Omega\ (300\ \text{pf.}) = 1.2\ \text{nsec} \tag{42}$$

where C_{WATER} can only be roughly estimated and is strongly dependent on the amount and shape of the water paths shunting the diode.

$$(2)\quad \frac{L_{DIODE}}{2Z_o + R_D} = \frac{28\ \text{nH}}{8\ \Omega} = 3.5\ \text{nsec} \quad . \tag{43}$$

$$(3)\quad R_{DIODE}\, C_{DIODE} = 4\ \Omega\ (30\ \text{pf}) \cong .1\ \text{nsec} \quad . \tag{44}$$

$$(4)\quad T_{SWITCH\ (ESTIMATED)} \cong 3\ \text{nsec.} \tag{45}$$

Since $\frac{L_D}{2Z_o + R_D} \gg R_D C_D$ we henceforth ignore $R_D C_D$. For normal shots the diode voltage should rise in a time,

$$T_{rise,normal} \cong \left[(T_{SWITCH})^2 + \left(T_{\frac{L_{DIODE}}{2Z_o + R_D}} \right)^2 \right]^{1/2} \tag{46}$$

$$= \left(3^2 + \left(\frac{28}{8}\right)^2\right)^{1/2} = 4.72\ \text{nsec} \quad . \tag{47}$$

For an open circuit test shot (i.e. $L_D = 0$)

$$T_{rise\ OPEN\ CIRCUIT} \cong \left[(T_{SWITCH})^2 + (T_{2Z_o C_{WATER}})^2 \right]^{1/2} = (3^2 + 1.2^2)^{1/2}$$

$$= 3.22\ \text{nsec} \tag{48}$$

For a Short Circuit-test shot, (i.e. $R_D = 0$)

$$T_{rise\ SHORT\ CIRCUIT} \cong \left[(T_{SWITCH})^2 + \left(\frac{T_{L_D}}{2Z_o}\right)^2 \right]^{1/2} = \left(3^2 + \left(\frac{28}{4}\right)^2\right)^{1/2}$$

$$= 7.85\ \text{nsec} \tag{49}$$

$$\frac{T_{rise\ -\ normal}}{T_{rise\ -\ open\ circuit}} = \frac{4.72\ nsec}{3.22\ nsec} = 1.47 \qquad (50)$$

This ratio has not been experimentally observed because diode voltage (V_D) is usually measured on a Tektronix 556 oscilloscope of minimum 5 nsec rise time and we have therefore been oscilloscope limited. Open circuit test shots may be used to cross check the Marx and diode voltage monitors in the same manner as the short circuit case discussed earlier. For example:

$$V_{\substack{DIODE \\ OPEN-CIRCUIT}} = 2\ V_{MARX}\ \frac{Z_D}{2Z_o + Z_D} \qquad (51)$$

or as $Z_D \longrightarrow \infty$

$$V_{\substack{DIODE \\ OPEN-CIRCUIT}} \longrightarrow 2\ V_{MARX} \qquad (52)$$

From the waveforms of open circuit shot No. 1 of 5/8/68, V_{DIODE} was measured as 390 KV and $2\ V_{MARX}$ as 386 KV .

The observed peak value of diode current is limited by the diode inductance (L_D), as follows: For the <u>diode alone</u> we have:

$$Z_D = R_D + s\ L_D \qquad (53)$$

$$V(s) = \frac{2V_0}{S} \qquad (54)$$

$$I(s) = \frac{V(s)}{Z(s)} = \frac{2V_0}{L_D}\ \frac{1}{S(S + \frac{R_D}{L_D})} \qquad (55)$$

$$i(t) = L^{-1}\left[I(s)\right] = \frac{2V_0}{R_D}\ (1 - e^{-R_D/L_D\ t}) \qquad (56)$$

$$I(t) = \frac{2V_0}{R_D}\,(1-e^{-\alpha t}) \quad ; \quad \alpha_D = \frac{R_D}{L_D} \tag{57}$$

The total circuit $\alpha(\alpha_{TOTAL})$ is equal to $\frac{2Z_o + R_D}{L_D}$ as seen in Figure 7. For $L_{D_{GEOMETRY}} = 28$ n and $2Z_o = R_D = 4\ \Omega$, α_{TOTAL} should equal 1/3.5. For a transmission line pulse of 50 nsec the exponential term in equation 57 should be negligible and the observed diode current rise times should be the same as diode voltage rise times. We do not observe this in practice. Current rise times are approximately 4 times as long as voltage rise times (28 nsec and 7 nsec respectively). One would expect that initially the diode impedance might be very high - but this makes the expected current rise time shorter not longer. A second possibility is that the initial diode current occurs over a radius, (a), much less then that of the geometrical cathode radius and that initially the diode inductance ($L_D = 2\,\ell \log_e \frac{b}{a}\, 10^{-9}$ henrys) is greater than predicted by geometry, but again the logarithmic term means that the variation is slow and this answer is not totally satisfactory either.

D. DIODE IMPEDANCE

1. A Comparison with the Child-Langmuir Equation

Typical diode-voltage (V_D) and diode-current traces are shown in Figure 21. Since the voltage waveform does not collapse or droop appreciably nor the current waveform increase discontinuously* during the Blumlein pulse (50-60 nsec) for pressure variations of $2\frac{1}{2}$ orders of magnitude, some form of space-charge-limited current emission is

*Recall that the source impedance is $2Z_o$ and equal to either 3.5 or 4 ohms.

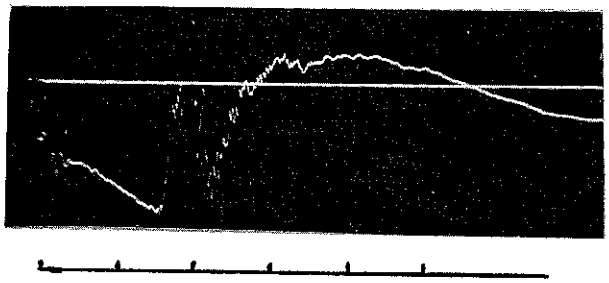

.5 microseconds/div

Marx Generator Voltage - Transmission line switch fires at sharp discontinuity.

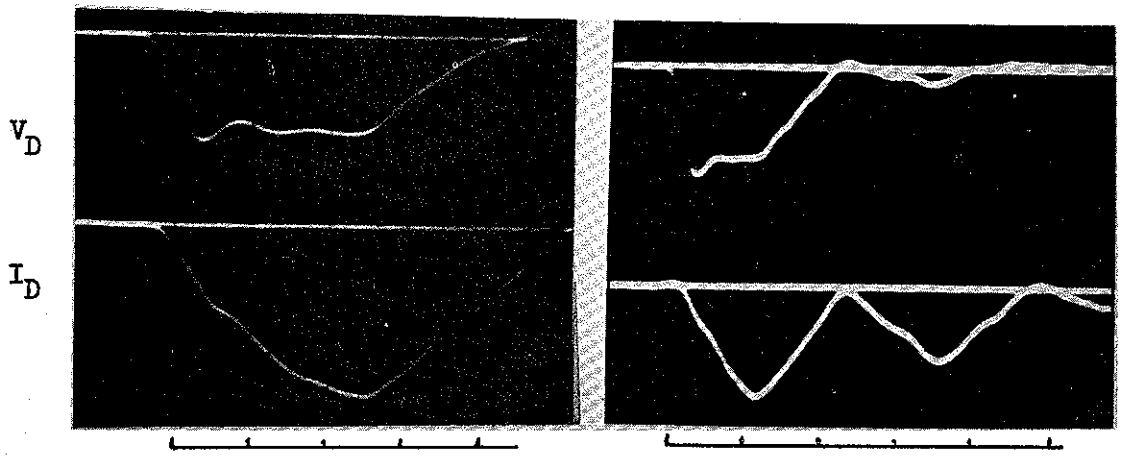

20 nanoseconds/div

V_D = 358 KV
I_{peak} = 76 KA
Z_D = 4.7 ohms
Shot # 5, 5/1/69

50 nanoseconds/div

V_D = 337 KV
I_{peak} ± 50 KA
Z_D = 6.74 ohms
Shot # 11, 5/14/69

Figure 21 TYPICAL DIODE MONITOR WAVEFORMS

at once postulated, and a comparison with the classical predictions of the Child-Langmuir equation[7] seems reasonable.

$$I_{C-L} = 2.34 \times 10^{-6} V_D^{3/2} \frac{A}{d^2} \left(\frac{AMP}{M^2}\right) \qquad (58)$$

For a flat voltage pulse:

$$Z_{C-L} = \frac{4.27 \times 10^5}{V_D^{1/2}} \frac{d^2}{\pi r^2} = \frac{136}{V^{1/2}} \left(\frac{d}{r}\right)^2 \text{ ohms} \qquad (59)$$

V is in megavolts

d = gap, in cm

r = cathode radius in cm .

The Cornell diode impedance (Z_D), measured during the flat resistive phase of the voltage and current waveforms is seen in Figure 22 to be less than that predicted by Child-Langmuir by a factor of approximately 2 over a broad range of anode-cathode gap spacings, (d), and for diode pressures ranging from 5×10^{-2} torr to 10^{-5} torr. (Exceptions to this rule, i.e. data for which Z_D is $\geq Z_{C-L}$ such as points 54-58 of Figure 22, will be accounted for in Chapter IV, Section D.) Table I compares the Cornell results with those of similar facilities. From the table it can be seen that all but the NRL facility observe diode impedances within a factor of two of Z_{C-L}. Measured impedances at NRL are smaller than Z_{C-L} by a factor of 15-20 and this special case is discussed in more detail in Section 3 of this chapter.

Since the Cornell diode is normally operated at a pressure of 2×10^{-4} torr some of the additional diode current is believed to be caused by beam-generated ions in the gap region, in the following manner.

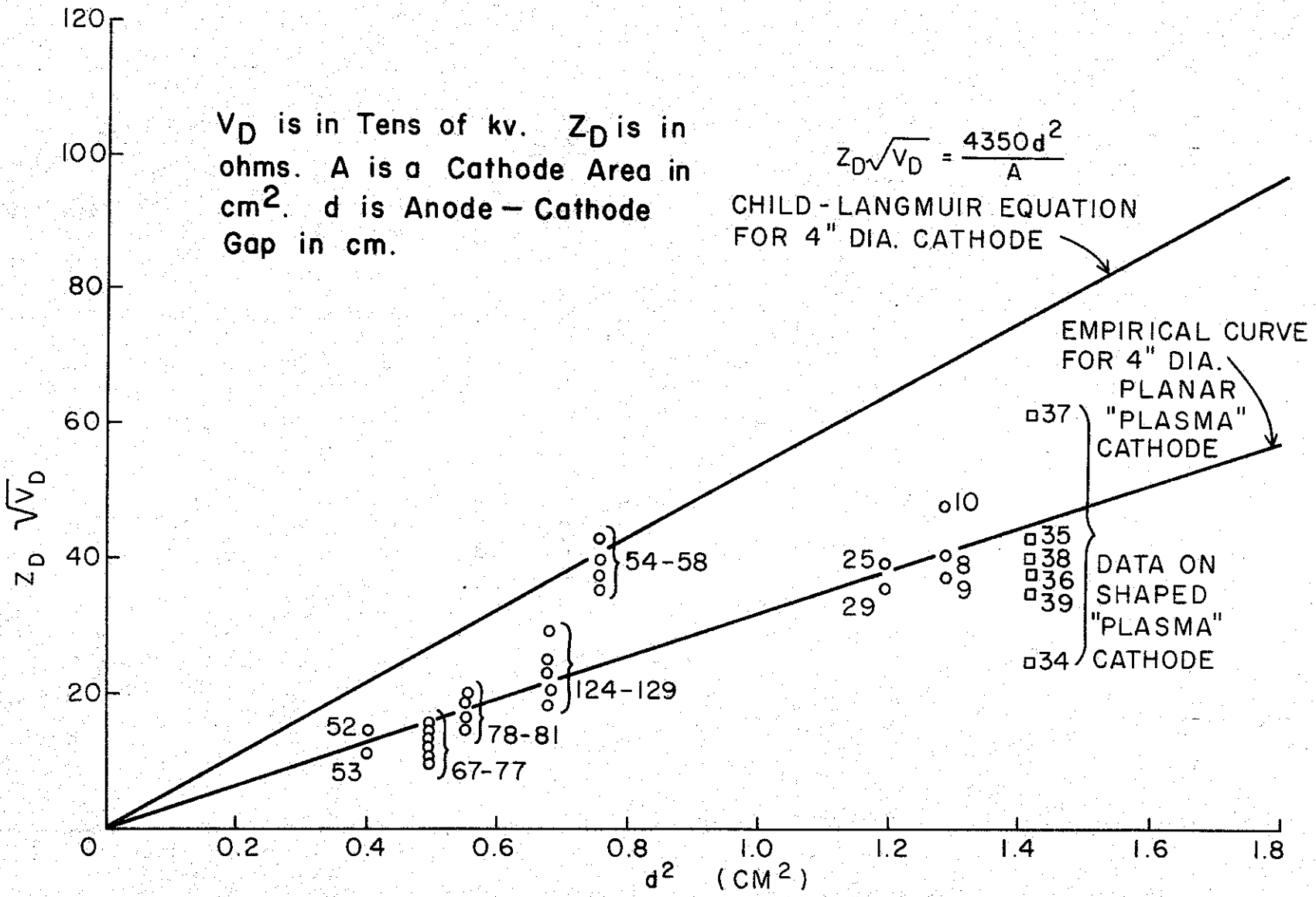

Fig. 22. Comparison of Child-Langmuir Equation and Cornell Diode Data for 4.0" Planar "Plasma" Cathode.

FACILITY	Z_D (MEASURED)	SPECIFICS
Physics International San Leandro, Calif.	$\frac{80}{V^{1/2}} \frac{d^2}{r^2}$	True from 200 KV to 5 MV needle cathode, r = 35 mm d = 2-10 mm
EG and G Brookline, Mass.	Z_{C-L}	V_D= 80-300 KV, I_D= 10-80 Ka $A_{CATHODE}$= 2cm, Z_D= 30 nsec
AWRE Aldermaston, England	Z_{C-L}	V_D= 200-500 KV, I_D= 50-100 Ka
Cornell	$\frac{80}{V^{1/2}} \frac{d^2}{r^2}$	V_D= 200-500 KV, I_D= 50-125 Ka $A_{CATHODE}$=80cm, d=10mm, T = 50 nsec.
Naval Research Lab. (NRL) Washington, D.C.	$\frac{136}{V^{1/2}} (\frac{\lambda_D}{r})^2$	I_D=200-500 Ka, V_D= 750 KV r_c= 2.5 cm, d = 7 mm λ_D=Debye length = $740(W_e/n_e)^{1/2}$

Table I

The number of beam electrons / cc (neglecting scattering of the primary beam) is given by[8]

$$n_e \cong 1.05 \times 10^{11} \frac{I}{AV^{1/2}} \qquad (60)$$

where I is in amps

V is in volts

A is the beam cross section in cm^2 .

For $I = 10^5$, $A = 80\ cm^2$, $V = 5 \times 10^5$

$$n_e \approx 2 \times 10^{11} \text{ electrons/cc}$$

The number of beam-generated ions formed per second per cm of length

is given empirically by[9,10]

$$N_i \approx \frac{3.75 \times 10^{23}\, Ip}{V} \tag{61}$$

where I is the primary beam current in amps

V is the voltage through which the electrons have been accelerated, in volts

p is the gas pressure, in torr.

Since the gap (d) in the Cornell diode is approximately 1 cm, we have for $I = 10^5$ amp, $V = 4 \times 10^5$ volts, $p = 2 \times 10^{-4}$ torr:

$$N_i = \frac{3.75 \times 10^{23}(10^5)(50 \times 10^{-9}\,\text{sec})(2 \times 10^{-4}\,\text{torr})}{4 \times 10^5} \tag{62}$$

$$n_i = \frac{9.38 \times 10^{11}}{80\ \text{cc}} = 1.17 \times 10^{10}/\text{cc} \tag{63}$$

The hard-vacuum Child-Langmuir equation may be modified (during the d-c portion of the waveforms) to include the presence of ions in the gap as follows:[11]

$$\nabla^2 V = -\frac{1}{\epsilon_o}(-n_e e + n_i e) \tag{64}$$

$$\bar{J} = -n_e e v_e + n_i e v_i \approx -n_e e v_e \quad (\text{for } v_e \gg v_i) \tag{65}$$

$$\frac{1}{2} m_e v_e^2 = eV \ (\text{since } V_{\text{accel.}} \gg V_{\text{ionization}}) \tag{66}$$

$$J = -n_e e \left(\frac{2eV}{m_e}\right)^{1/2} \tag{67}$$

$$\frac{d^2V}{dx^2} = \frac{1}{\epsilon_o}\left[J\left(\frac{m_e}{2eV}\right)^{1/2} + n_i e\right] \tag{68}$$

$$2\left(\frac{dV}{dx}\right) dx \frac{d^2V}{dx^2} = \frac{J}{\epsilon_o}\left(\frac{m}{2e}\right)^{1/2} V^{-1/2} 2dV + \frac{1}{\epsilon_o} n_i e\, 2dV \tag{69}$$

Integrating, we have:

$$\left(\frac{dV}{dx}\right)^2 = 4\,\frac{J}{\epsilon_o}\left(\frac{m_e}{2e}\right)^{1/2} V^{1/2} + \frac{2}{\epsilon_o}\, n_i eV \qquad (70)$$

From (67) we have

$$V^{1/2} = \frac{-J}{n_e e}\left(\frac{m}{2e}\right)^{1/2} \qquad (71)$$

Equation (70) becomes

$$\left(\frac{dV}{dx}\right)^2 = 4\,\frac{J}{\epsilon_o}\left(\frac{m}{2e}\right)^{1/2} V^{1/2} + \frac{2}{\epsilon_o}\, n_i \not{e}\, V^{1/2}\left(\frac{-J}{n_e \not{e}}\right)\left(\frac{m}{2e}\right)^{1/2} \qquad (72)$$

$$\left(\frac{dV}{dx}\right)^2 = 2\,\frac{J}{\epsilon_o}\left(\frac{m}{2e}\right)^{1/2}\left(2 - \frac{n_i}{n_e}\right) V^{1/2} \qquad (73)$$

$$\frac{dV}{dx} = \sqrt{2}\left(2 - \frac{n_i}{n_e}\right)^{1/2}\left(\frac{J}{\epsilon_o}\right)^{1/2}\left(\frac{mV}{2e}\right)^{1/4} \qquad (74)$$

For $n_i = 0$ (i.e. Child-Langmuir) For $n_i \approx n_e$

$$\frac{dV}{dx} = 2\left(\frac{J}{\epsilon_o}\right)^{1/2}\left(\frac{mV}{2e}\right)^{1/4} \qquad \frac{dV}{dx} = \sqrt{2}\left(\frac{J}{\epsilon_o}\right)^{1/2}\left(\frac{mV}{2e}\right)^{1/4} \qquad (75)$$

Integrating again

$$\frac{4}{3} V^{3/4} = 2\left(\frac{J}{\epsilon_o}\right)^{1/2}\left(\frac{m}{2e}\right)^{1/4} x \qquad \frac{4}{3} V^{3/4} = \sqrt{2}\left(\frac{J}{\epsilon_o}\right)^{1/2}\left(\frac{m}{2e}\right)^{1/4} \qquad (76)$$

Solving for J yields

$$J = \frac{4\epsilon_o}{9}\left(\frac{2e}{m}\right)^{1/2}\frac{V^{3/2}}{x^2} \qquad J = \frac{4\epsilon_o}{9}\, 2\left(\frac{2e}{m}\right)^{1/2}\frac{V^{3/2}}{x^2} \qquad (77)$$

Since

$$Z_D^{-1} = \frac{J \cdot A}{V} \qquad (78)$$

$$Z_{C-L} = \frac{9}{4\epsilon_o}\left(\frac{m}{2e}\right)^{1/2}\frac{x^2}{AV^{1/2}} \; ; \; Z_{D_{ions}} = \frac{9}{4\sqrt{2}\,\epsilon_o}\left(\frac{m}{2e}\right)^{1/2}\frac{x^2}{AV^{1/2}} \tag{79}$$

$$Z_{C-L} = 136\ V^{-1/2}\frac{x^2}{r^2} \qquad Z_{D_{ions}} = 96\ V^{-1/2}\frac{x^2}{r^2} \tag{80}$$

$Z_{D_{ions}}$ of equation (80) which has assumed $n_e \approx n_i$ compares favorably with both the Cornell and Physics International Co. data of Table 1. Considering only beam-generated ions in the gap we have estimated:

$$\frac{1}{f} = \frac{n_e}{n_i} = \frac{2 \times 10^{11}/cc}{1{,}17 \times 10^{10}/cc} \cong \frac{17.0}{1} \tag{81}$$

Equation (81) indicates that beam-generated ions alone will produce fractional ionizations , $(f = \frac{n_i}{n_e})$, of less than 6% . It should be noted however that estimates of N_i and n_i (from equations (62) and (63) respectively) are quite conservative in that the assumption is implicit that all the electrons in the gap have acquired energies of 4×10^5 eV before undergoing collisions. Many of the beam electrons will of course suffer collisions while still in the process of acquiring this energy (i.e. while the probability of an ionizing collision is considerably higher than for an electron of 4×10^5 eV), resulting in a fractional ionization considerably larger than 6% . Additionally, if other sources of ion creation in the gap region are considered such as ion-atom collisions, anode bombardment, and cathode sputtering, fractional ionizations of approximately 1 become very reasonable.

2. Relativistic Corrections of the Child-Langmuir Law

The beam-generated-ion correction to the hard-vacuum Child's Law discussed above is exact for low accelerating voltages but requires correction as the applied voltage is raised. Harmon[8] gives an approximate solution to the relativistic Child-Langmuir Law as:

$$I \propto V_o^{3/2} \left(1 - \frac{3}{28} \frac{V_o}{V_N}\right) \qquad (82)$$

where

$$V_N = \frac{m_o c^2}{e} = 5.11 \times 10^5 \text{ volts}$$

and remarks that the reduction in current is due to the fact that "for any given voltage the electron velocity is less than that calculated from non-relativistic considerations. The charge density is therefore greater and the field in the region of the cathode correspondingly reduced."

A more detailed analysis over large voltage ranges, and asymptotic solutions have been carried out by Acton.[12] More recently, Boers and Kelleher[13] have presented an exact solution of Poisson's equation for the one-dimensional case. Figure 23 compares their exact solution (a combination of 2 convergent series) with 1) Childs Law (which is a good low voltage approximation) and with, secondly, an ultra-relativistic solution which is an approximate high voltage solution and which gives 1% accuracy only for U values ≥ 200 . The figure shows that for the usual Cornell operating voltages of U ranging from 0.5 to 1.0, the Child's Law correction is $\leq$ 10% and we therefore choose to neglect relativistic corrections in our analyses because the aforementioned space-charge neutralization caused by beam-generated and other ions are a much more important correction consideration.

3. Transmission Line Imbalance - The Condition Called "Pre-Pulse"

Should an imbalance of more than a few percent between the charging impedances of the two sides of the Blumlein occur, a "pre-pulse" voltage of up to many tens of kilovolts may exist across the diode gap during the Marx-to-Blumlein energy-transfer cycle, prior to the firing of the solid dielectric switch. Since this charging cycle lasts on the

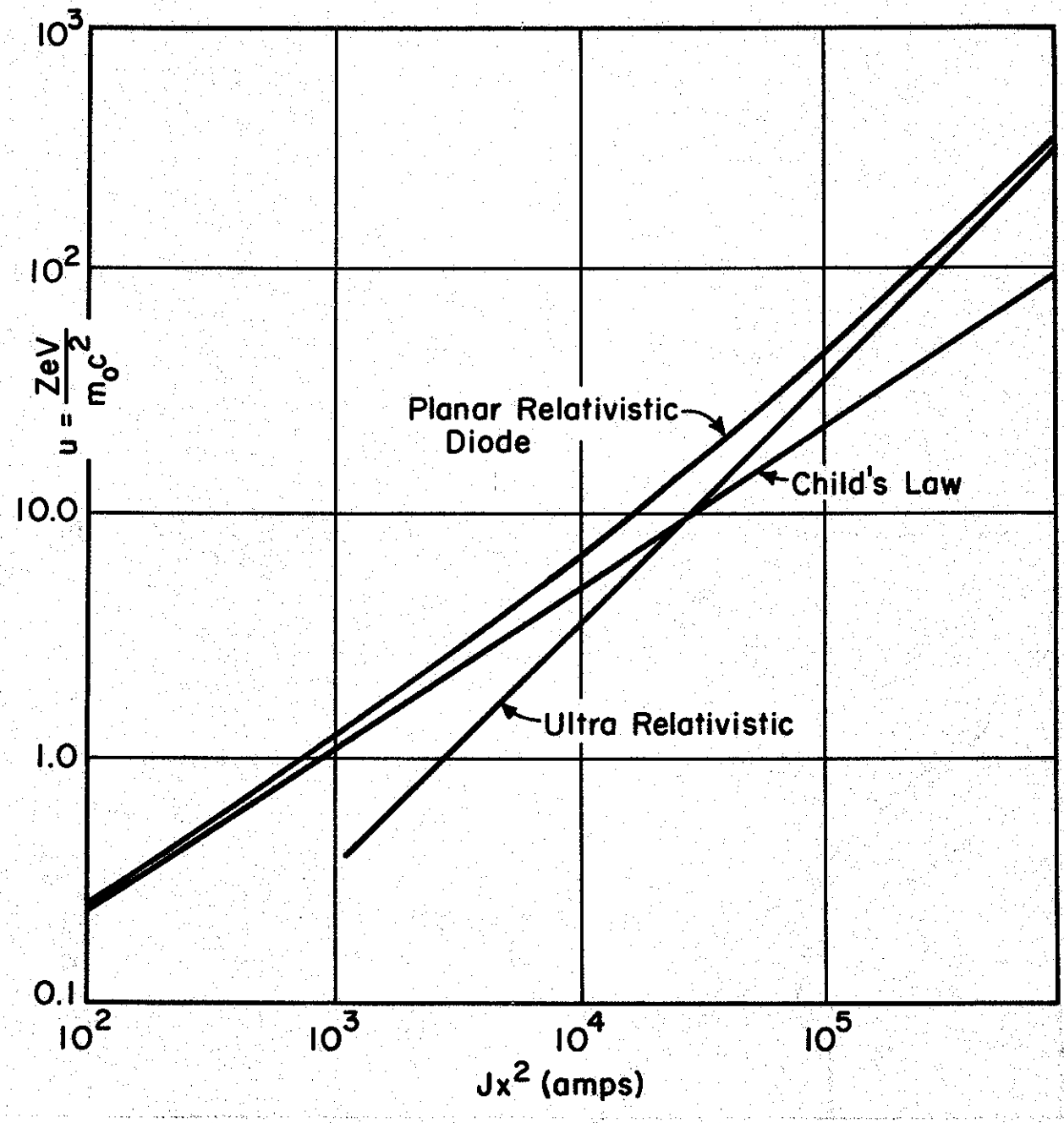

Fig. 23. Comparison of Planar Relativistic Diode, Child's Law, and Ultrarelativistic Soultions (After Reference 13)

order of a microsecond, the diode gap has sufficient time to become plasma filled* and upon arrival of the main pulse (V_D) the diode impedance will collapse.

The Cornell Blumlein has been measured to be balanced within 1.5% but the results of gross line imbalance (caused by a partial failure of one of the 2μh charging inductors) may be seen in Figure 24 to cause main-pulse collapse very similar to that of short circuit test shots, and this is considered to be evidence that such a "pre-pulse" plasma did in fact exist in the gap region. It is further believed that a measured line imbalance of approximately 10% and charging voltages in the megavolt range explains in part, at least, the difference between the measured impedance of the NRL facility and the other listed results in Table I.

*The measurements of formative plasma times in the anode-cathode gap discussed in Chapter III are not directly applicable since they were post-main-pulse plasma formation times. The rapid formation times (a few tens of nsecs) do indicate, however, that above a certail threshold field strength in the gap (% of imbalance) there is certainly enough time (~ nsec) for the plasma to form.

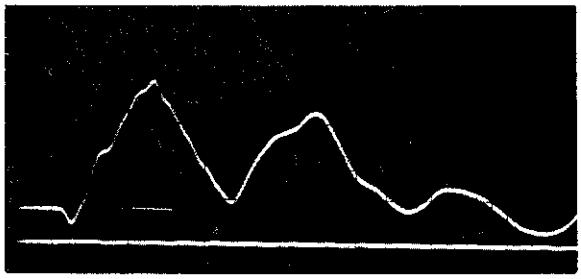

a. Diode Current Waveform - Normal Operating Conditions
Shot #2 3/19/69

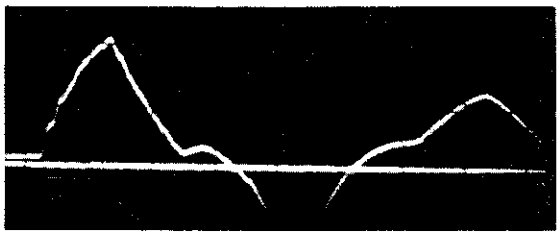

b. Diode Short Circuit Current Waveform
Shot #4 3/21/69

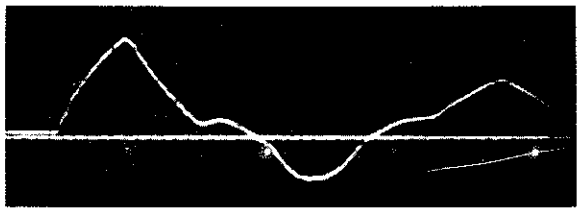

c. Diode Current Waveform for case of Gross Imbalance in Charging Impedance (Pre-Pulse Condition)
Shot #4 3/23/69

Fig. 24. $\dot{B}$ Probe Measurements of Diode Current
All Traces $\frac{50 \text{ nsec}}{\text{cm}}$, $\frac{28 \text{ KA}}{\text{cm}}$.

CHAPTER III - CATHODE STUDIES

Measurements of the diode impedance (Chapter II) have shown that it is less than that predicted by the Child-Langmuir equation by a factor of approximately two over a broad range of anode-cathode gap spacings, d, and for diode pressures ranging from 5×10^{-2} to 10^{-5} torr. For diode voltages of a few hundred kilovolts, diode currents of several tens of kiloamps are obtained. In this chapter an attempt will be made to explain:

1) the mechanism/s by which such large currents are possible, and
2) the effects of the dielectric cathode sections on the observed spatial distribution of the diode current.

A. EMISSION MECHANISMS FOR METAL CATHODES

A number of possible emission mechanisms have been considered in an attempt to explain the current densities in diodes of the Cornell type. Among these were:[14]

a) High-Field Emission
b) Electron Emission from Ionization and Ion Bombardment
c) Thermionic Emission due to Ohmic Skin Heating
d) Secondary-Electron Emission due to Electron Bombardment.

There is now general agreement among investigators[1,4,14,15] that high field emission (Fowler-Nordheim tunneling[16]) or T-F emission* are the

*"Emission from a heated conductor subjected to a field of sufficient magnitude so that most electrons are emitted through rather than above the surface energy barrier of the metal"

dominant mechanisms in liberating the initial electrons from the cathode surface. T-F emission is of particular interest because it does not require the ultra high vacuum (10^{-12} to 10^{-9} torr) of pure cold field emission surfaces[17] and is more compatible to our own operating pressure range (10^{-4} torr). Pure field emission is governed by the modified Fowler-Nordheim equation[18]

$$J = (1.54 \times 10^{-6} \frac{F^2}{\phi}) \exp\left[-6.83 \times 10^{7} \phi^{3/2} \frac{f(y)}{F}\right] \qquad (83)$$

where

J = current density (amp/cm^2)

F = electric field (V/cm)

ϕ = emitter work function (eV)

$f(y)$ = a slowly varying function (Nordheim elliptic function) which, over the useful range of the equation is almost constant and typically varies between 0.7 and 0.95.

Figure 25, taken from reference 18, shows the strong dependence of J on both F and ϕ.

T-F emission is an intermediate process between the extremes of thermionic emission and field emission. Figures 26a and 26b (from Reference 15) "show the theoretical dependence of emitted current density on field and temperature for tungsten (ϕ = 4.5 eV). Figure 26a shows that in regions to the left of point A [thermionic and Schottky (field-assisted thermionic) range] tunneling accounts for a very small percentage of the total emission; J is sensitive to T, but relatively insensitive to F. In the region to the right of points B(T-F and field emission range) emission occurs primarily or solely by tunneling; J increases rapidly with F, becoming very large and relatively insensitive to T.

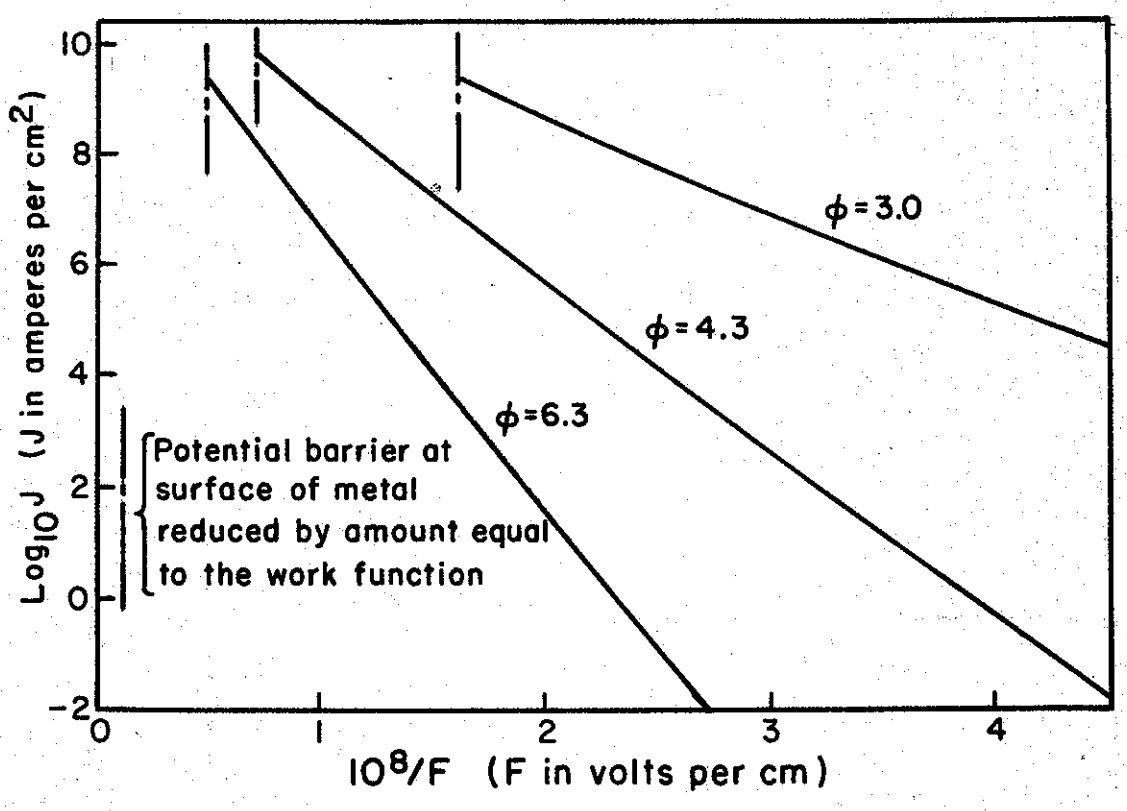

Fig. 25. Graphs of the Modified Fowler-Nordheim Relation of Eq.(5), Showing Field-Current Density J as a Function of Applied Surface Electric Field F, For Several Values of the Work Function ϕ in ev. (After Reference 18).

Eq.(5) of Reference 18. $$J = (1.54\times10^{-6}\frac{F^2}{\phi})e^{-6.83\times10^7\phi^{3/2}\frac{f(y)}{F}}$$

J in amp/cm^2
F in V/cm
ϕ in eV

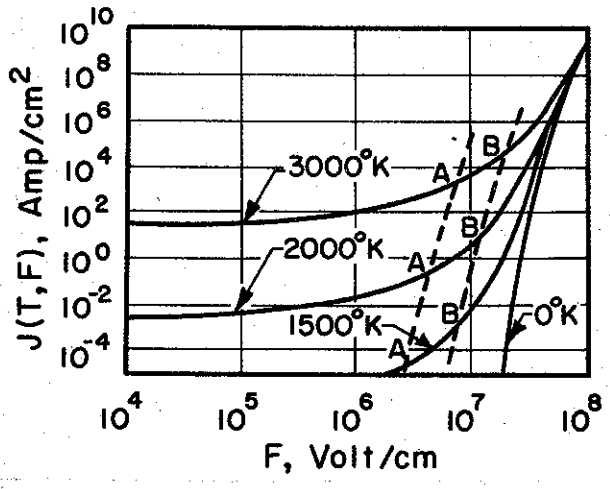

Fig. 26a. Theoretical Dependence of Emitted Current Density on Field and Temperatures. (After Reference 17)

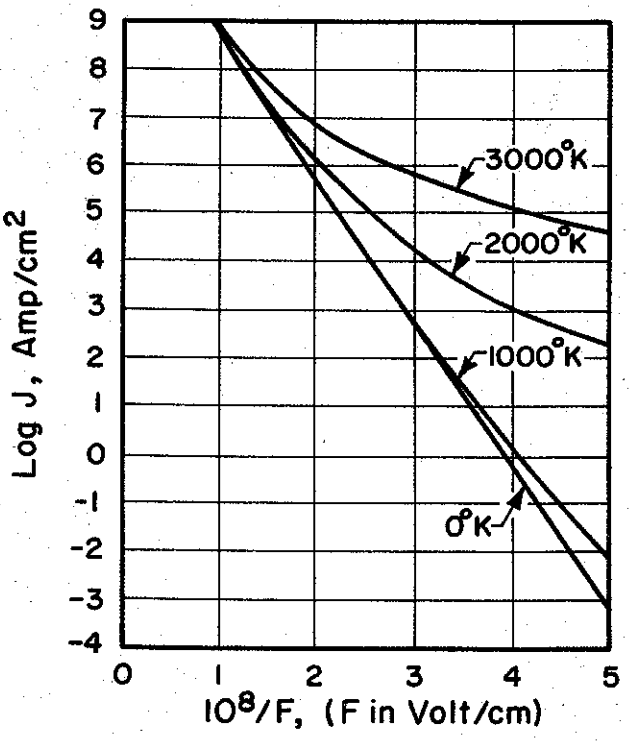

Fig. 26b. Computed Current Density Versus Reciprocal Field at Various Temperatures. (After Reference 17)

Figure 26b displays the above information in the high field region (2×10^7 to 10^8 volts/cm). In theory, emission densities above 10^{10} amps/cm^2 could be reached; in practice, however, J is limited by resistive heating of the cathode and power dissipation requirements."[15]

B. METAL-DIELECTRIC CATHODE STUDIES - AN AD HOC APPROACH

Accurate studies of field-emitted current even from point sources, are very difficult because of:[19]

a) Differences in the emission from different crystal faces of a single crystal point.

b) Non-uniformities in the field distribution produced by microscopic irregularities in the point.

c) The extreme difficulty in maintaining a clean point of a pure metal at low temperatures, even in the best available vacuua.

A consideration of these difficulties, complicated by the additional operational requirements of the Cornell diode such as:

a) A large-area (~80 cm^2) cathode [to provide large currents at low voltage and gaps of the order of 1 cm. Recall:

$$Z_D \cong \frac{80}{(V_D)^{1/2}} \left(\frac{d}{r}\right)^2]$$

b) A cathode composed of metal and plastic (and therefore having no distinct work function)

c) Operation in a soft vacuum (~10^{-4} torr) environment.

has led to a more ad hoc approach in cathode studies. For example, the Cornell diode has average fields of approximately 5×10^5 V/cm (400 KV across 8 mm gap). From Figure 26a, even for cathode temperatures of

2000° K, total cathode currents of only a 100 amp could be expected. However, the field enhancement at the hole edges and at other microscopic irregularities or "whiskers" (caused by local field stresses) on the cathode surface can enhance the average field by several orders of magnitude. "Whiskers" have been observed[20,21] under electron microscopes to be typically 10^{-5} cm. in diameter and 10^{-4} cm in length, and to enhance the local field by approximately 100 .

For the present, let us assume that the total currents measured (up to 10^5 amp) require current densities ($\frac{10^5}{80\ cm^2}$) large enough to destroy surface whiskers and that after a few nanoseconds, a dense plasma cloud, a virtual cathode, composed of vaporized whiskers and possibly dielectric fill material is the source of the space-charge-limited electron flow observed in Chapter II. (This model will be supported by experiments reported on in sections to follow.)

1. Radiograph and Optical Studies of Various Cathode Geometries

Figure 27 shows the experimental setup for obtaining both pinhole radiographs and optical photographs of the various cathodes, The lens used throughout these experiments is a multi-faceted lens (known as a PRISMA lens) and is similar to those used in television for multiple-image displays. Each of its off-center facets was covered with a different value of neutral-density Wratten filter giving light attenuations of 0,2,4,10 and 20 times, and thus allowed a comparison of the visible light generated in the diode with the radiograph which was being simultaneously taken.

X-ray pinhole-camera radiographs* (magnifications ranging from (1/4 to 1) were made of the "plasma" cathode for a variety of input voltages,

*Ilford Red-Seal X-ray film ($\gamma \approx 3$) was used. To maintain a constant film γ, the development and fixing times were controlled. The pinhole X-ray camera is homemade, and consists of 1/8" lead sheets folded into a box design with a 1 mm pinhole in the front, center.

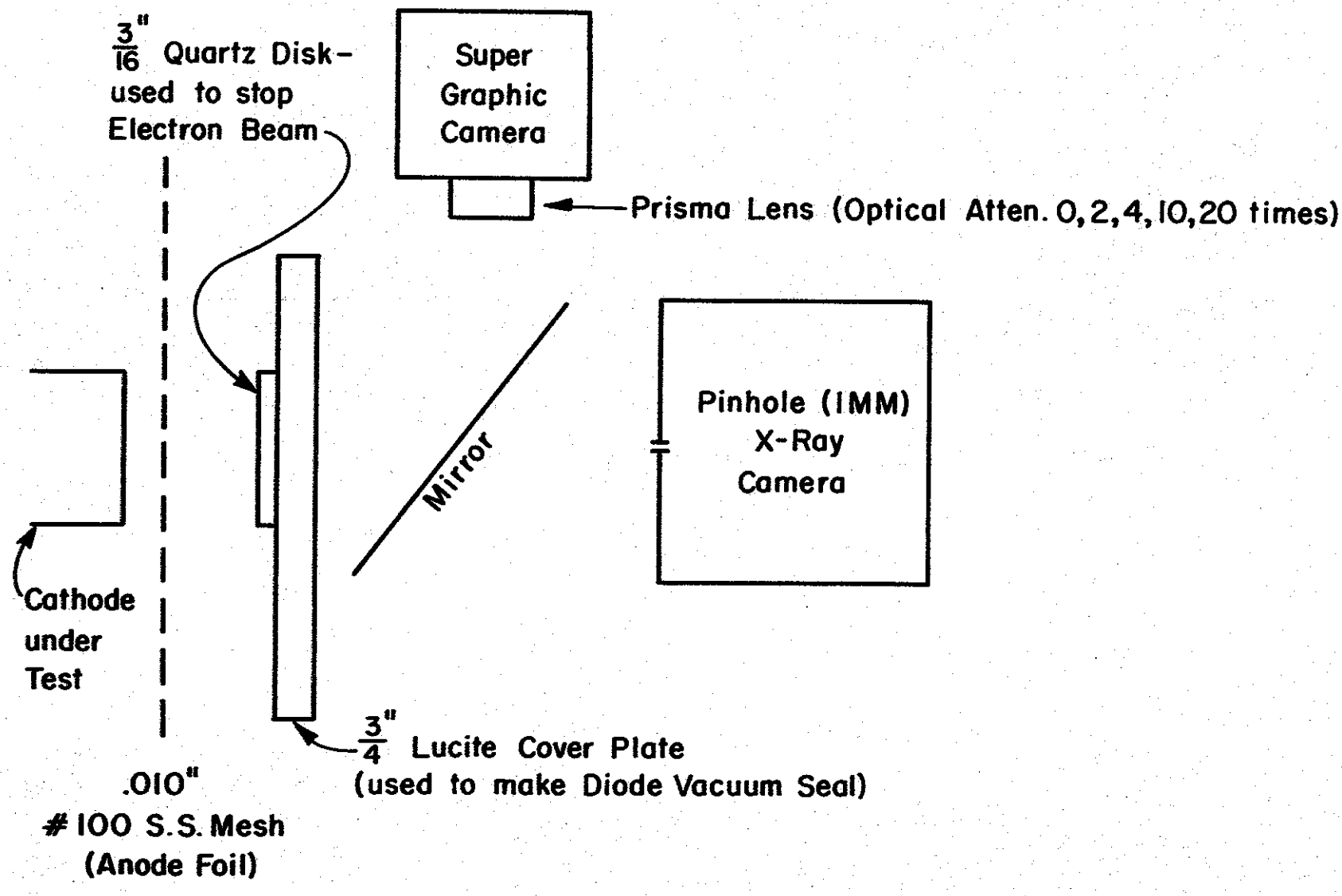

Fig. 27. Experimental Setup for Measuring Time Integrated Electron Spatial Distribution of Various Test Cathodes.

pressures and anode-cathode gaps. Most radiographs of the "plasma" cathode showed a "honeycomb" type emission pattern, whose resolution indicated reasonably laminar flow, as was predicted by J.C. Martin of AWRE, who originally suggested the "plasma" cathode design.

In addition, shots were made on a "plasma" cathode whose conical holes were not filled with a dielectric. No change in diode impedance (Z_D) was observed for this unfilled case, but a distinctly different, less regular emission pattern resulted. The contrast in the two types of emission patterns is perhaps best illustrated by a radiograph of a cathode in which the holes of the bottom half were filled with lucite and in which the holes of the top half were left unfilled (See Figure 28). Z_D, measured for this half-filled, half-unfilled case was approximately the same as for the completely filled case. The darkest section of the radiograph is believed to be the result of a current "pinch" in the anode-cathode gap which is dependent on diode current, voltage and aspect ratio (See Chapter IV).

Because Z_D remained invariant with the first three cathode designs used, it was decided to use cathodes of a quite different design in an effort to sort out the importance, if any, of such parameters as hole diameter, type of dielectric fill material used etc.

Figures 29-30 show the correspondence obtained for the radiographs and PRISMA lens photographs, for a) the brass plasma cathode (filled) b) the brass plasma cathode (unfilled) and c) the aluminum outer hole cathode.

Figure 31 shows some of the cathode designs on which shots were made both for the filled and unfilled configuration and Figure 32 orders the cathodes according to:

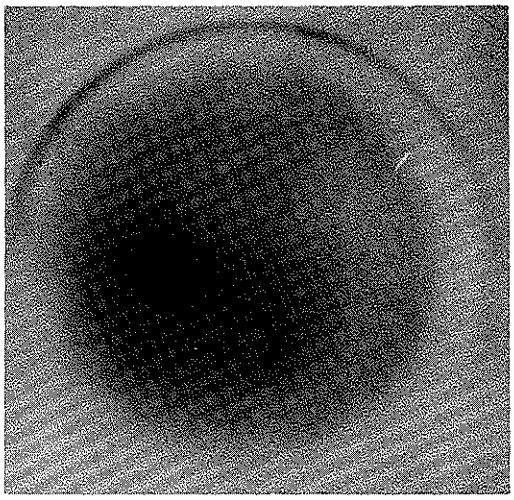

Fig. 28. Radiograph of 4.0" Plasma Cathode
Bottom Half Filled - Top Half Unfilled
Shot #14, 10/29/68
V_D = 423 KV, I_D = 64.7 KA, Z_D = 6.56Ω

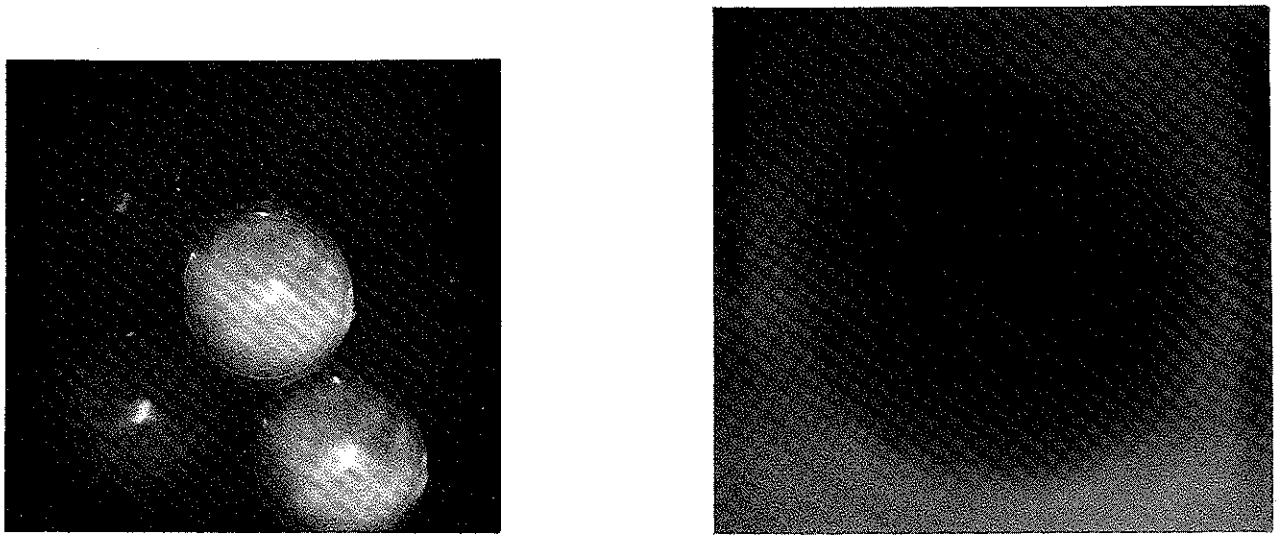

(a). 4.0" Brass Plasma Cathode (Filled)
Shot #4, 10/29/68
V_D = 373 KV, I_D = 52.7 KA, Z_D = 7.09Ω

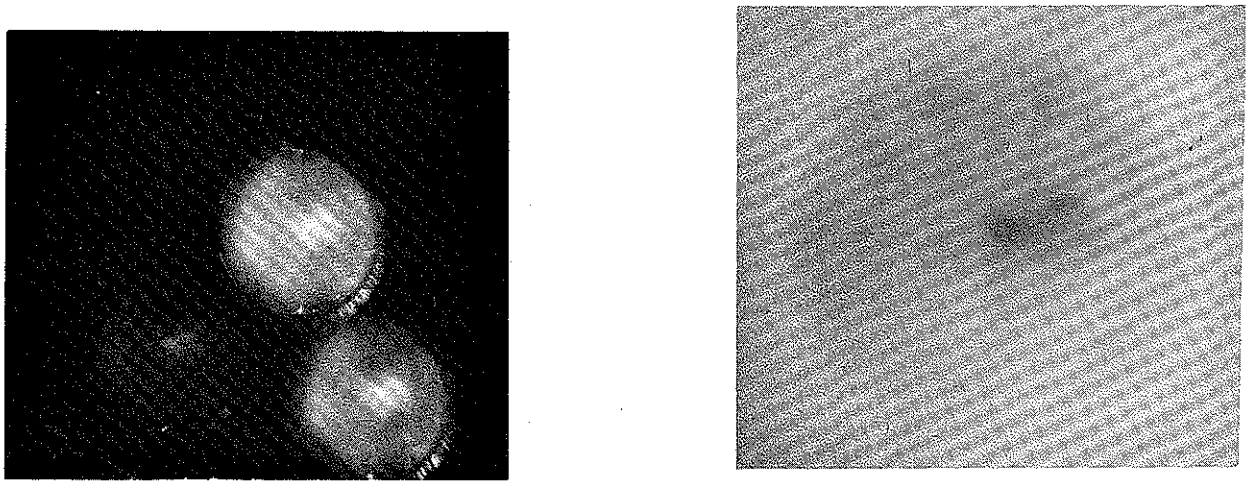

(b). 4.0" Brass Plasma Cathode (Unfilled)
Shot #10, 10/29/68
V_D = 330 KV, I_D = 45.6 KA, Z_D = 7.24Ω

Fig. 29. A Comparison of Radiographs and Prisma Lens Photographs (Optical Attenuation 0,2,4,10, 20 Times)

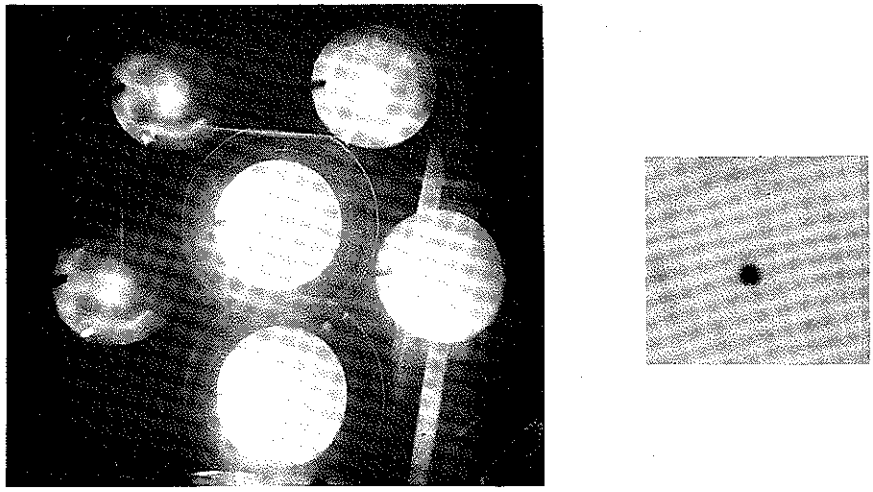

(a). 4.0" Aluminum Outer Hole Cathode
Shot #24, 7/18/68
V_D = 360 KV, I_D = 32 KA, Z_D = 11.2Ω

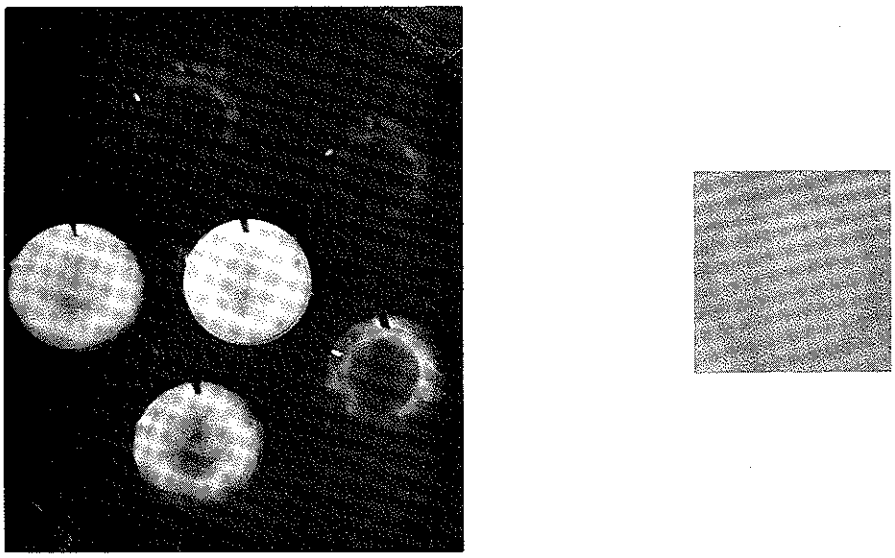

(b). 4.0" Brass Ridge Cathode
Shot #11, 7/18/68
V_D = 260 KV, I_D = 28.6 KA, Z_D = 9.1Ω

Fig. 30. A Comparison of Radiographs and Prisma Lens Photographs (Optical Attenuation 0,2,4,10, 20 Times)

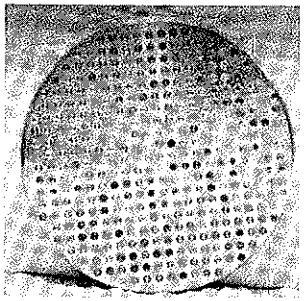

(a)
4.0" Brass Plasma, Filled (After 35 Shots)

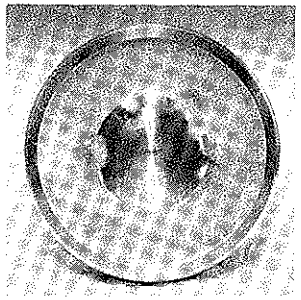

(b)
Wide Ridge, Filled (After 10 Shots)

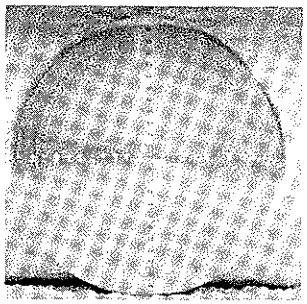

(c)
Cross, Unfilled

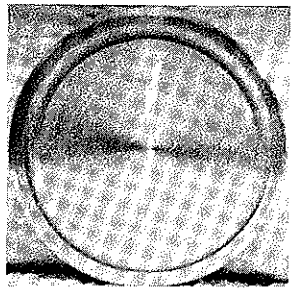

(d)
Narrow Ridge (1/4") Unfilled

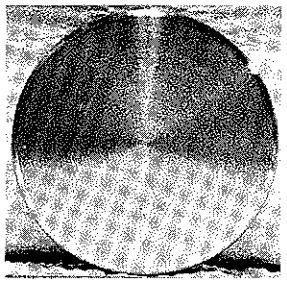

(e)
Brass, Blank

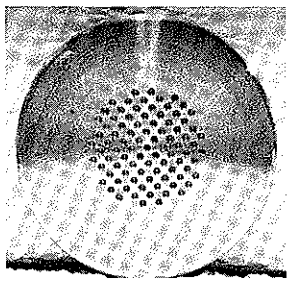

(f)
Plasma Center

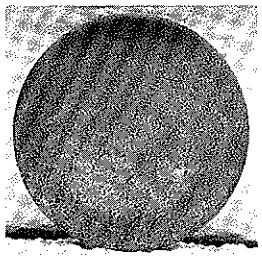

(g)
EG&G Sintered Tungsten

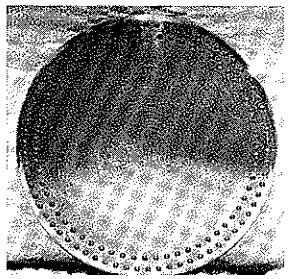

(h)
Edge Hole

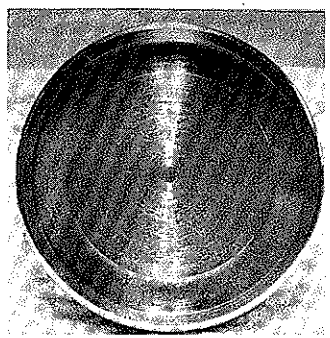

(i)
Intermediate (1/2") Ridge, Unfilled

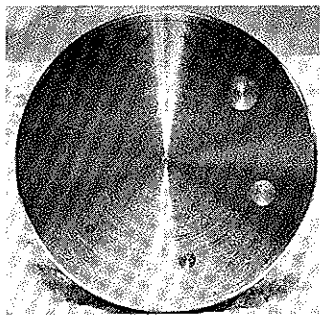

(j)
Various Hole Size, Filled

Fig. 31. Test Cathodes & Designs

FIG. 32

DIODE-IMPEDANCE ORDER
FOR
VARIOUS CATHODE SURFACES
(BASED ON CATHODE GEOMETRY)

Z_D-ORDER	CATHODE - SURFACE TYPE	
LOW-HIGH	FOR $Z_D \propto \frac{1}{A}$:	FOR $Z_D \propto \frac{1}{C}$:
1	WIDE RIDGE	PLASMA*
2	PLASMA*	EDGE HOLES
3	MEDIUM RIDGE	CENTER HOLES
4	NARROW RIDGE	NARROW RIDGE
5	EDGE HOLES	MEDIUM RIDGE
6	CENTER HOLES	WIDE RIDGE
7	CROSS	CROSS
8	NON-UNIFORM HOLES	NON-UNIFORM HOLES

*MANY PLASTIC-FILLED HOLES OVER ENTIRE SURFACE

$$Z_D \propto \frac{1}{A} \; ; \quad \text{where} \quad A = \text{total hole area}$$

$$Z_D \propto \frac{1}{C} \; ; \quad \text{where} \quad C = \text{total hole circumference.}$$

Difficulty in comparing data on the various cathode types was encountered because the diode voltage (V_D) is controlled by the breakdown voltage of the pre-stabbed solid-dielectric Blumlein switch for which the scatter was approximately $\pm$ 6% . A substantial number of shots on each cathode design was therefore required in order to allow grouping of the shots with approximately constant input voltage to the diode (i.e. rule out the input voltage as a parameter) and cause Z_D to be a function of cathode design only. Figure 33 presents early data on such an ordering scheme. While promising, it lead to no definite conclusion, since a comparison of Figure 33 with Figure 32 shows that the cathode data (i.e. Z_D) order according to either, 1/A or 1/C .

A newer switch fabrication technique reduced the Blumlein switch scatter to $\pm$ 2% and the data were more easily taken. Figure 34 indicates that the filled cathode structures order according to $Z_D \propto 1/A$.

A tabular summary of the observed spatial distribution patterns of the various cathodes tested is given in Figure 35. Figure 36a shows the type of "hot-spots" which develop on the brass-blank cathode and Figure 36b shows the enhanced central emission of the "plasma"-center cathode.

Figures 37a,b compare the radiographs for the filled and unfilled cases of the a) Various Hole Size Cathode, b) Narrow Ridge Cathode (See Appendix B for a brief discussion of the possible use of the cathode for launching a "hollow beam" into a drift tube.).

A study of Figures 29-37 has led to the following conslusions:

1) Emission from the brass-blank (all metal) cathode is probably

FIG. 33

DIODE-IMPEDANCE ORDER
FOR
VARIOUS CATHODE TYPES
(EXPERIMENTAL RESULTS)

Z_D - ORDER LOW→HIGH	SHOT NUMBER	V_{MARX} (KV)	CATHODE TYPE	Z_D (OHMS)
1	13	246	SINTERED TUNGSTEN	5.65
2	6	246	PLASTIC-FILLED BRASS	6.35
3	9	246	UNFILLED BRASS	6.87
4	19	246	ALUMINUM WITH RIDGE	7.56
5	23	246	ALUMINUM WITH CROSS	8.00

FIG. 34

DIODE-IMPEDANCE ORDER

PLASTIC-FILLED CATHODES ($Z_D \propto \frac{1}{A}$)

Z_D - ORDER LOW→HIGH	ANODE-CATHODE GAP IN MM.	RELATIVE V_{INPUT}	CATHODE TYPE	A* (SQ. INCHES)	Z_D OHMS (MEASURED)
1	8	1.0	PLASMA	9.69	5.44
2	8	1.0	NARROW RIDGE	2.98	8.02
3	8	1.0	NON-UNIFORM HOLES	0.5	13.8

* CALCULATED AREA OF SURFACES OF THE DIELECTRIC FILLER MATERIAL.

	Cathode Type	Emission Pattern (Filled)	Emission Pattern (Unfilled)
1.	Brass Plasma	Uniform Over Surface, Laminar	Fairly Uniform, Less Regular, Less Laminar
2.	Narrow Ridge	Generally Emission Over Ridge Section Only, Sometimes "Hot Spots" Over Center Area	Maximum Emission at Ridges; Pattern Not As Distinct Over Ridge Area.
3.	Intermediate Ridge	Maximum Emission Still Occurs Over Ridge Edges But Dielectric Fill Enhances Emission Over That of Unfilled Case.	Maximum Emission Over Inside Ridge Edge. Entire Ridge Clear.
4.	Wide Ridge	Maximum Emission Still Occurs Over Ridge Edges But Dielectric Fill Enhances Emission Over That of Unfilled Case.	Maximum Emission From Ridge Edges. Unfilled Area Less Visible.
5.	Various Hole Sizes	Star Shaped Patterns Indicating Dielectric Surface Breakdown-Maximum Emission Over Holes.	Maximum Emission Over Holes.
6.	Sintered Tungsten (EG&G)		Uniform Over Surface.
7.	Plasma (Center Only)		Definitely Enhanced Over Center (Hole Filled) Area.
8.	Cross		Maximum Emission Over Cross. "Hot Spots" Similar to #9 Over Planar Area.
9.	Brass Blank		Random "Hot Spots" Over Surface.
10.	Holes in Outer Edge		Outer Holes Visible - But Pattern Generally Had "Hot Spots" Similar to #9.

Fig. 35. A Tabulation of Observed Emission Patterns of Various Test Cathodes

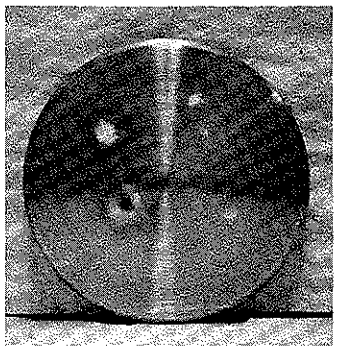

Fig. 36a. Photograph of Brass Blank Cathode After 2 Shots. Note the "Hot Spots".

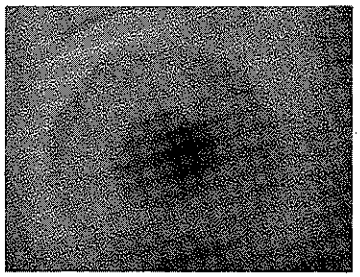

Fig. 36b. Radiograph of "Plasma" - Center Cathode Showing Enhanced Central Emission Region.

Shot #17 of 7/17/68

V_D	I_D	Z_D
460 KV	65.5 Ka	7Ω

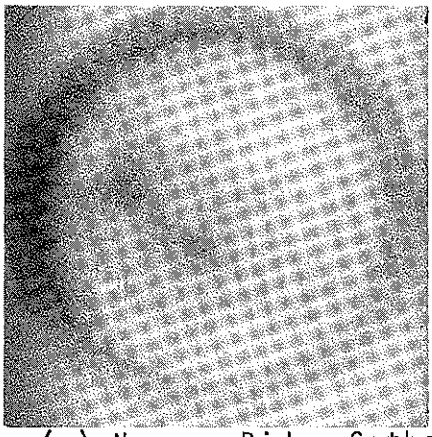

(a) Narrow Ridge Cathode

Shot #9, 1/8/69
V_D=338 KV, I_D=56.7 KA, Z_D=6.0Ω

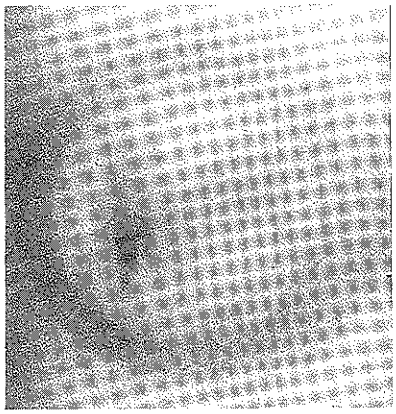

Shot #22, 10/29/68
V_D=396 KV, I_D=52.7 KA, Z_D=7.53Ω

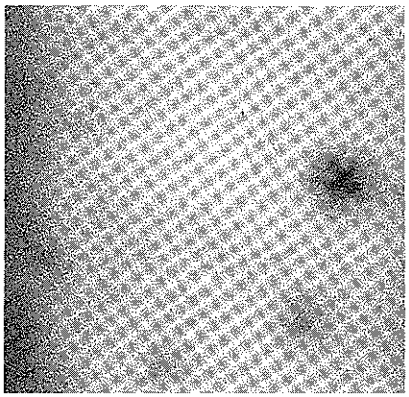

(b) Various Hole Size Cathode

Shot #5, 1/8/69
V_D=272 KV, I_D=50 KA, Z_D=5.44Ω

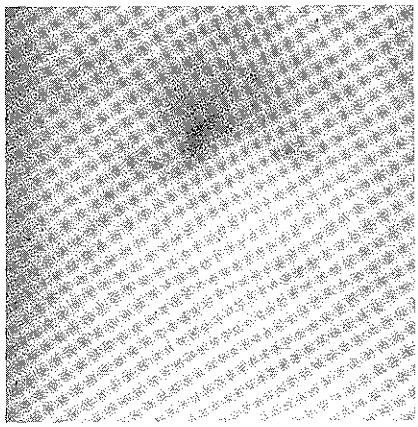

Shot #18, 10/29/68
V_D=363 KV, I_D=48.3 KA, Z_D=7.20Ω

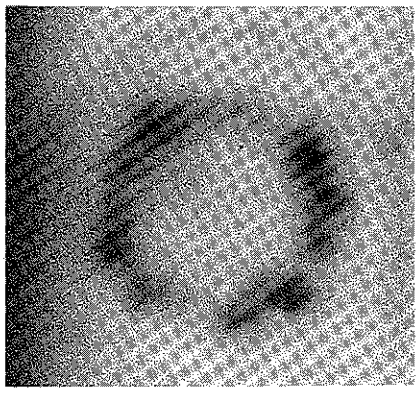

(c) Wide Ridge Cathode

Shot #2, 1/8/69
V_D=300 KV, I_D=66.2 KA, Z_D=4.54Ω

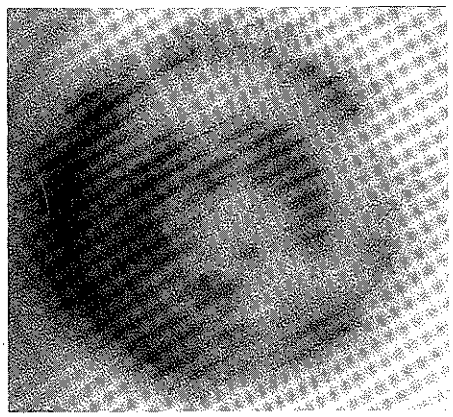

Shot #8, 10/30/68
V_D=330 KV, I_D=40 KA, Z_D=8.3Ω

Fig. 37. Comparison of Radiographs for Filled (Left Side of Page) and Unfilled Cathode Configurations.

best explained by T-F emission, no other known mechanism providing the observed current magnitudes.

2) The overall diode impedance (Z_D) is not a strong function of cathode design (planar anode-cathode geometry). However for a fixed gap we have seen changes in Z_D of 2.7/1 for the shapes tested; the impedance of the cathodes ordering roughly as $Z_D \propto 1/A$.

3) The spatial distribution of electron emission is a strong function of cathode geometry. Maximum emission occurs as expected at field enhanced edges and suggests that a large area uniformly emitting cathode should be of the multi-hole "plasma" type or of the sintered tungsten (EG and G) type. (The "plasma" cathode has the additional advantage of being easily refaced if it becomes coated with anode debris whereas the sintered type must be entirely re-processed.)

4) In all cases tested, the dielectric fill gave a more uniform laminar pattern across the filled surface than the non-filled case, and indicated that the dielectric was undergoing a rapid surface breakdown process. By comparing the surface patterns of the filled various hole size and wide ridge cathodes, the maximum effective track length is estimated at 1 cm , for 50 nsec pulse widths.

5) For the "plasma" cathode the surface-breakdown process and the flow laminarity may be explained by referring to Figure 38, a rough sketch of the electric field lines in the anode-cathode gap region. The electric field vector $\bar{E}$ is seen to be composed of E_z and E_r components, with $E_z \gg E_r$. The large E_z component explains the flow laminarity. E_r is large enough

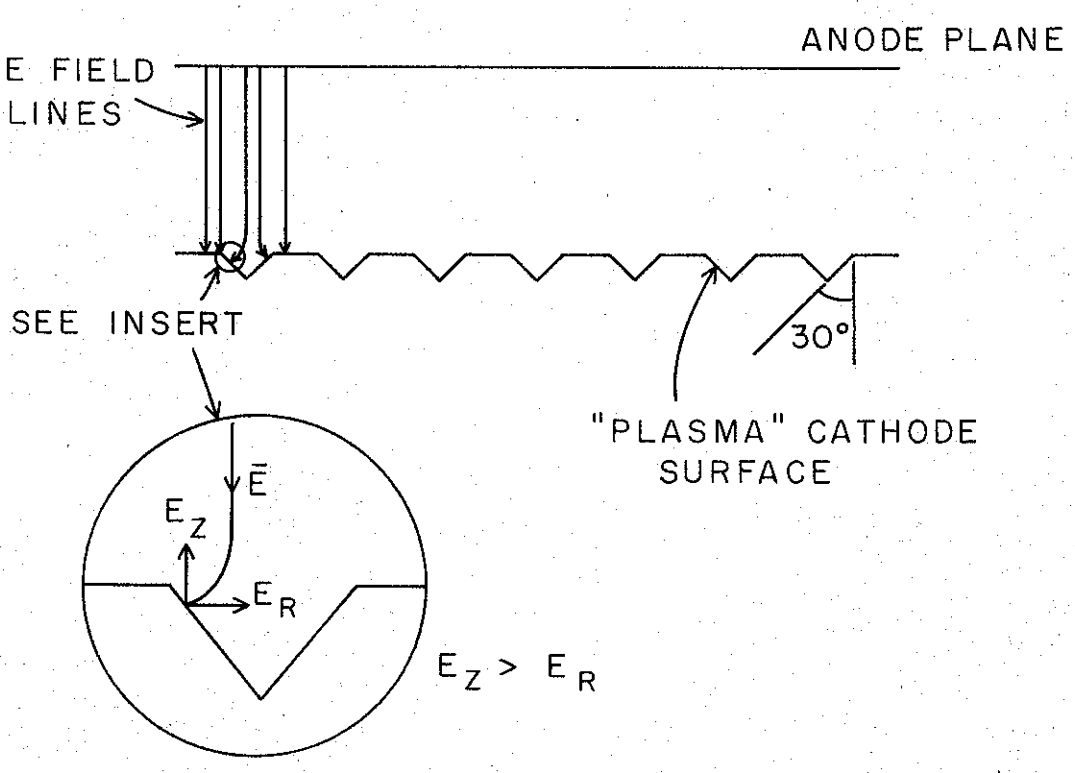

Fig. 38. Rough Sketch of Electric Field Lines in Anode-Cathode Gap.

to either:

a) produce electron multipactoring along the surface of the dielectric studs once field emission has been initiated at the hole edges or

b) produce dielectric surface-flashover similar to that of the lucite insulators discussed in Chapter II (Figure 17a).

For a hole of radius 1.5 mm, E_R (Figure 38) may be estimated as approximately 600 KV/cm which is considerably in excess of the 50 KV/cm required for surface flashover at 0° in Figure 17a.

Such processes in conjunction with cathode sputtering from beam-generated and other ions can easily produce a tenuous plasma sheath over the cathode surface.

2. The Formative Times or Cathode Plasmas

The formative time of such a plasma in the anode-cathode gap region of a diode similar to Cornell's has been studied at Ion Physics Corporation.[22] At pressures of 3×10^{-5} torr and a gap of 1 cm, the time history of the anode-cathode gap spectra were studied by means of 0.5 meter Jarrel-Ash monochrometer and an Amperex XP1003 S-20 photomultiplier. Using an aluminum cathode:

the Al^{I} (3961 Å) line peaked 180 nsec after the electron peak

Al^{II} (3587 Å) line " 75 " " " " "

Al^{III} (3601 Å) line " 80 " " " " "

The Ion Physics Corporation study concluded:

"The question of the time growth of a plasma around cathode tips was studied experimentally, and indicate that the tenuous plasma forms quite quickly. Both residual gas species and cathode material species

were observed in the plasma, the cathode material being the dominant member. This suggests that either vaporization of minute whiskers from the cathode or sputtering of the cathode itself is responsible for the growth of the plasma. In any case, the presence of the plasma suggests that a space-charge-limited emission mechanism if probably operative. This assumption is supported by the good agreement obtained when comparing predicted and empirical evidence for one known geometry."

CHAPTER IV - BEAM ENTRANCE CONDITION STUDIES

The effects of the dielectric sections of the cathode on the observed spatial distribution of diode current were noted in Chapter III. The presence of a plasma sheath in front of the cathode which serves as the source of electrons for the space-charge-limited flow measured in Chapter II has been postulated. The study of other diode parameters which have a pronounced effect on the observed spatial distribution of current at the anode plane is now described. Data on these diode parameters is extremely important because the propagation characteristics of the electron beam in the drift tube* are in turn critically dependent on the spatial distribution of current and the angular spread of the electron trajectories at the anode plane. (See Section 2 of this chapter.)

A. TIME-INTEGRATED CURRENT DISTRIBUTION STUDIES

1. Radiograph Measurements

Radiographs (magnification $\approx \frac{1}{2}$) similar to those discussed in Chapter III were made of the "plasma" cathode for a variety of input voltages, pressures and anode-cathode gaps. Most of the radiographs showed a honeycomb type emission pattern, the resolution of which indicated reasonably laminar flow. In addition the pattern was quite uniform in intensity and regularity across the cathode surface (See Figure 39a). A number of radiographs, however, showed distinct skewing of the beam to the downstream side of the diode (Figure 39b), and, in certain cases

*See Appendix A, "High Current Relativistic Electron Beam Propagation Characteristics - A Summary"

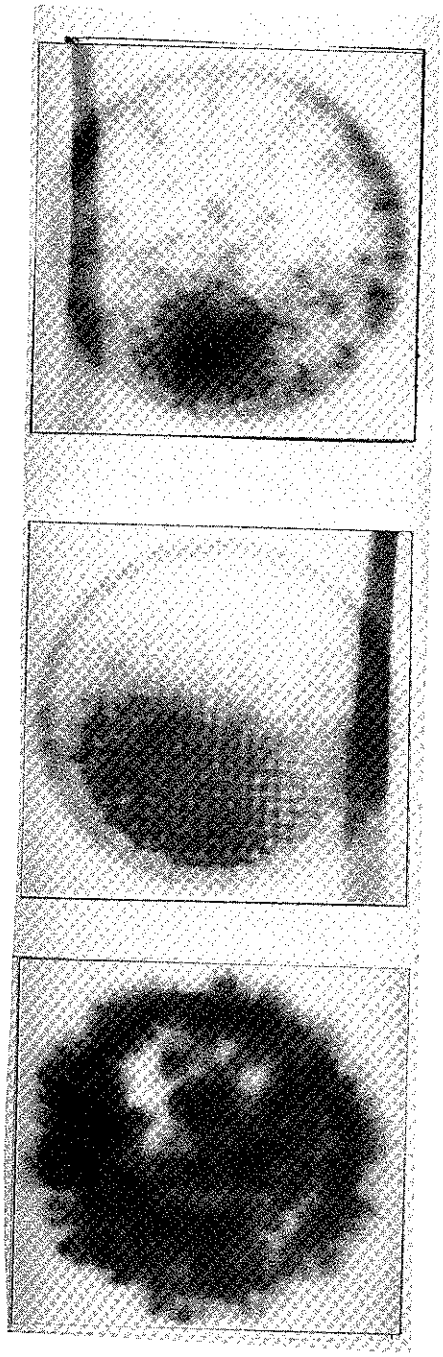

		V_D	I_D	Z_D	GAP	$\frac{V}{\gamma}$ critical	$\frac{V}{\gamma}$ measured
Fig. 39a	UNIFORM EMISSION	457 KV	58 KA	7.85Ω	.351"	2.83	1.86
Fig. 39b	SKEWED EMISSION PATTERN	366 KV	78 KA	4.7Ω	.290"	3.45	3.31
Fig. 39c	SKEWED AND PINCHED EMISSION PATTERN	372 KV	71.5 KA	5.2Ω	.290"	3.45	2.93

Fig. 39 Radiographs of Various Cathode Emission Patterns

(Figures 39c), both skewing and radial compression of the beam was observed. This evidence of decrease in laminarity of electron flow will henceforth be called "pinching." In Section IV.B it will be shown that the ions in the gap remain essentially stationary. Consequently this pinching* effect is not to be confused with the usual linear pinches encountered in other areas of plasma physics where ion drag is important.

The question posed by the radiographs was "What are the conditions for which electron flow between parallel-plane electrodes becomes so affected by the self-generated magnetic field of the electrons that the original laminar flow becomes seriously degraded?". A simple model for the prediction of this pinch condition in the diode-gap region has been proposed by Friedlander[14] et al and is summarized as follows:

"In the cathode-anode region of an electron gun, the situation can be quite different (i.e. from that of a propagating electron beam). In the limit where the beam cross section is much larger than the cathode-anode distance, the space-charge field is almost entirely axial. The radial space charge force approaches zero. The self-magnetic field, however, is essentially unchanged by the cathode-anode geometry because the magnetic field depends only on the current enclosed by the integration path which in this case is a ring about the beam axis. Radial currents in the anode, or coaxial return currents outside the gun, will not be enclosed by an integration path inside the cathode-anode space and therefore will not change the magnetic field.

---

*Similar diode pinching has been noted elsewhere [2,11,14,15,31] but no detailed systematic measurements to determine the conditions for which such pinching occurred had been carried out.

The lack of an outward space charge force to balance the inward self-magnetic field force in a planar gun will result in a convergence of the beam, making planar flow in a planar geometry impossible above a certain current and voltage level. Since the self magnetic force ($F_m = - \frac{ev\mu\ Jr}{2}$) increases with radius, the most extreme convergence will occur for the outermost electrons, the field at the edge of the beam being given by

$$B_\phi = \frac{-\mu I}{2\pi r} \tag{84}$$

where I is the total beam current.

Electrons at the edge of the beam in the cathode-anode region will perform quasi-cycloidal motion due to the self-magnetic field and the applied electric field. Assuming a constant magnetic field given by equation (84) the cycloid radius is given by

$$r_{cycloid} = \frac{mv}{eB_\phi} \tag{85}$$

where m is the relativistic mass and v is the velocity, both of which are assumed constant. To estimate a limiting criterion for the diode, we will investigate the condition for which the cycloid radius equals the diode spacing. With this condition applied to equation (84) and (85) we have:

$$\frac{mv2\pi r}{e\mu I} = d \tag{86}$$

$$I_{critical} = \frac{m_o \gamma v}{e\mu} \frac{2\pi r}{d} \cdot c = \frac{2\pi m_o c^2}{e}\sqrt{\frac{\mu}{\epsilon}}\frac{r}{d} B\gamma = 8500 \frac{r}{d} B\gamma \tag{87}$$

where d is the diode spacing; $\beta = \frac{v}{c}$ and γ is the relativistic mass factor, $\gamma = \frac{1}{(1-\beta^2)^{1/2}}$."

He concludes: "The limiting current expression given by equation (87) is clearly based on rather restrictive assumptions; however it can be used to estimate conditions under which self magnetic fields will play an important role in determining the electron flow."

In terms of the Lawson model (Appendix A) we have:

$$I_{LAWSON} = 17{,}000\ B\gamma \quad \text{and} \quad \nu = \gamma \quad , \quad \frac{I_{PINCH}}{I_{LAWSON}} = \frac{r}{2d} \tag{88}$$

$$\left.\frac{\nu}{\gamma}\right|_{\substack{CRITICAL \\ PINCH}} \geq \frac{r}{2d} \tag{89}$$

A comparison of the measured values of ν/γ for the radiographs of Figures 39a-c, with $\nu/\gamma/_{critical}$ and measured Z_D shows the general departure from laminar flow as $\nu/\gamma/_{measured}$ approaches $\nu/\gamma/_{critical}$. It is notable that the beam pattern which is both skewed and pinched occurs for a lower relative value of ν/γ but a higher value of Z_D than for the skewed beam only. This phenomenon has occurred consistently but cannot presently be explained. A review of the radiographs and data for other cathode shapes (Figure 40) indicates that the model is consistent and independent of cathode type (planar anode-cathode geometry) as expected. This is perhaps, most clearly shown for the half/half cathode in Figure 41.

The measured densitometer density range of Figure 41b is

$$\frac{13}{20}\ (\text{codes}) \times 1.5\ (\text{Range}) = .975 \quad .$$

where "codes" refers to steps in the densitometer calibration and "range" refers to the total density range of the instrument. The γ of the X-ray film, (defined as $D_2\text{-}D_1/\log E_2 - \log E_1$), where D = film density and E is exposure) is ≈ 3. Therefore

SHOT NO.	DATE	V_D(KV)	I_D(KA)	Z_D(Ω)	CATHODE TYPE	$\frac{\nu}{\gamma}$/CRITICAL	$\frac{\nu}{\gamma}$/MEASURED
4	7/17/68	400	67.2	5.95	Brass Plasma Filled	2.9	2.64
6	7/17/68	480	75.5	6.35	Brass Plasma Filled	2.9	2.67
10	7/17/68	520	79.0	6.57	Brass Plasma Unfilled	2.9	2.71
13	7/17/68	260	46.0	5.65	Sintered Tungsten (EG&G)	2.9	2.30
5	7/18/68	460	74.0	6.22	Cross Cathode	2.9	2.71
22	7/18/68	520	73.2	7.1	Cross Cathode	2.9	2.51

Fig. 40. Data on Cathode Types for Which "Pinching" Has Occurred.

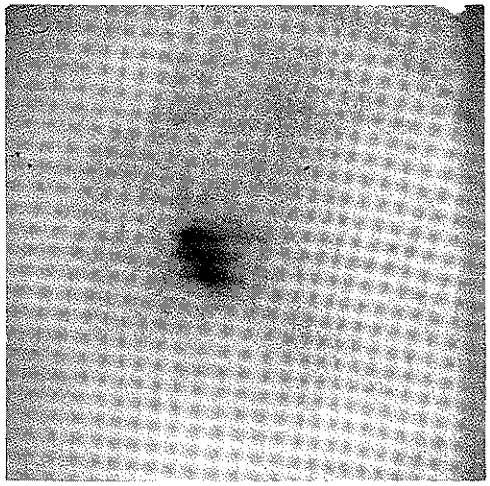

(a) Radiograph of Half/Half Cathode, Shot #2, 10/30/68
(Left Half Filled, Right Half Unfilled)
V_D=379 KV, I_D=58.5 KA, Z_D=6.5Ω

$\frac{\nu}{\gamma}\Big|_{Critical}$=4.2; $\frac{\nu}{\gamma}\Big|_{Measured}$=3.2

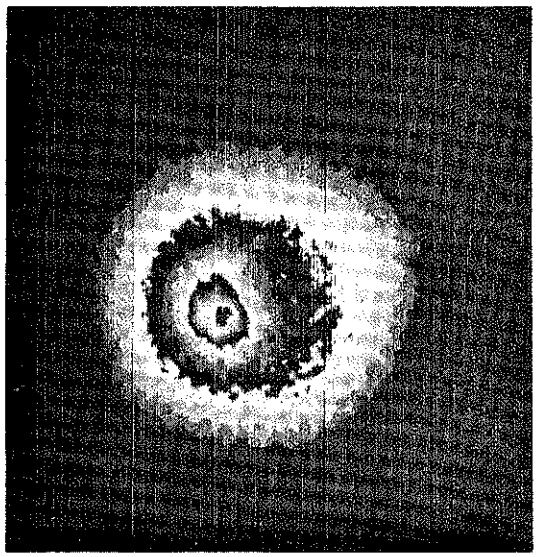

(b) Densitometer Trace of Radiograph Shown in (a) Above.

Fig. 41. Radiograph & Densitometer Trace of Half & Half Cathode (Pinched Mode).

$$3 = \frac{.975}{\log E_2 - \log E_1} \qquad \text{or} \qquad \frac{E_2}{E_1} = 2.12 \ ;$$

i.e. the ratio of pinch spot intensity to that of the background is 2.12/1.

An operational curve used to quickly estimate $\nu/\gamma\big|_{measured}$ from the diode voltage (V_D) and current (I_D) scope traces is presented as Figure 42. (For a measured diode voltage (V_D) $17\beta\gamma$ is read from Figure 42 and divided into the measured diode current (I_D in KA) to find $\nu/\gamma/_{measured}$.)

2. Distributed Calorimeter Measurements

The diode-pinch mode was next studied for ν/γ both less than and greater than $\nu/\gamma_{critical}$ by means of a segmented graphite calorimeter mounted 1 mm behind the anode foil.

The calorimeter consists of a 5 x 5 array of 1 cm square by .63 cm thick graphite blocks surrounded by four 2 cm x 1 cm x .63 cm and twelve 2 cm x 2 cm x .63 cm blocks (Figure 43). The total array is 9 cm by 9 cm compared to a cathode diameter of 10 cm and a drift tube (if used) diameter of 14 cm . Each graphite block has a thermocouple embedded in the back of it and the wires from the array are fed into a 100 channel scanner which enables each thermocouple to be sampled at least once every two seconds. The scanner output is amplified and recorded on a Visicorder Oscillograph. The temperature rise for each block is proportional to the beam energy deposited therein and has been calibrated as 3/4 joule per centigrade degree for the small square blocks, twice that for the rectangular blocks, and four times that for the large square blocks.

The increase of pinching with increasing $\nu/\gamma/_{measured}$ is evident (Figure 44) and conforms to the model. Note that even for the low $\nu/\gamma/_{measured}$ case (1.76) there is some skewing of the beam to the left

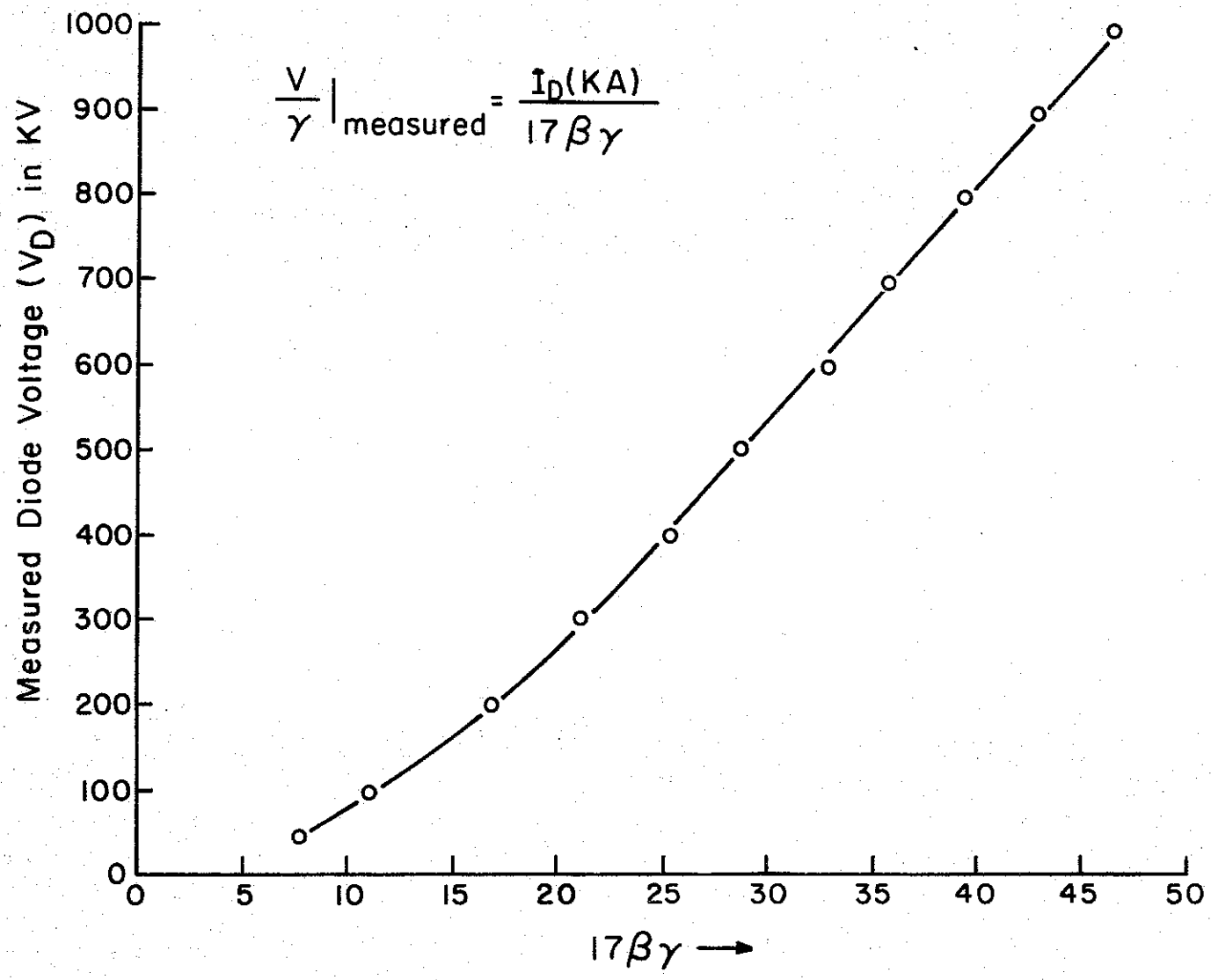

Fig. 42. An Operational Curve for Determining $\frac{V}{\gamma}/_{measured}$ From V_D and I_D Oscilloscope Traces.

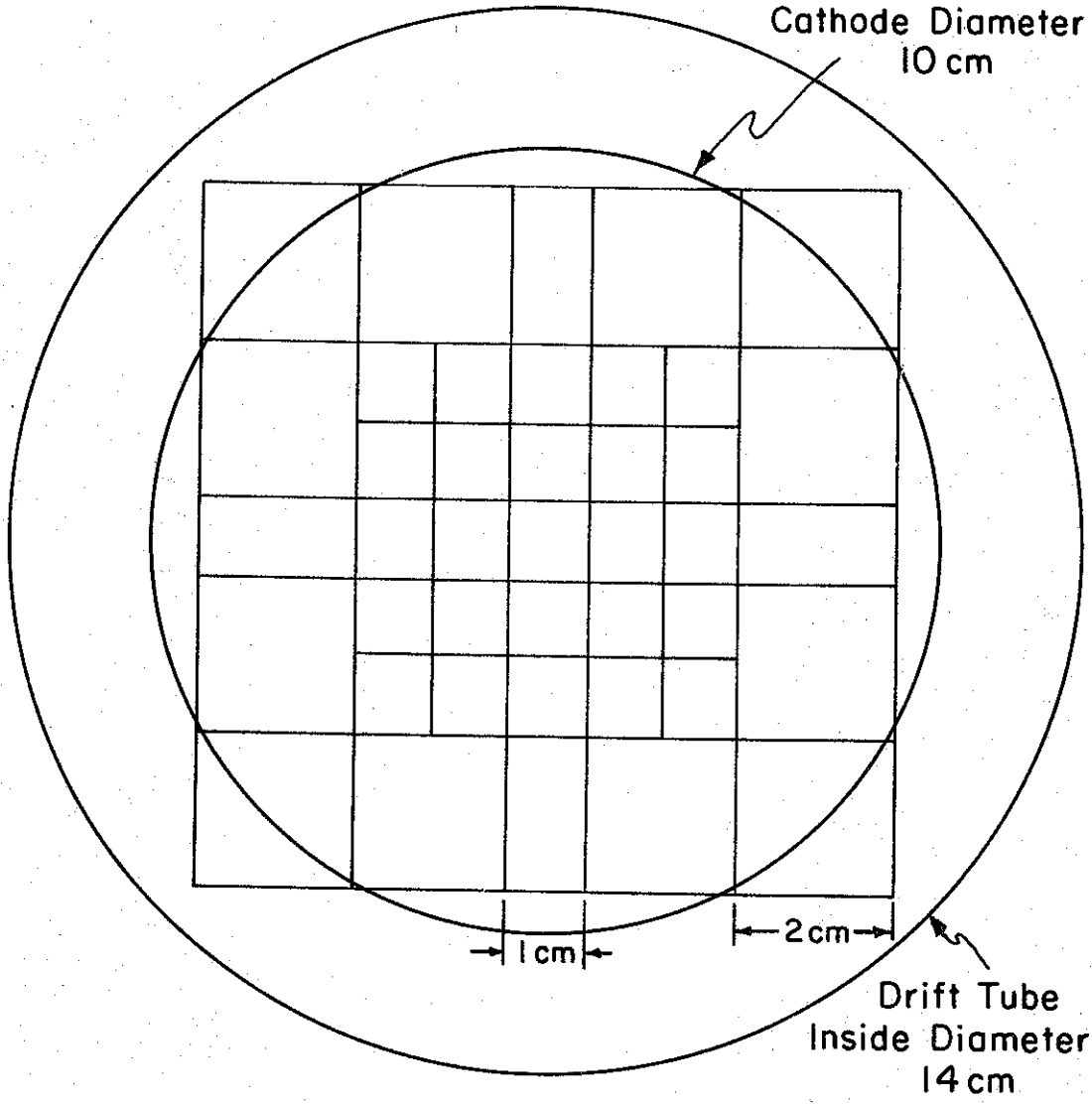

Fig. 43. 41 Point Segmented Calorimeter Array

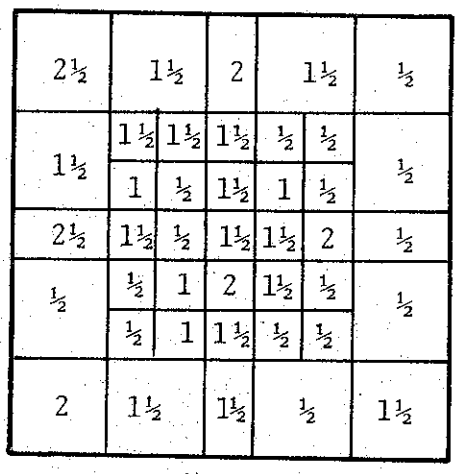

i. $\frac{\nu}{\gamma} \approx 1.7$

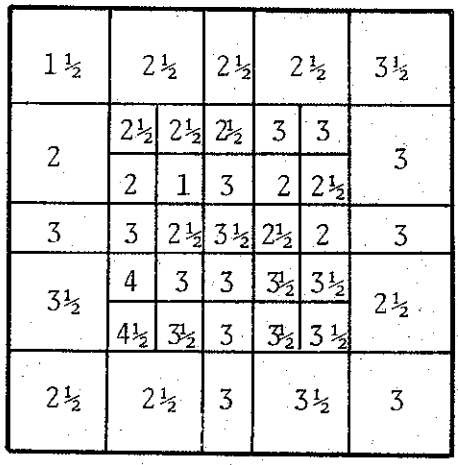

ii. $\frac{\nu}{\gamma} \approx 2.3$

Numbers are temperature rise in Centigrade degrees.

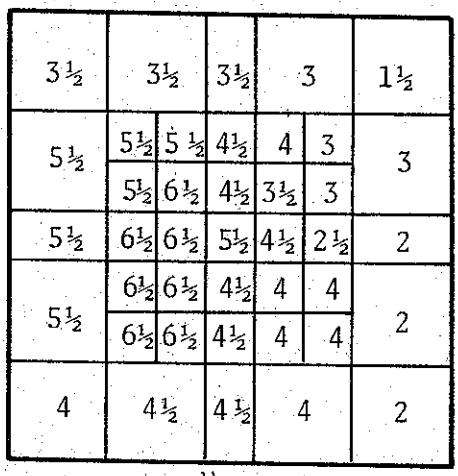

iii. $\frac{\nu}{\gamma} \approx 2.8$

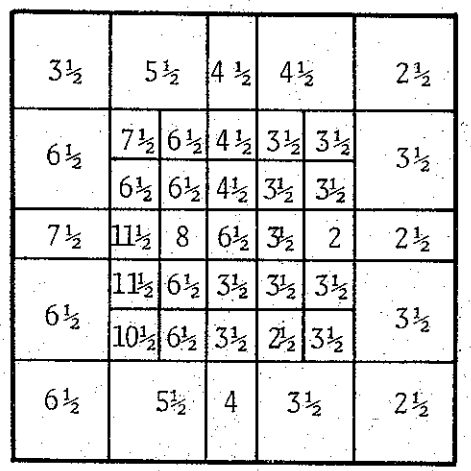

iv. $\frac{\nu}{\gamma} \approx 3.4$

Figure 44

Segmented Calorimeter Data at 1 Millimeter

Shot Data	i.	ii.	iii.	iv.
Shot Number and Date	5-3/15/69	2-3/19/69	3-3/15/69	11-3/19/69
Drift Tube Pressure	Same as Diode Pressure-Less than .0005 torr			
Diode Voltage(Ave.)	400KV	320KV	430KV	350KV
Diode Current(Peak)	44KA	49KA	75KA	77KA
Diode Impedance	9.20Ω	6.43Ω	5.73Ω	4.52Ω

(Listed $\frac{\nu}{\gamma}$ was calculated from peak current. Average values are about 70% of those listed. $\left.\frac{\nu}{\gamma}\right|_{critical} = 2.81$; d= 0.89 cm.)

(i.e. downstream) side of the matrix. This type of offset is believed to be due to the non-symmetrical feed of the Cornell diode since the geometrical alignment and gap spacing of the diode have been carefully checked. The offset is consistent with both the radiographs and the diode toroidal resistor measurements (Figure 15) mentioned earlier.

Other Cornell thermocouple data[23] taken at 0.3 and 2 $\frac{1}{2}$ meters indicate that there is a strong tendency for the diode pinch to be perpetuated as the beam propagates down the drift tube, even though the $\nu/\gamma_{measured}$ at the calorimeter has fallen well below the value in the diode. The azimuthal position of the pinch is not necessarily maintained as the beam propagates and this may be due to image forces in the conducting walls of the drift tube.

The data of Figure 44 represent about 30% of the initial beam energy since a fine (No. 100) stainless steel mesh, which is only 30% transparent to the beam electrons was used as the anode. The net transmitted energy measured by the calorimeter may therefore be compared to that obtained from the beam current and voltage monitors in $0.3\int_0^\infty V_D(t)I_D(t)dt$ obtained from the respective monitor scope and traces. If the diode is reasonably well matched, only the first two voltage and current pulses need be considered since the energy in the remaining pulses is generally below the cutoff energy of the anode foil. For the data here, taken with a mesh there is no such threshold energy cutoff but since $\langle Z_D \rangle$ was approximately 5.5Ω, and the voltage nearly constant, $0.3\int_0^\infty V_D(t)I_D(t)dt$ could be reduced to $0.3\left[\overline{V_D}\ \overline{I_D}\right]_0^{T_{1st\ pulse}}$ and energy comparison checks within 15% could generally be obtained.

3. Diode Pinching in the Presence of an External Axial Magnetic Field

The effects of extending the anode-cathode gap into a uniform magnetic field whose magnitude is of the same order as the self-generated

magnetic field of the beam is shown in Figure 46.[24] The experimental setup is shown in Figure 45. The zero applied-field case (Figure 46a) shows the usual skewing of the beam to the left (downstream) side of the diode. Figure 46b, shows the increase in laminarity for a 10 KG applied axial field (one shot) and indicates that the cathode hole edges are the main source of electron emission (as discussed in Chapter III).

Figure 46c shows a 10 mil SS mesh used as an anode for three shots, the first without an external guide field and the last two with an 8 KG applied field. The edge emission occurred on the first shot and there was enhanced emission on the downstream side. The excellent laminarity for the last two shots is evident. It is believed that the hole (pattern) gradually fills in as successive shots etch the mesh. A comparison (if possible) of the hole-edge intensity to the hole center intensity would give a crude estimate of the ratio E_Z to E_R (See Chapter III, Figure 38).

B. TIME-DIFFERENTIATED CURRENT DISTRIBUTION STUDIES

1. Description of the Experimental Setup

The time-history of the diode-pinch mode was obtained by means of a TRW Image Converter camera and a masking technique described below. The camera is a modified image-converter tube fitted with an objective lens in front of the photocathode and a Polaroid camera behind the photoanode. The modifications involve placing a grid behind the photoanode so that the camera can be electronically "shuttered," and the addition of deflection plates so that the photoanode image can be rapidly deflected vertically.

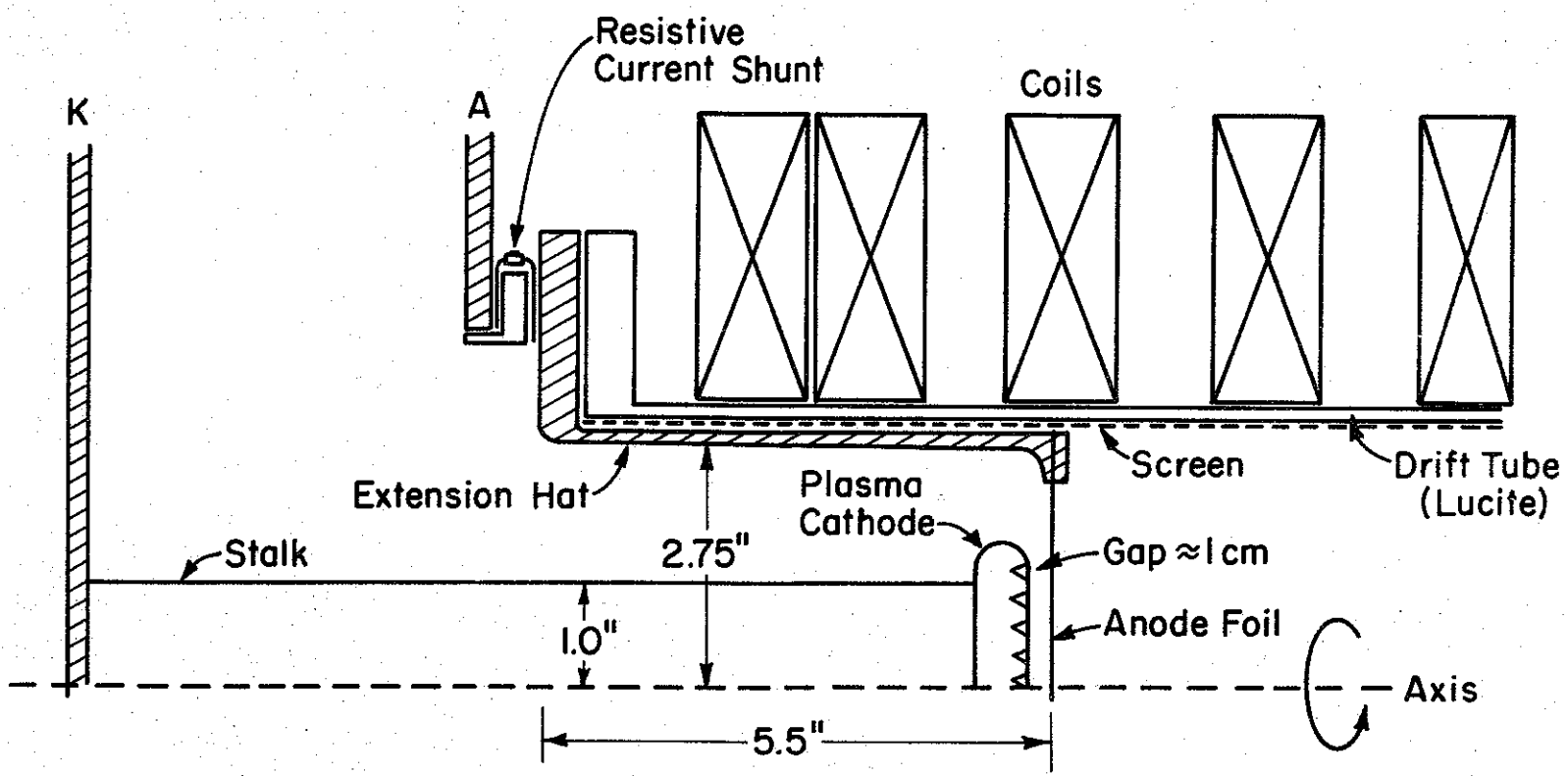

Fig. 45. Cathode-Anode Gap Extension Into a Uniform Field

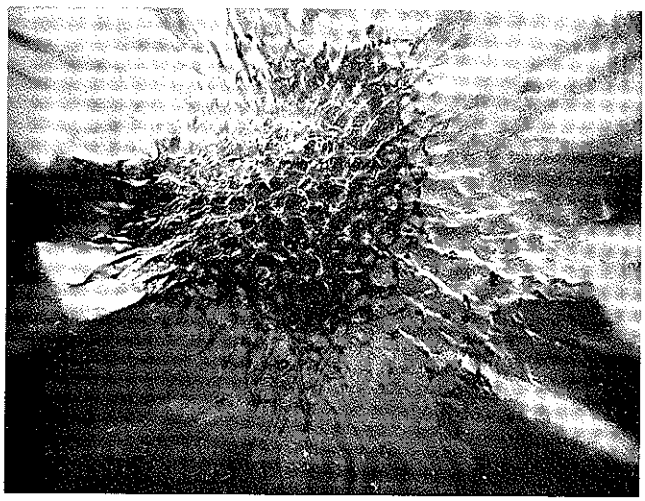

(a) No Magnetic Field Case
V_D= 250 KV, I_D= 37 KA
P_{DIODE}= 2×10^{-4}TORR,
$P_{DRIFT\ TUBE}$= 250μ
Foil: 1 Mil Titanium
$\frac{\nu}{\gamma}\Big|_{Critical}=2.5; \frac{\nu}{\gamma}\Big|_{Meas.}=1.89$

(b) 10 KG Field
V_D=240 KV, I_D= 37 Ka
P_{DIODE}= 2×10^{-4}TORR;
P_{DRIFT}= 300μ
Foil: 2 Mil Titanium
$\frac{\nu}{\gamma}\Big|_{Critical}=2.5; \frac{\nu}{\gamma}\Big|_{Meas.}=1.90$

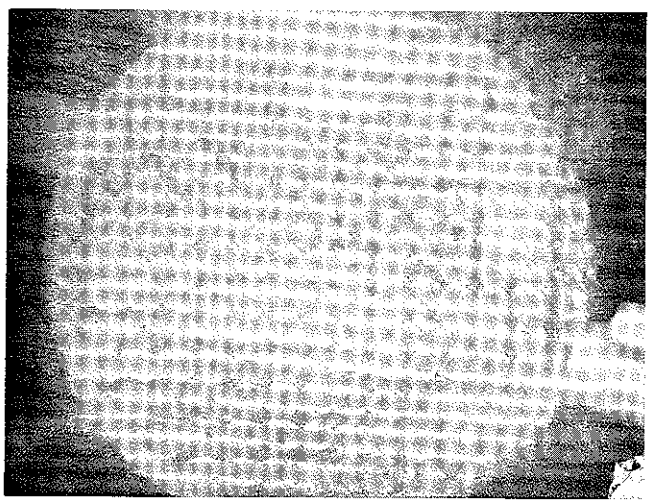

(c) 8 KG Field
V_D= 350 KV, $I_D \cong$ 40 KA
$P_D = P_{DT}$= 2×10^{-3}TORR
Foil: 10 Mil S.S.
$\frac{\nu}{\gamma}\Big|_{Critical}=2.5; \frac{\nu}{\gamma}\Big|_{Meas.}=1.72$

(After 3 Shots)

Fig. 46. Photographs of Anode Foils Used in Magnetic Field Pinching Experiment.

With these modifications and various available plug-in units the camera is capable of both framing and streak modes of operation. In the fast framing mode, three 17 x 25 mm pictures can be taken in rapid succession (i.e. intervals of 50, 100, and 200 ns) with exposure times of 5, 10 or 20 nsec. In the fast streak mode the camera causes the photo-anode image to sweep vertically (bottom to top of picture) a distance of 50 mm , in times of 20, 50, 100 and 200 nsec. In general, the streak mode is most useful if the object to be photographed can be reduced to a horizontal line, the resulting picture providing a time history of each point on the line for the duration of the streak.

The camera requires a trigger pulse of +300 volts (minimum) with a 10 nsec rise time to initiate either its framing or streak operations. Since the time jitter in the solid dielectric switch breakdown voltage was approximately $\pm$ 100 nsec it was not possible to use the Marx spark column trigger as a simultaneous command signal to the camera. It was decided to use a magnetic pick-up loop placed either above or below the Blumlein switch section. When the Blumlein switch fires, ($di/dt \approx 10^{13}$ amp/second) current flows from the outer conductor through the switch to the inner conductor giving rise to a magnetic field in the vertical direction. A wire loop placed nearby will intercept the flux lines, and if a small break is made in the loop, a potential difference proportional to $\dot{B}$ is available at the loop ends. A continuous length of 50Ω solid outer conductor styroflex cable was used as pick-up loop by clamping the center conductor to the outer conductor at one end. Some difficulty was found in orienting the loop so that it would discriminate between the $\dot{B}$ of the Marx, which would shutter the camera too soon, and that of the Blumlein switch. Eventually discrimination ratios of 3/1 were obtained and these proved quite satisfactory.

2. Fast-Framing Camera Studies of the Plasma Cathode

The first framing camera observations of diode pinching were observed in October-December 1968 in photographing the beam as it bombarded a quartz disk and caused the emission of light. The experimental setup was similar to that of Figure 27, with the framing camera positioned alongside the Super Graphic camera. Monitor pulses from the framing camera were time synchronized with the anode x-ray pulse (as recorded by an x-ray scintillator photo-diode of negligible time delay) and indicated that the pinching occurred approximately 35 nsec after the start of diode-current flow. Typical data for these pinched shots are:

SHOT NO.	DATE	V_D(KV)	I_D(Ka)	Z_D	d(cm)	$\nu/\gamma/_{measured}$	$\nu/\gamma/_{critical}$
5	12/13/68	322	68	4.74	0.89	3.2	2.81
7	12/13/68	300	64.5	4.66	0.89	3.0	2.81

These results were of considerable interest because they again confirmed the validity of Friedlander's model, but the quality of the photographs was not good, and the question was raised as to whether or not surface phenomena on the quartz target was responsible for some of the emitted light. To remove this difficulty, a masking technique (Figure 47) was devised which was capable of decreasing the primary beam current to a level that would not cause heat damage to a fast rising (~ 3 nsec) scintillator material (Pilot "B" scintillon).

Electrons leaving the plasma-cathode surface pass through a 30% transmitting .010" stainless steel mesh anode. The transmitted electrons next encounter two layers of .005" or .002" Al, one layer of .010" black drawing paper (used to absorb the light reflected in the back direction and prevent it from reducing the overall resolution) and

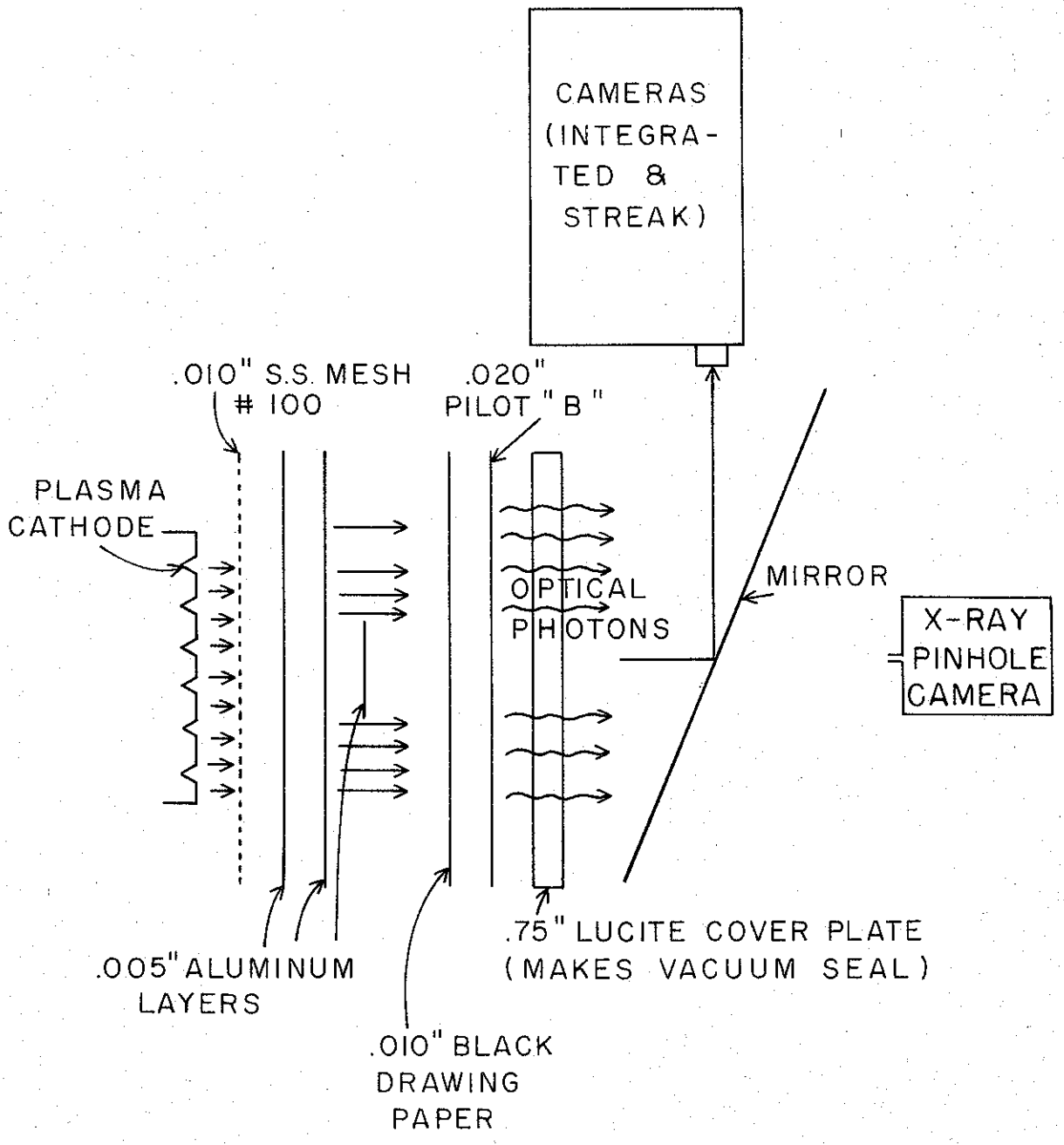

Fig. 47. Masking Technique for Time-Differentiated Electron-Beam Studies.

finally a .020" layer of scintillon. The calculated penetration depth of 300 KV electrons is ≈.012" of aluminum, while the absorption length of the x-rays produced by both the S.S. mesh and the aluminum sheets is a few centimeters. Since the electrons which reach the scintillon are more effective in producing optical photons in the scintillon than the x-rays which reach it (by a factor of at least 10^3), a scintillon sheet thin enough to pass the x-rays with little optical excitation allows one to discriminate against the x-rays, and in effect, optically photograph the electron spatial distribution. Figure 48a is a time-integrated photograph made to test the idea. The black rectangle in the center of the photograph shows that there is no light output from the scintillon over a region where the aluminum mask thickness (.015") exceeds the estimated electron penetration depth* (i.e. .012" for 300 KV electrons). Were the scintillon being excited by x-rays from the S.S. anode, etc. this effect would not be noticeable due to the much longer x-ray range in Al, and the photograph therefore gives the spatial distribution of the electrons.

Figure 48b shows a 5 nsec/frame photograph of the plasma cathode for the following conditions

V_D = 360 KV

I_D = 61 Ka

Z_D = 5.9 Ω

$\nu/\gamma/_{measured}$ = 2.60

$\nu/\gamma/_{critical}$ = 2.95

*The number and thickness of the Al layers is determined by the expected V_D of the shot.

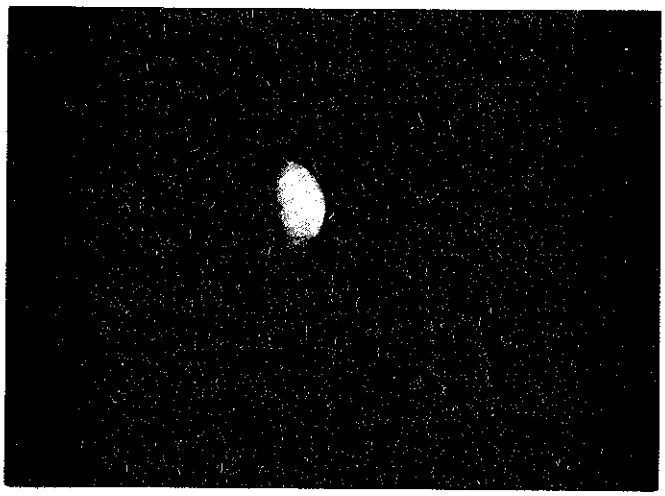

Fig. 48a Time-integrated electron spatial distribution [f/32 + neutral density filter (x 10)].

Time

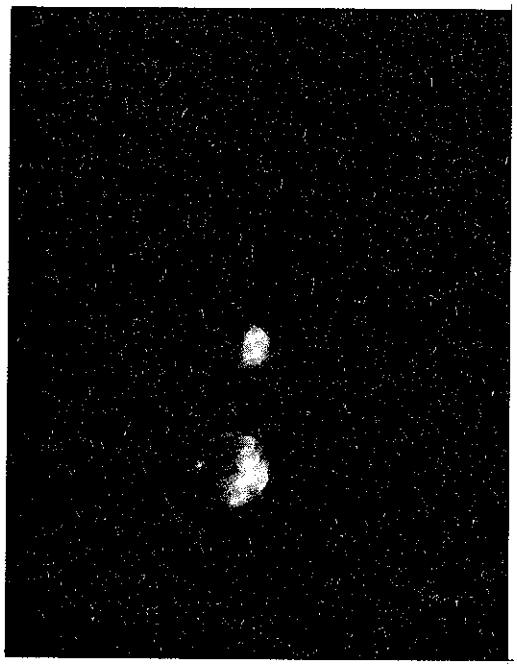

Fig. 48b Time-differentiated electron spatial distribution
5 nsec/frame,
frame separation 50 nsec.
[f/2.0 + neutral density filter (x 40)].

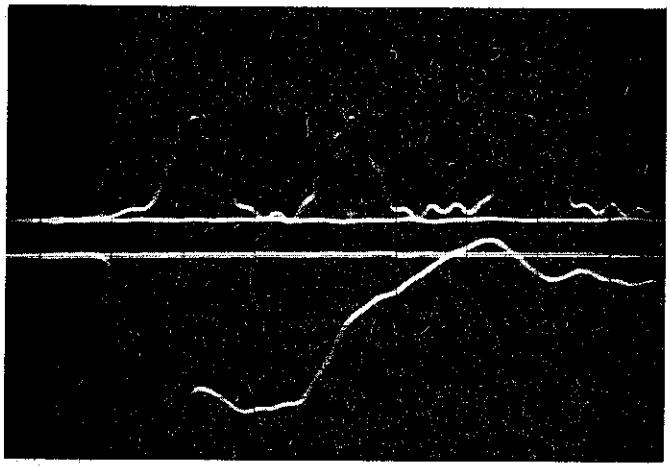

Fig. 48c Lower trace: time-synchronized diode voltage (V_D)

Upper trace: TRW framing camera marking pulses (20nsec./cm)

Figure 48c shows the time-synchronized trace of V_D, versus the framing camera marker pulses and indicates that considerable beam skewing (Figure 48b) has occurred by the time of the first frame, approximately 20 to 30 nsec after the start of the V_D trace.

3. Fast Streak Camera Studies of the Plasma Cathode

In order to acquire a continuous time-history of the diode pinching the streak mode of camera operation was next employed. Simultaneously, it was decided to move the camera away from its original position adjacent to the Blumlein in order to:

1. Decrease the RF noise from the Blumlein and improve the camera focus which was sharper under strobe-light test conditions than during actual shots (although the camera and power supply were inductively decoupled to avoid ground loop currents).
2. Let the increased distance serve as an optical delay line and effectively allow more time for the camera shutter to open.

These aims were accomplished by means of an adjustable objective lens system which allowed us to retain the original image size on the camera film, while simultaneously adding optical delay (~12 ns) and subtracting trigger pulse delay to the streak camera (Figure 49) to improve on the camera "get-away" time. The objective lenses were carefully focussed and the camera lens aperature kept below f/8 to ensure uniform illumination of the photo cathode.

The diode lucite cover plate was masked off with light absorbing black drawing paper except for a slit 1" wide across the horizontal diameter (4.0") of the cathode. This slit (1" by 4") is seen at the camera film plane as a strip image 2 mm high by 8 mm wide. For an unpinched beam, the streak image will therefore be 8 mm wide and for a pinching

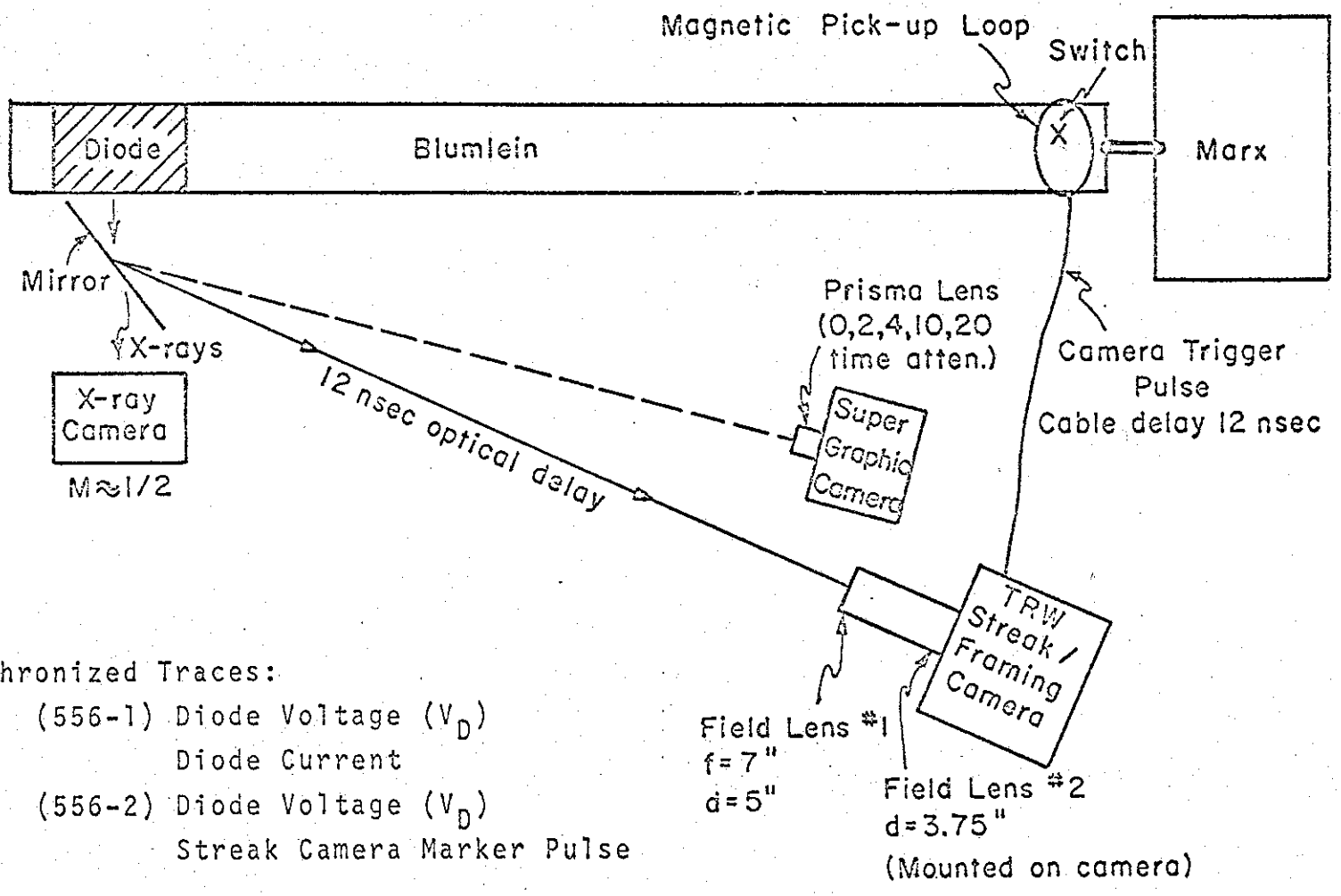

Time-Synchronized Traces:

Tektronix (556-1) Diode Voltage (V_D)

Diode Current

Tektronix (556-2) Diode Voltage (V_D)

Streak Camera Marker Pulse

Fig. 49. Experimental Setup for Streak Camera Data

beam something less than 8 mm . The time resolution of the beam history is equal to the streak speed per mm times the 2 mm height of the undisplaced film-plane image. For the 50 nsec/50 mm streaks the time resolution is (50 nsec/50 mm x 2 mm) = 2 nsec. and for the 100 nsec streaks the resolution is 4 nsec.

The start position of the streak is 9 mm from the bottom edge of the film. To determine when (in real time) events are happening the streak camera marker pulse was time-synchronized with the V_D trace as shown in Figure 51. The time sequence of events for a typical shot is as follows: (Figure 49)

t = 0 Blumlein	Blumlein switch fires
t = 12 nsec	Trigger pulse arrives at Streak Camera
t = 20 nsec	V_D pulse arrives at diode
t = 24 nsec	Streak camera shutter opens (occurs at approximately 90% of Marker Pulse. For a 400 V trigger input this is approximately 12 nsec).
t = 28 nsec, 26 nsec	Streaking Mode initiates for 50 nsec/50 mm, 100 nsec/50 mm mode, respectively.
t = 33 nsec	Light from diode arrives at camera (combined time of transit time of V_D pulse to diode and optical delay from diode to camera).

The start of events occurs at the 90% point of the streak camera marker pulse minus the difference between the time of light arrival at the camera and the streak mode initiation time. (i.e. 33 nsec minus (28 or 26 nsec)).

Figures 50 a-e present fast (50-100 nsec/50 mm) streak camera photographs of the normal (Figure 50b) and the skewed and pinched electron beam in the diode gap, as a function of $\nu/\gamma/_{measured}$ and diode pressure.

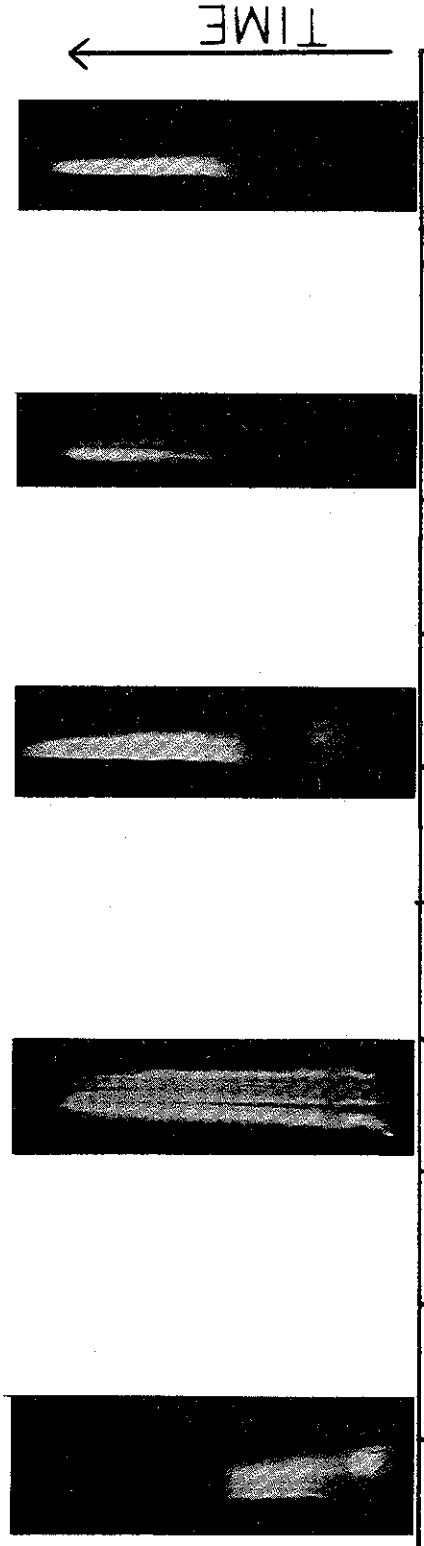

Fig. No.	Streak Duration (nsec)	V_D (KV)	I_D (KA)	Z_D (Ohms)	Gap (Inches)	$\frac{V}{r}$ Critical	$\frac{V}{r}$ Meas.	P_{Diode} (Torr)	Shot - Date
50a	100	386	65.5	5.9	.290	3.45	2.58d	2×10^{-4}	11-5/8/69
50b	50	254	73.2	3.5	.226	4.43	3.87	2×10^{-4}	8-5/14/69
50c	50	350	76.2	4.6	.290	3.45	3.28	11×10^{-4}	7-5/7/69
50d	50	329	70.0	4.7	.290	3.45	3.16	1×10^{-3}	12-5/7/69
50e	50	358	75.0	4.8	.290	3.45	3.22	5×10^{-3}	19-5/7/69

Fig. 50 Streak Camera Photographs of Cathode Emission

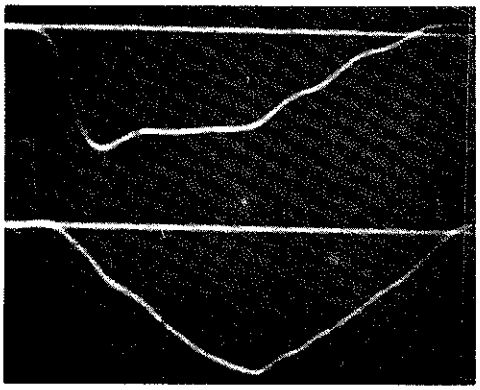

Capacitive Voltage Divider (Shipman Probe) Measurement of V_D. 286 $\frac{KV}{cm}$, 20 nsec/cm.

Torridal Resistor Shunt (I_D) 34 Ka/cm, 20 nsec/cm.

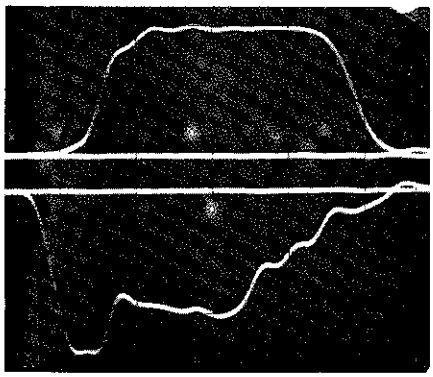

Streak Camera Marker Pulse 5 V/cm, 20 nsec/cm.

Resistive Voltage Divider (V_D) Used as Time Marker Only. 20 nsec/cm.

Fig. 51. Time Synchronized Oscilloscope Traces (Tektronics Type 556) for Streak Camera Photograph of Fig. 50a.

Once again, the Friedlander model holds, - the pinching increases as the ratio of $\nu/\gamma/_{measured} \Big/ \nu/\gamma/_{critical} \longrightarrow 1$. At no time was pinching observed for a ratio less than 0.82. In all cases, the pinching was evidenced in both the radiographs and integrated photographs taken simultaneously with the streak photos. The data of Figures 50c-e show that while the gross diode impedance, Z_D, and $\nu/\gamma/_{measured}$ remained essentially constant with a change in pressure (as had the early Z_D measurements of ChapterII), the distribution of current and laminarity of flow was noticeably pressure dependent.

Friedlander et al[14] have investigated the effects of ion neutralization of space charge flow for a needle and plane diode (by means of an IBM-360/40 computer program) in an attempt to explain why measured currents exceeded non-ion neutralized predicted values.* The computer program provides for the self-generated magnetic field of the electrons. The electron beam generated by the needle and plane diode is reasonably hollow.

The diode analyzed consisted of a cylindrical cathode rod, 13 inches long and 1/8 inch in diameter, with a hemispherical tip having a 1/16 inch radius and a completely planar anode spaced 2.7 cm from the end of the cathode tip. A tabulation of results follows:

Beam Radius of Maximum Current Density at Anode	$I_{measured}$(KA)	$I_{theoretical}$(KA)	% Neutralization
20-25 mm	24		0
33		15.6	0
15		18.8	40
7		24.2	65
1		29.0	80

*Similar to our observations on Z_D in Chapter II.

The convergence of their model at 65% ion neutralization is quite good with respect to total current - but obviously quite poor with respect to current distribution at the anode (i.e. radius of maximum current density) and indicates the complexities of such a theoretical analysis. There is qualitative agreement with our streak results however.

Some physical insight into the increased pinching with increased pressure may be had by assuming that the cancellation of the radial space charge field (E_r) by the proximity of the anode is not complete and is still slightly dependent on the fractional ionization (f).* The range of f, using equations 60 and 63 of Chapter II is tabulated as:

Streak Photo No.	Pressure (torr)	n_e	n_i	$f=n_i/n_e$	K	$(\frac{K}{2})^{1/2}\frac{z}{r_o}$
50 c	1×10^{-4}	1.18×10^{11}	3.56×10^{9}	.031	1.76	0.138
50 d	1×10^{-3}	1.12×10^{11}	3.14×10^{10}	0.288	0.412	.067
50 e	5×10^{-3}	1.15×10^{11}	1.61×10^{11}	1.43	-5.35	.241

where d = .290" = .737 cm

I = .7 I_{PK} (as listed in Figure 50c-e) since N_i of equation 62 is time dependent

T_{pulse} = 50 nsec

n_e = number of beam electrons/cc

n_i = number of beam-generated ions/cc

---

*It is interesting to compare the diode case ($E_R \approx 0$, E_Z large) with that of the Lawson beam model ($E_Z=0, E_R\neq0$) (Appendix A). The listed values of Lawson generalized preveance, $K = \frac{\nu}{\beta^2\gamma}(1-\beta^2-f)$ indicate that such a beam should go from an unpinched condition ($K > 0$) to a pinched condition ($K < 0$).

In addition, from an operational point of view, the noted dependence of pinching on the fractional ionization suggests that to avoid pinching:

a) Diodes for beams with high relative ν/γ ratios should be operated at as low a pressure as is compatible with system pump down time requirements.

b) The cathode and anode materials should be made of high-melting-point materials to reduce anode-cathode sputtering.

The times for the diameter of the beam edge electrons to collapse from its initial value to its final value is estimated as:

Fig. No.	Pressure (torr)	Collapse Time(nsec)	Final Beam mm(film)	Diameter cm(actual)	Initial Beam mm (film)	Diameter cm(actual)
50 c	$1x10^{-4}$	34.5	3.4	4.25	8	10
50 d	$1x10^{-3}$	31	2.8	3.5	8	10
50 e	$5x10^{-3}$	32	2.3	2.88	8	10

The onset time of streak-camera-measured beam diameter collapse was continuously cross checked and found to be in excellent agreement (~2%) with the time required for the diode current (I_D) to exceed $I_{D_{critical}}$, as measured by the diode current shunt.

A simple dynamical pinch theory for the case of a plasma stream of infinite conductivity (the "snow plow" model) predicts[25] that the plasma stream radius, r_s, would collapse due to its self-generated magnetic field at a rate of

$$\dot{r}_s \propto \left(\frac{KI^2}{\rho_m}\right)^{1/4} \qquad (90)$$

where I is the stream current, and ρ_m the plasma density. For our pressure variations of $\frac{50}{1}$ (10^{-4} to 5×10^{-3}) such a model would indicate a variation in pinch times of $\sqrt[4]{50} \approx \frac{2.66}{1}$.

Since our measured radial collapse times are essentially constant with changing pressure, it is believed that only the electrons are taking part in the radial collapse and that the beam-generated ions remain essentially stationary over the pulse times of interest (50 nsec).

C. ELECTRON TRAJECTORY STUDIES

A partial explanation for the onset of pinching at values of $\nu/\gamma/_{\text{measured}}$ at approximately 80% of $\nu/\gamma/_{\text{critical}}$ may be had by recalling that Friedlander assumes that the edge electrons are traveling at a constant velocity, v_z across the gap, in a constant magnetic field, B. In fact, the electrons start out at velocities much less than v_z (i.e. ≈ 0) and the self-magnetic field is a function of both radial position and time, so that the actual electron orbits are complex variations on the usual simple theme of planar magnetron cycloidal trajectories (See Figure 52). For the case of v_{initial} equal to zero the maximum electron displacement in the z direction (Figure 52) is given as[10]

$$z_m = \frac{2a}{\omega^2} = 1.138 \times 10^{-11} \frac{\frac{dV}{dz}}{B^2} \qquad (91)$$

where $a = \frac{e}{m} \frac{dV}{dz}$

$$\omega = \frac{eB}{m}$$

B in webers/m^2 = 10^{-4} gauss

For our case B is the self-generated field of the electrons given by

$$B_\phi = \frac{2Ir}{ca^2} \qquad r < a \qquad (92)$$

$$= \frac{2I}{ca} = \frac{1}{5} \frac{I}{a} \text{ kilogauss } (r = a) \qquad (93)$$

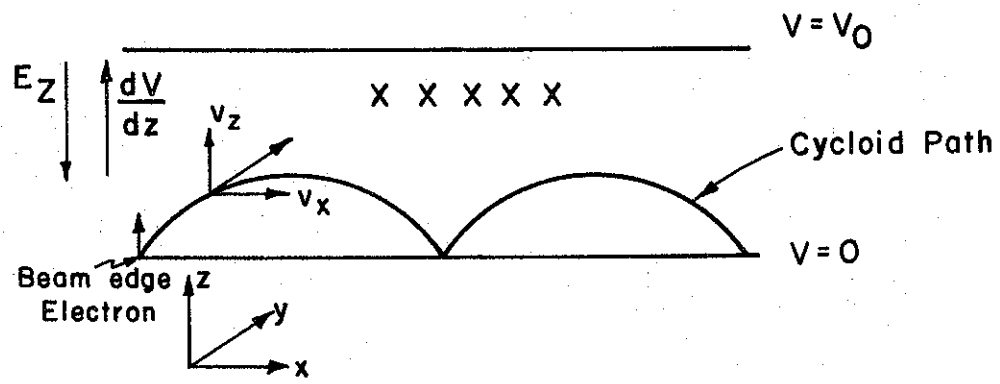

Fig. 52. Electron Motion in a Parallel Plane Magnetron Configuration for the Case $v_{initial}=0$. $E_Z = -\frac{V_o}{d}$, $\vec{B} = B_y$.

where a is beam radius in cm

r is actual radius in cm .

I is the beam current in kiloamps. From the streak data of Figure 50c-e for example, we have:

I = 75 Ka, a = 5 cm, r = 5 cm (electron at beam edge)

B_ϕ = 3 gauss = .3 weber/cm^2

V_D = 350 KV

d = .737 cm

we have:

$$z_{max} = \frac{1.13 \times 10^{-11} \ (4.75 \times 10^7 \ \frac{v}{m})}{(.3)^2 \text{ webers/ } m^2} \qquad (94)$$

$$= .597 \text{ cms} .$$

which says that the outermost electrons don't make it to the anode, but in fact cause crowding for lower currents than expected in the Friedlander $v_{initial} = v_{drift}$ model.

The self magnetic field that would just allow the edge electron to graze the anode for $v_i = 0$ is from equation 91 :

$$B^2 = \frac{1.13 \times 10^{-11} \ (4.75 \times 10^7)}{.737 \times 10^{-2}} \qquad (95)$$

$$B = 2.32 \text{ k gauss} .$$

The ratio of these self fields is $\frac{2.32}{3.00} = .774$ which is very close to our observation that pinching becomes noticeable for $\nu/\gamma/_{measured} \approx .82 \ \nu/\gamma/_{critical}$.

A brief attempt to measure the angular spread of the electron trajectories at the anode plane was made using the experimental setup of

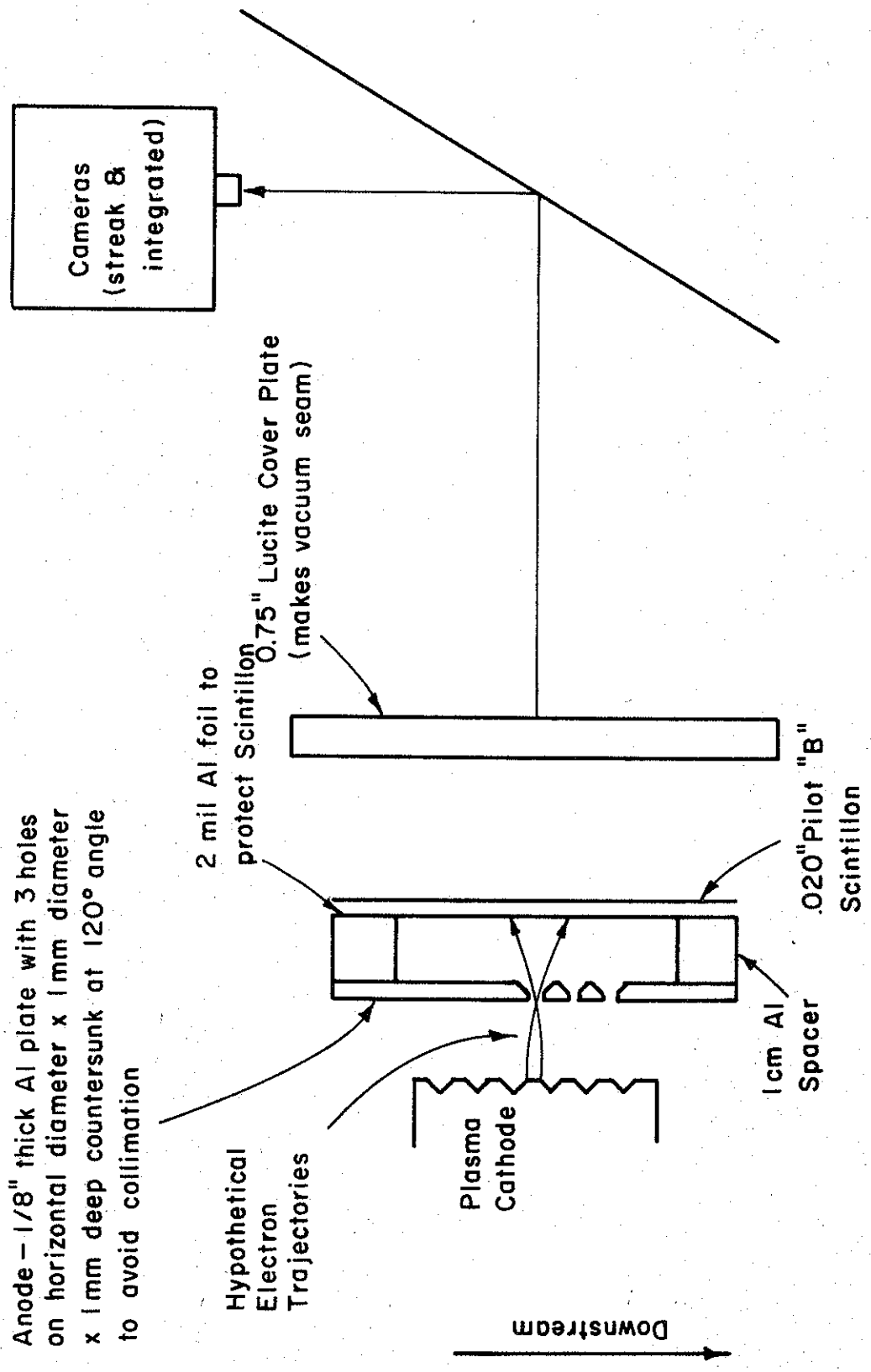

Fig. 53. Experimental Setup For Measuring Angular Spread of Electron Trajectories at Anode Plane.

Figure 53. The selected hole diameter of 1 mm reduces the current/hole to approximately one part in eight thousand of that of the primary beam. The 1 mm hole depth is shown to have enough material remaining to stop electrons outside the hole radius from penetrating the foil and thin enough to avoid collimating those electrons which pass through the hole. The holes are located at the cathode (beam) center and 1 $\frac{1}{4}$" and 2.0" off center. The 1 cm anode-to-scintillon spacing was chosen because for a primary beam of 300 KV and 100 KA, (i.e. the highest expected value of $\frac{\nu}{\gamma}$) the Lawson perfeance* K is:

$$K = \frac{\nu}{\beta^2\gamma}(1-\beta^2-f) = \frac{2}{(.61)^2}\,0.39\,(.59 \times 10^{-3})$$

$$= 1.20 \times 10^{-3} \qquad (96)$$

and $(\frac{K}{2})^{1/2}\ \frac{z}{r_1} < .27$ for less than 10% beam spreading due to electrostatic space charge forces (Figure 55, Appendix A). This gives $\frac{z}{r_1} < 11$, where z is the axial beam distance travelled and r_1 is the original beam radius. Therefore, the angular spread measured on the scintillon will not be enhanced by beam spreading beyond that already present in the anode-cathode gap (even for our assumed f = 0). Data obtained on 5/17/69 are:

---

*For a non-relativistic, unneutralized beam, K = 15000 k where $k = \frac{I}{V^{3/2}}$ amps per (volt)$^{3/2}$. For a completely neutralized beam $K = -2\nu/\gamma = -.06\ I/V^{1/2}$ amps per (volt)$^{1/2}$.

Shot No.	V_D (Ka)	I_D (KV)	Z_D (ohms)	$\frac{\nu}{\gamma}$ critical	$\frac{\nu}{\gamma}$ measured	Relative $\frac{\nu}{\gamma}$	Angular Spread (degrees) Center Hole	Middle Hole	Edge Hole
6	228	40.8	6.89	3.35	2.21	.66	12	9	9
1	286	57.8	4.94	↓	2.72	.81	48	40	no data
5	272	57.8	4.71		2.96	.88	32	29	28
2	314	66.3	4.73		3.01	.90	42	37	31
7	378	74.9	5.06		3.06	.91	34	26	26
8	344	81.0	4.24		3.52	1.05	31	17	25

Figure 54 is a plot of the diode relative ν/γ versus the average angular spread of the electron trajectories at the anode plane, in both the horizontal and vertical directions, for the 3 anode hole positions. The angular spread was estimated by measuring the film image-size of the respective hole, taking into account the demagnification of the camera setup and the known anode-hole to scintillon distance.

From the figure we see that:

a) The angular spread of the electron trajectories increases (as expected) up to $\nu/\gamma/_{relative}$ of .81 but thereafter decreases (or may be constant) as $\nu/\gamma/_{relative}$ increases.

b) The spread is quite small for $\nu/\gamma/_{relative}$ of .66 . This is an accord with Figure 38 of Chapter II.

c) The spread is greatest for the center hole and almost always least for the edge hole. (It is believed that this may be evidence once again of the asymmetry of our system wherein the pinch always occurs to one side of the diode. Hence the trajectories on the downstream edge of the cathode are never as severely distorted from laminar flow as might be expected in the symmetric case.)

d) While there is no gross difference in angular spread in the horizontal plane compared to that of the vertical plane, the horizontal angles are slightly greater in general. This may be caused by the diode asymmetry mentioned earlier.

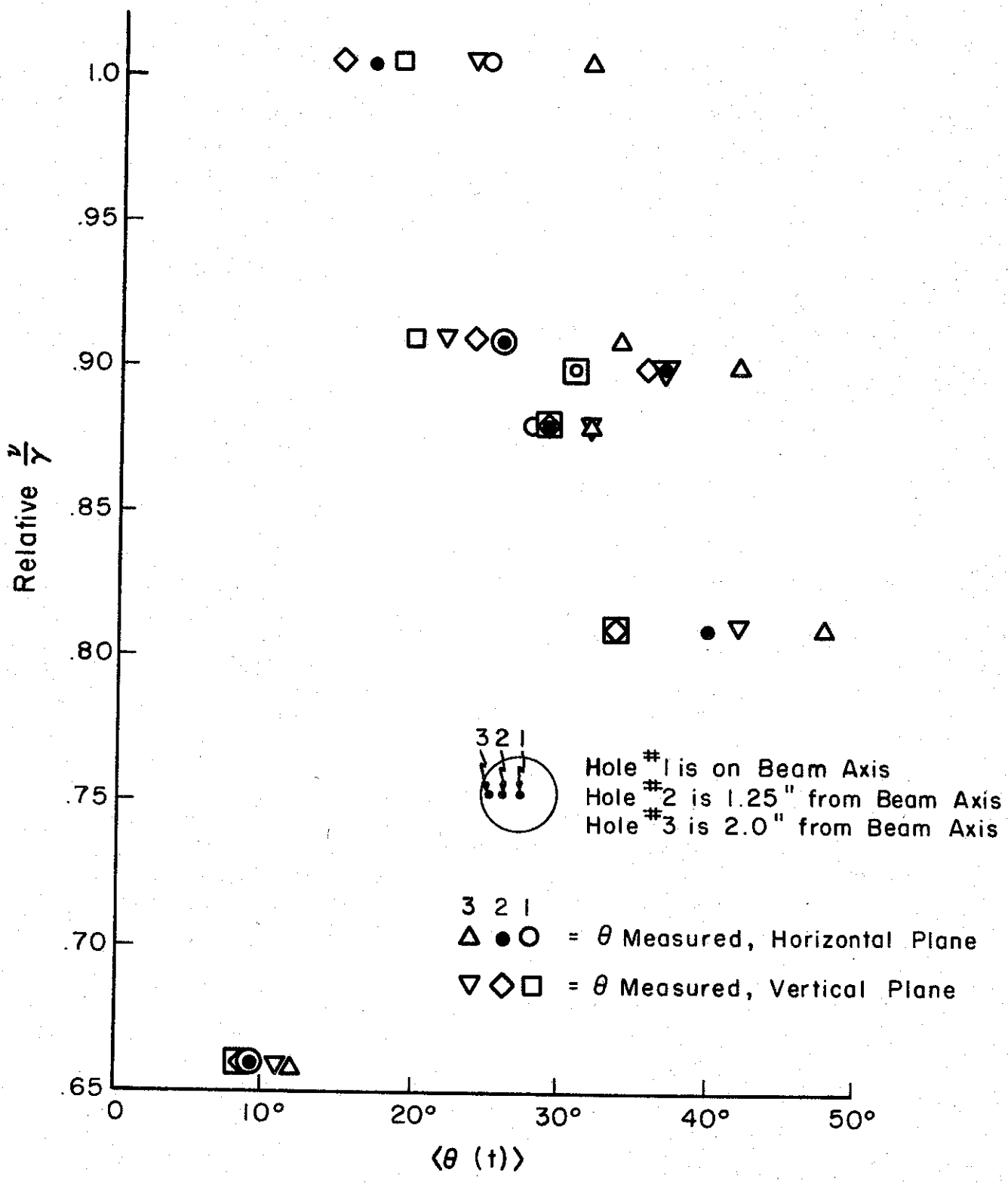

Fig. 54. Plot of Average Electron Trajectory Angle at Anode Plane versus Diode Relative $\frac{\nu}{\gamma}$

The streak-camera photographs indicate that the instantaneous trajectory angle at the anode may vary as much as 1.7/1 in times as short as 12 nsec .

D. DIODE IMPEDANCE - REVISITED

A diode pinch model essentially similar to Freidlander's and operationally useful for predicting diode impedance has been proposed by de Packh.[26] In de Packh's notation Childs' Law is expressed as:

$$\frac{i_{MA}}{V_{MV}} = .0074 \; V_{MV}^{1/2} \; \left(\frac{r_o}{d}\right)^2 = \frac{1}{Z_{C-L}} \qquad (97)$$

and the critical diode current which will cause the Larmor radius of the outermost beam electron to be just equal to the diode gap is:

$$\frac{i_{MA}}{V_{MV}} = .017 \; \left(1 + \frac{1}{V_{MV}}\right)^{1/2} \; \frac{r_o}{d} = \frac{1}{Z_{PINCH}} \qquad (98)$$

where

i_{MA} = diode current (megamps)

V_{MV} = diode voltage (megavolts)

r_o = cathode radius

d = anode-cathode gap

If these two equations are set equal, the critical value of r_o/d (i.e. F) may be found as follows:

$$\frac{Z_{C-L}}{Z_{PINCH}} = \frac{2.16}{F} \; \frac{\sqrt{V+1}}{V} \qquad (99)$$

or

$$F_{CRITICAL} = 2.16 \; \frac{\sqrt{V+1}}{V} \qquad (100)$$

Using (100) we have:

$V_{(MV)}$	$F_{CRITICAL}$	V_{MV}	$F_{CRITICAL}$
.250	9.65	.375	6.72
.275	8.90	.400	6.41
.300	8.21	.425	6.05
.375	7.65	.450	5.77
.350	7.15	.475	5.52
		.500	5.27

For a shot wherein $F_{GEOMETRY\ OF\ DIODE} > F_{CRITICAL}$ we may expect from equation (99)

$$Z_{PINCH} = Z_{C-L}\ \frac{F}{2.16}\ \frac{V}{\sqrt{V+1}} \approx Z_{C-L}\ \frac{F_{GEOMETRY}}{F_{CRITICAL}} \qquad (101)$$

We are therefore expecting two distinct regimes of impedance in the diode. For $F_{GEOMETRY} < F_{CRITICAL}$ the flow should be laminar and the diode impedance should follow Childs' Law (modified by ion neutralization). For $F_{GEOMETRY} > F_{CRITICAL}$ it is proposed that the crowding of the edge charge into the beam reduces the field near the cathode and correspondingly the current will be less and the measured impedances will be greater than those of Child's Law.

Recalling that (Chapter II)

$$(Z_D\ \ V_D)_{C-L} = 55.4\ d^2 \qquad (102)$$

$$(Z_D\ \ V_D)_{EMPIRICAL\ CURVE} = 30\ d^2 \qquad (103)$$

we now reconsider the data of Figure 22 (i.e. shots 54, 55, 56, 58) which did not fall on the empirical curve but rather fell on the Child-Langmuir curve. The data are:

Shot No.	V_D	Z_D	$Z_D\sqrt{V_D}$ measured	d	$\frac{r_o}{d}$ geometry	$\frac{r_o}{d}$ critical	Ratio $\frac{\frac{r_o}{d}\text{ geometry}}{\frac{r_o}{d}\text{ critical}}$
54	345	7.2	42.3	.864	5.78	7.20	.803
55	357	6.0	35.8	.864	5.78	7.05	.820
56	360	6.58	39.5	.864	5.78	6.95	.832
58	358	6.96	41.7	.864	5.78	6.95	.832

The data are now explained by the high listed ratios (i.e. the flow is approaching the pinch condition). Note that the lowest listed ratio is .803 which is very close to the .82 ratio mentioned earlier as the onset ratio of $\nu/\gamma/_{\text{measured}} \Big/ \nu/\gamma/_{\text{critical}}$ for pinching in our more recent streak photos. Data taken on 7/17/68

Shot No.	V_D	Z_D	$(Z_D\sqrt{V_D})$ measured	d	$\frac{r_o}{d}$ geometry	$\frac{r_o}{d}$ ctitical	Ratio $\frac{\frac{r_o}{d}\text{ geometry}}{\frac{r_o}{d}\text{ critical}}$
2	500	6.6	46.7	.875	5.7	5.27	1.08
6	480	6.35	44.0	.875	5.7	5.52	1.03
10	520	6.57	47.3	.875	5.7	5.20	1.09

for ratios > 1.0 indicate that the pinch region has definitely been entered since the measured values of $Z_D\sqrt{V_D}$ are greater than or equal to those predicted by Child-Langmuir, and that the correction of equation (101) is valid, i.e.

Shot No.	$(Z_D\sqrt{V_D})_{C\text{-}L}$	$(Z_D\sqrt{V_D})_{\text{measured}}$	$(Z_D\sqrt{V_D})_{\text{PINCH}}$ (calculated from (equation (101))
2	42.3	46.7	46.9
6	42.3	44.0	43.8
10	42.3	47.3	46.4

We contrast the data above with those of 10/29/68 i.e.

Shot No.	V_D (KV)	Z_D	$(Z_D\sqrt{V_D})_{C-L}$	$(Z_D\sqrt{V_D})_{measured}$	$(Z_D\sqrt{V_D})_{EMPIRICAL\ CURVE}$	d	$\frac{r_o}{d}_{geometry}$	$\frac{r_o}{d}_{critical}$	Ratio $\frac{\frac{r_o}{d}_{geometry}}{\frac{r_o}{d}_{critical}}$
2	409	6.67	72.5	42.4	39.3	1.145	4.39	6.15	.714
3	409	7.29		46.4				6.30	.697
4	373	7.09		43.2				6.72	.654
5	346	7.96		46.7				7.15	.614
6	366	6.62		40.0				7.00	.627
7	393	6.26		39.2				6.43	.682
8	330	8.27		47.4				7.60	.577

and note that over a ratio range of .577 - .714 the flow is still laminar i.e.$(Z_D\sqrt{V_D})_{measured} < (Z_D\sqrt{V_D})_{C-L}$ and the empirical curve of Figure 22 is accurate. Since the highest ratio observed for laminar flow is .714 and the pinched mode has been observed consistently for ratios of approximately .820 a severe transition zone between the two flow regimes is expected. In any case, the diode impedance is predictable within a factor of two over a broad range of anode-cathode gaps and diode pressures.

CHAPTER V - SUMMARY AND CONCLUSIONS

The accelerator described in Chapters I and II has proven to be a very reliable research tool. To date approximately 2000 shots have been made at average currents of 60 KA , average voltages of 325 KV and with peak currents of 125 KA and peak voltages of 600 KV . These shots have yielded data on:

a) the propagation characteristics of the beam in various drift tube configurations[32]

b) the effects of an external axial magnetic field on beam propagation characteristics[24]

c) the effects of drift tube pressure and gas type on beam parameters[33]

d) microwave radiation from the beam[34]

e) the fluence distribution of the beam as a function of drift tube pressure and axial position (z).[23]

The plasma cathode used to generate the beam for these experiments is of interest for its own sake because it:

a) can provide uniform emission and laminar flow (Chapter III) over a large area. Since

$$Z_D \propto \frac{d^2}{V_D^{1/2}\,\pi r_C^2} \propto \frac{1}{V_D^{1/2}} \cdot \frac{1}{F^2} \qquad (102)$$

for a given input voltage and (low) impedance a large area cathode allows larger gaps and therefore relaxes the dimensional tolerances. These larger gaps can become quite important for very high current (megamp) machines in which more anode ions will be released, and at longer (80-100 nsec) pulse lengths because diode impedance

collapse may then be limited by ion transit times in the gap.

b) provides good shot-to-shot reproductibility (if pinching does not destroy the anode or evaporate anode material onto the cathode surface)

c) is long lived (i.e. is easily faced off if it receives surface damage).

The dielectric fill of the plasma cathode has been shown to make an important contribution to the uniformity of cathode emission by means of a surface multipactor or flashover effect which supposes that enough of the dielectric is vaporized to cause a plasma sheath to form in front of the cathode. Electrons released from this sheath under space-charge-limited conditions then determine the overall diode impedance, Z_D (Chapter III).

Diode impedance has empirically been shown to be equal to or just greater than that predicted by Child's Law for the pinched mode of the diode and less than Z_{CHILD} by a factor of approximately two for the usual case of laminar flow (Chapter II).

The impedance predictions assume that little or no voltage exists across the anode-cathode gap prior to the arrival of the main pulse (V_D). Should such a "pre-pulse" voltage exist the diode impedance will be greatly different from that of the non "pre-pulse" case (Chapter II, Section D.3) as evidenced by NRL results.[11] Some success has been had in eliminating "pre-pulse" voltages by special cathode shank designs.[31]

The models of Friedlander et al[14] and de Packh[25] have proved very useful for estimating diode pinch conditions (Chapter IV). Such conditions are of extreme interest because they pre-determine the

propagation characteristics and fluence distribution of the beam in the drift tube.[23,31]

Diode pinching has been observed to occur (radiographs, distributed calorimeter measurements) for values of $\nu/\gamma/_{measured}$ above 82% of $\nu/\gamma/_{critical}$ as defined by Friedlander, and a minor correction to his model for $v_{initial} = 0$ has been offered.

Fast-streak and framing-camera studies indicate 1) the diode pinch build-up time is generally about 30 nsec and that 2) the severity of pinching is pressure dependent (Figures 50c-e) whereas the overall diode impedance, Z_D, is pressure independent - at least over the available range of 5×10^{-3} to 10^{-5} torr.

The masking techniques used in the streak-camera studies are directly applicable for use in the drift tube, and similar measurements should be carried out in the drift tube as a function of axial position , z.

When undesirable,diode pinching may be decreased (or eliminated) by employing:

a) the extension of the anode-cathode gap into an axial magnetic field of the same order as, or greater than, the self-magnetic field of the beam (Chapter IV, Section A.3)

b) cathode designs such as the narrow ridge cathode may be used to generate a hollow beam, and for which preliminary measurements support Hammer's[23] predictions of increased beam stability for a given ν/γ ratio (Appendix B).

c) a combination of (Chapter IV, Section B.3)

1. the lowest possible operating pressure

2. use of gases other than air which are more difficult to ionize

3. cathode and anode of the highest melting point materials consistent with electron-foil penetration depth etc.

d) convex cathode and concave anodes. Friedlander et al[14] have considered this geometry analytically and it looks quite promising since the $\overline{E}$ field lines in the gap are divergent, (would therefore cause the initial electron trajectories to be divergent) and would better counter-balance their self magnetic field. (There has,however, been some difficulty with the convergence of their computer program.)

APPENDIX A

HIGH CURRENT RELATIVISTIC ELECTRON BEAM CHARACTERISTICS - A SUMMARY

The theoretical development of relativistic electron beams began in 1934 when W.H. Bennett[27] showed that electrostatically neutralized high current electron streams could be magnetically self-focusing. The "Bennett Pinch Relation"

$$I^2 = \frac{8\pi}{\mu_o} Nk (T_e + T_i) \tag{103}$$

where N is the number of electrons and singly charged ions/meter

k is the Boltzmann constant

μ_o is free space permeability ($4\pi \times 10^{-7}$)

T_e, T_i are electron and ion temperature in degrees Kelvin

specified a critical current above which the stream would be pinched by its own magnetic field. The validity condition of this relation being $v_t \ll v_z$ where v_t, v_z are the beam transverse and axial velocity components respectively.

In 1939 Alfven[28] defined a current limit $I_A \simeq 17000\ \beta\gamma$ where $\beta = v_z/c$ and $\gamma = (1-\beta^2)^{-1/2}$ due to the pinch forces of the beam's self-magnetic field, and showed that for currents less than, equal to, or greater than I_A, the particle orbit would be (respectively) sinusoidal about, perpendicular to or even backward to its original propagation axis.

In 1957 and 1958 J.D. Lawson[29,30] extended the concept of perveance to include relativistic and space-charge effects, by defining a generalized perveance K which can be reduced to Bennett's critical current relation for $f = 1$.

Lawson's model assumed $v_t = 0$ and no collisions in the beam. In a cylindrically symmetric beam with constant radius ($r = a$), the radial electric field is $E_r = 2N_e\, er\,(1-f)/a^2$ statvolt/cm where N is the number of electrons/cm and f is the ratio of singly charged ions to electrons. If the electrons are traveling with a velocity $\beta_z c$ parallel to the axis and the ions are at rest, $B_\theta = 2N_e\, er\,\beta_z/a^2$. The radial force on a electron in the beam at a distance r from the axis is

$$F_r = \gamma_m \frac{d^2r}{dt^2} = 2N_e\,(1-\beta_z^2 - f)\,\frac{e^2 r}{a^2} \qquad (104)$$

at the beam edge, $r = a$

$$F_r = \frac{2N_e e^2}{a}\,(1 - \beta_z^2 - f) = \gamma_m \beta_z^2 c^2 \frac{d^2r}{dz^2} \qquad (105)$$

or

$$\frac{r d^2r}{dz^2} = \frac{2\nu}{\beta_z^2\gamma}\,(1 - \beta_z^2 - f) \qquad (106)$$

where $\nu = N_e e^2/4\pi\,\epsilon_o\, mc^2 = Nr_o$ is the number of electrons per classical electron radius ($r_o = 2.82 \times 10^{-15}$ meters) and I may be written as $N_e \beta c = 17000 \nu \beta$. K, the generalized perveance is defined as

$$K = \frac{2\nu}{\gamma}\,\frac{(1 - \beta_z^2 - f)}{\beta_z^2} \qquad (107)$$

and reduces to $15{,}000\ I/V^{3/2} = 15000\ k'$ for a non-relativistic, non neutralized beam, where k' is the usual perveance, in units of amps per $(\text{volt})^{3/2}$.

The solutions to $r\,(d^2 r/d_z^2) = K$ are shown in Figure 55.

For positive perveance, the beam diverges, while for negative perveance an initially parallel beam of radius $r = r_o$ converges in a distance less than $z = r_o\,(\frac{2}{K})^{1/2}$. Lawson indicates that only beams

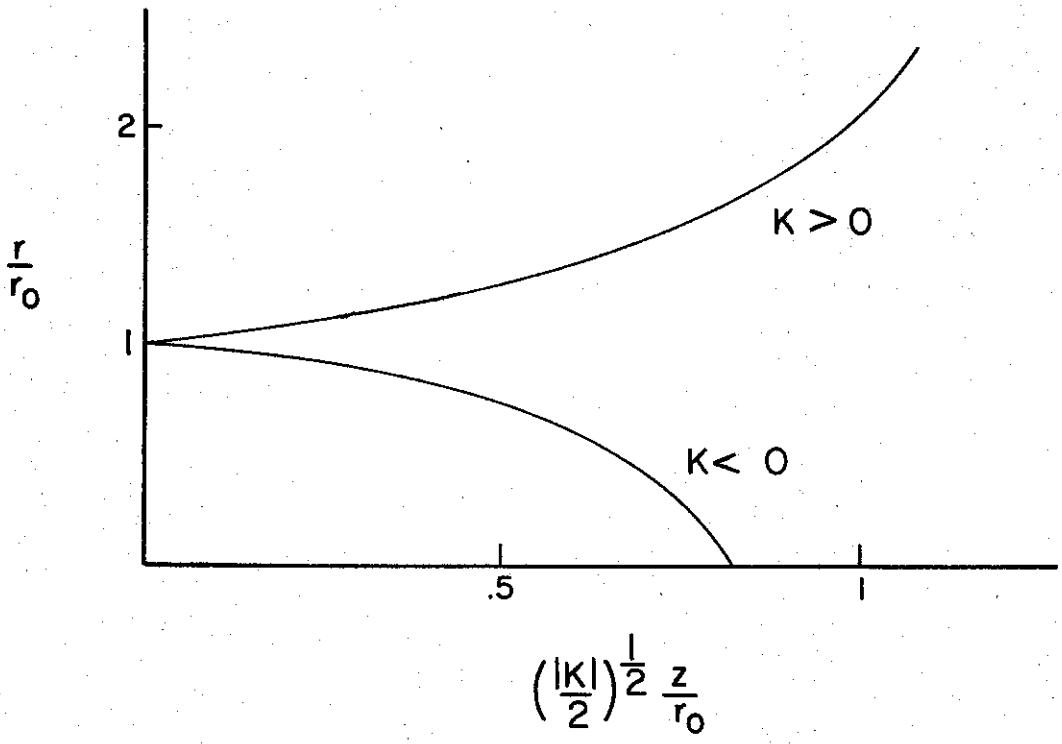

Fig. 55. Solutions to $r\frac{d^2r}{dt^2} = K$. (After Reference 30)

for which $K \ll 1$ can exist for more than a very short distance.

Lawson next considered a more general model allowing small initial transverse velocities. He found

$$\gamma m\left[\frac{d^2r}{dt^2} - r\left(\frac{d\theta}{dt}\right)^2\right] = \frac{2N_e e^2 r}{a^2}(1 - \beta_z^2 - f) \qquad (108)$$

Neglecting angular motion and considering the projection of the trajectory on a plane through the axis he sets $x = r \cos\theta$. This gives:

$$\frac{md^2x}{dt^2} - \frac{2N_e e^2}{\gamma a^2} x\,(1 - \beta_z^2 - f) = 0 \qquad (109)$$

or

$$\frac{1}{c^2}\frac{d^2x}{dt^2} - \beta_z^2 \frac{Kx}{a^2} = 0 \qquad (110)$$

and using

$$\frac{d^2x}{dt^2} = \beta_z^2 c^2 \frac{d^2x}{dz^2} \qquad (111)$$

he found

$$\frac{d^2x}{dz^2} - \frac{Kx}{a^2} = 0 \qquad (112)$$

or, the equation for simple harmonic motion.

For $K < 0$, the solution is a sinusoidal trajectory of wavelength $= 2\pi a/(-K)^{1/2}$. The requirement of small transverse velocities implies the condition that $\lambda \ll 2\pi a$ which implies $-K \ll 1$. This agrees with the previous conclusion drawn from Figure 55.

Further physical insight into the condition $K \ll 1$ (which for $f = 1$, becomes $\nu/\gamma \ll 1$) may be had by considering the Larmor radius of a beam electron expressed in terms of the beam radius, a.

$$a_{LARMOR} = \frac{v_z}{\omega_c} = \frac{\gamma mcv_z}{eB_\theta} = \frac{\gamma mcv_z}{e}\ \frac{ca}{2I} \qquad (113)$$

$$= \frac{\nu}{\gamma}\ \frac{a}{2} \qquad (114)$$

where ω_c is the electron cyclotron frequency. For $\nu = \gamma, a_e = a/2$ or electrons at the beam edge will turn around causing the beam to break up. In addition, for $\nu/\gamma = 1$ the Debye length is of the same order as the beam radius and plasma oscillations are possible. Stable beams would include only those for $I_A \leq 17{,}000\ \beta\gamma$ or for Lawson ($\nu = \gamma$) $I_L \leq 17{,}000\ \beta\nu$.

Recent experiments at Ion Physics Corporation[22] and Physics International Company[31] have shown that for drift-tube pressures $\leq .01$ torr beams of current greater than about $I_A/2$ were unable to propagate. For pressures $\geq .1$ torr Physics International Corporation and Cornell University experiments have shown currents considerably greater than I_A can be propagated. Hammer[23] was led to consider and answer affirmatively the question: "Can theoretical self-consistent beam models be constructed which allow the propagation of relativistic electron fluxes in excess of $17{,}000\ \beta\gamma$ amperes?" Hammer has proposed three models to explain the observed current fluxes.

"The first theoretical model discussed is a self-consistent, fully relativistic electron beam equilibrium consisting of mono-energetic electrons having the same canonical axial momentum, partially or fully neutralized by infinitely massive possible ions. It is found that by concerntrating its current density in a sheath of thickness c/ω_{pb} , the ratio of the velocity of light to the beam plasma frequency, this equilibrium is able to carry arbitrarily large total beam current.

In the second theoretical model, the initial-value problem of an electron beam propagating in a plasma of density large compared to the beam density is solved in the time asymptotic limit. The beam velocity is assumed large compared to the plasma thermal velocity, and at the initial time the beam is not electrostatically neutralized, nor is there any backstreaming plasma current tending to cancel the beam's self-magnetic field. The solution indicates that the plasma neutralizes the beam charge density, and a counter-streaming current carried by slowly moving plasma electrons is induced which tends to cancel the beam magnetic field. In the limit of the beam radius being large compared to c/ω_p, where c is the velocity of light and ω_p is the background plasma frequency, the magnetic neutralization is nearly complete and a nearly field-free environment is obtained through which a beam with arbitrary current can propagate.

The final theoretical model treated is a uniform beam propagating in the presence of a uniform axial magnetic field. In the limit in which the axial field is large compared to the maximum self-magnetic field of the beam, it is found that superimposed on the uniform axial motion are two rotations - a high frequency gyration with small radius about a guiding center which slowly rotates around the beam axis. This result holds regardless of the degree of neutralization or total current in the beam."[23]

APPENDIX B

FAST STREAK CAMERA STUDY OF A HOLLOW ELECTRON BEAM

As mentioned in Appendix A, Hammer[23] has predicted that a fully relativistic self-consistent equilibrium is possible for an electron beam "which concentrates it's current density near the edge of the beam so that beam electrons have left high field regions before they have a chance to turn around on themselves." He further indicates that an experiment to launch a high-current-density shell beam into a background plasma of density approximately equal to the beam density would serve as a useful check on his proposed equilibrium model.

Although no such beam has been launched into a pre-ionized background gas at Cornell, preliminary measurements on the narrow ridge cathode of Figure 31 indicate that such a "hollow" beam is in fact more stable in the diode gap than solid beams for a given ratio of $\nu/\gamma/_{\text{measured}}$ to $\nu/\gamma/_{\text{critical}}$.

The radiograph and streak camera photograph of such a beam are shown in Figure 56. The radiograph indicates that the emission is somewhat enhanced on the downstream (right) side but no pinching of the beam is evident in either the radiograph or streak photograph. The data for this shot and those of a skewed and pinched solid beam are compared:

Shot/date	Beam type	Emission Pattern	V_D	I_D	Z_D	Gap	$\nu/\gamma/_{\text{measured}}$		$\nu/\gamma/_{\text{critical}}$
8 of 5/8/69	Solid	Skewed and Pinched	372	72Ka	5.2Ω	.290"	$\frac{2.93}{3.45}$	=	.840
18 of 5/8/69	Hollow	Slightly Skewed	314	80.5	3.9Ω	.226"	$\frac{3.75}{4.43}$	=	.845

(The emission points in the central section of the hollow beam can be removed by machining away the metal in this section, thus opening the gap there.)

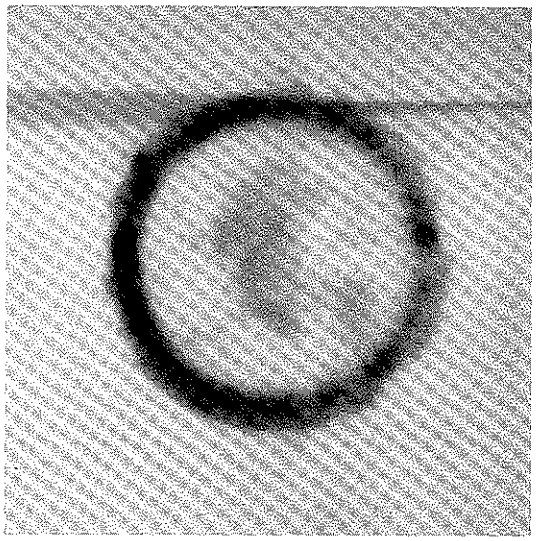

(a)
Magnification ≈ 1/2

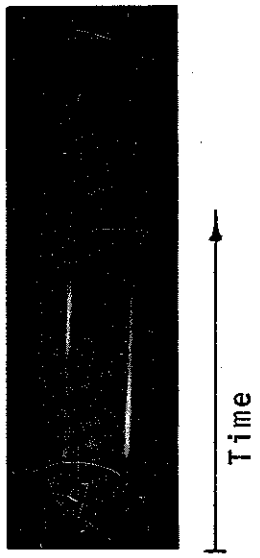

(b)
Streak Rate = $\frac{50 \text{ nsec}}{50\text{mm}}$

Fig. 56. Radiograph and Streak Camera Photograph of Emission From Narrow Ridge (Hollow Beam) Cathode.
Shot #18, 5/8/69
V_D= 314 KV, I_D= 80.5 KA, Z_D= 3.9Ω

$$\left|\frac{\nu}{\gamma}\right|_{\text{Measured}} \Big/ \left|\frac{\nu}{\gamma}\right|_{\text{Critical}} = \frac{3.75}{4.43} = 0.845$$

REFERENCES

1. Martin,J.C., Champney, P., Storr, T. et al., "Lecture Notes Prepared for a Visit of Sandia Corporation" AWRE, Aldermaston, England, Publication, March, 1964.

2. Martin,J.C., AWRE Aldermaston,England, Private Communication.

3. Ury,M., Clark,J., "Analysis of Energy Transfer Between Marx Generator and Blumlein Transmission Line" Internal Report No. 2, Laboratory of Plasma Studies, Pulse Power Division, Cornell University, January, 1969.

4. Clark,J., Ury,M., Andrews,M., Hammer,D., Linke,S., "High Current Relativistic Electron Beam Accelerators at Cornell," Report of 10th Symposium on Electron, Ion, and Laser Beam Technology May 21-23, 1969, National Bureau of Standards, Gaithersburg, Md., San Francisco Press, San Francisco, Calif.

5. Smith,I.D., "Pulse Breakdown of Insulator Surfaces in a Poor Vacuum," Proc. of the International Symposium on Insulation of High Voltages in Vacuum, Oct. 1964.

6. Watson, A., Shannon,J., "Pulsed Flashover in Vacuum," Ion Physics Corp. Burlington, Mass. - Private Communication.

7. Hemenway, C.L., Henry,R.W., Caulton,M., "Physical Electronics," pp. 106-8, John Wiley and Son, 1962.

8. Harmon,W.W., "Fundamentals of Electronic Motion" McGraw-Hill,1953,

9. Bennett,W.H., "Magnetically Self-Focusing Streams," Phys. Rev., vol. 45, pp. 890-897, June 15, 1934.

10. Spangenberg,K.R., "Vacuum Tubes," pp. 757, McGraw-Hill, 1948 .

11. Vitkovitsky,I., Plasma Physics Division, Naval Research Laboratory, Washington, D.C., Private Communication.

12. Acton,E.W.V., "The Space Charge Limited Flow of Charged Particles in Planar, Cylindrical, and Shperical Diodes at Relativistic Velocities," J.Elect. and Control, 3, pp. 203-210 (1957).

13. Boers,J.E., Kelleher,D., "Exact Solution of Poisson's Equation for One-Dimensional Space-Charge-Limited Relativistic Flow" ~~Research Report No. SC-RR-68-536, Sandia Laboratories, Albuquerque, New Mexico~~ Radiation Production Note 16 (Nov. 1968).

14. Friedlander,F., Hechtel, R., Jory, H., Mosher,C., "Megavolt-Megaampere Electron Gun Study" Final Report, Defense Atomic Support Agency (DASA) No. 2173, Sept. 1968, Washington, D.C. 20305.

15. Kraemer,J., Crewson,W., "Cogen Final Report," EG and G, Brookline, Mass., April 1968.

16. Fowler, R.H., Nordheim,L., "Electron Emission in Intense Electric Fields," Proc. Roy. Soc. London, Series A 119 173 (1928).

17. Susskind,C., (Editor), "The Encyclopedia of Electronics" Reinhold Publishing Corp., New York, (1962).

18. Dyke,W.P., and Dolan,W.W., "Field Emission" in "Advances in Electronics and Electron Physics" Academic Press,N.Y. Vol. 8(1956).

19. Gray,T.S., "Applied Electronics" John Wiley and Son, MIT Press (1954).

20. Little, R.P. and Smith,S.T., "Electrical Breakdown in Vacuum," IEEE Transactions on Electron Devices, Vol. ED-12, pp. 77-83 (1965).

21. Bennette, C.J., Swanson,L.W., Charbonnier,F.M., "Electrical Breakdown Between Metal Electrodes in High Vacuum,II. Experimental," J.Appl.Phys., vol. 38, pp. 634-640 (1967).

22. Uglum,J., McNeill,W., Rizzo, J., Graybill,S., "Research on Beam Stopping due to Self-Magnetic Compression," Defense Atomic Support Agency Report No. DASA 2167, Ion Physics Corporation, Burlington, Massachusetts, Nov. 1968.

23. Hammer,D., "Studies of High-Current Relativistic Electron Beam Propagation" Ph.D. Thesis, Cornell Univ., Ithaca, N.Y. 1969.

24. Bzura, J., Laboratory of Plasma Studies, Cornell University, Private Communication (1969).

25. Rose,D., Clark,M., "Plasmas and Controlled Fusion" pp. 334 MIT Press (1961).

26. dePackh,D.C., "The Vacuum Pinch in Parallel-Plane Diodes: A Preliminary Examination," Internal Report, Naval Research Lab., Washington, D.C. 12 March 1968.

27. Bennett,W.H., "Magnetically Self-Focusing Streams," Phys. Rev., 45, p. 840 (1934).

28. Alfvén,J., "On the Motion of Cosmic Rays in Interstellar Space," Phys. Rev., 55, p. 425 (1939).

29. Lawson,J.D., "On the Adiabatic Self-Constriction of an Accelerated Electron Beam Neutralized by Positive Ions" J.Elec. and Control, 3, 587, (1957).

30. Lawson,J.D., "Perveance and the Bennett Pinch Relation in Partially Neutralized Electron Beams," J.Elec. and Control, 5, p. 146, 1958.

31. Yonas,G., and Spence,P., "Experimental Investigation of High ν/γ Electron Beam Transport" Physics International Company, San Leandro, Calif., Report No. PIFR-106 (Oct. 1968). RPN 41

32. Hammer,D., Laboratory of Plasma Studies, Cornell University, Private Communication (1968).

33. Andrews, M.L.,Bzura,J.J., Davitian, H.E., Fleischmann,H.H., Hammer,D.A., "Experimental Measurements on High Current Relativistic Electron Beams," Bull.A.P.S. Paper 7E7, 13, p.1572 (1968).

34. Nation,J.A., "Microwave Radiation from Relativistic Electron Beams," Bull.A.P.S. Paper 7E8, 13, p. 1572 (1968).